Controllable Free-Volume in Polymer-Grafted Nanoparticle Membranes: Origins, Characterization, and Applications

Eileen N. Buenning

Submitted in partial fulfillment of the
requirements for the degree of
Doctor of Philosophy
in the Graduate School of Arts and Sciences

COLUMBIA UNIVERSITY

2018

ABSTRACT

Controllable Free-Volume in Polymer-Grafted Nanoparticle Membranes: Origins, Characterization and Applications

Eileen Buenning

Polymer based membranes play a key role in several industrially important gas separation technologies, e.g., removing CO2 from natural gas, with enormous economic and environmental impact. In this thesis, we develop a novel hybrid membrane construct comprised entirely of inorganic nanoparticles grafted with polymer chains. For all graft architectures studied, the permeability of several small gases and condensable solvents are higher in GNP membranes than the neat polymer analogs. More interestingly, the matrix-free GNPs displayed a non-monotonic peak in gas permeability as a function of grafted chain molecular weight, M_n, at a fixed grafting density, σ. Furthermore, in contrast to neat polymer membranes, which suffer from degraded performance over time due to chain densification and "aging", the performance of GNP membranes is preserved for months to years. We show that these enhancements are not limited to a single polymer, thus we suggest that this grafting mechanism may be an option to improve permeability in polymer membranes in general.

We conjecture the grafted polymer chains must stretch to fill the interstitial voids in the NP "lattice", as such voids would be free-energetically unfavorable due to the relatively high surface tension of the polymer melt. Since this stretching leads to an unfavorable chain conformational entropy, we expect a decrease in the polymer density, which we verify experimentally as well as through molecular dynamics simulations. When a penetrant molecule is placed in these regions of

highest distortion, the chains can assume more favored, undistorted conformations. This in turn creates a driving force for further penetrant uptake. Therefore, we systematically study the structure and dynamics of matrix-free GNP materials at various chain grafting densities and a wide range of graft molecular weight. Small angle scattering experiments reveal that the core nanoparticle spacing systematically increases with increasing molecular weight but the overall morphology remains amorphous and isotropic. Whereas previous studies[1] have found the brush height in matrix-free GNPs scales as the degree of polymerization $\sim N^{0.5}$, we find that the brush height in our systems scales $\sim N^{0.7}$, indicating the chains are indeed highly stretched. Moreover, studies of the structural evolution upon swelling with solvent show that the brush is fully wetted and the solvent distribution is homogeneous within the film.

Additionally, we systematically probe the dynamics of matrix-free GNP systems over broad length and time scales using linear and non-linear mechanical rheology, and broadband dielectric spectroscopy. The linear viscoelastic response shows that while the polymeric signal (e.g. glassy and Rouse dynamics) is equivalent for a range of graft chain lengths, the terminal flow of these materials is slowed by several decades compared to the neat melts of corresponding molecular weight. The low frequency (long time) response shows that below a critical molecular weight, these systems transition from polymeric to that of a colloidal system. To understand this behavior, a scaling theory is developed to describe the polymer brush conformation, which reveals that at this transition point the grafted particles behave as a system of packed “rigid” spheres. We note that the transition point coincides with the maximum observed in the transport behavior, and that the reduced system mobility may be responsible for the reduced aging effects. On the other hand, secondary relaxations for GNPs at this transition molecular weight are found to be faster than the neat polymer of corresponding molecular weight, which is attributed to a lower effective

polymer density found in these samples. Therefore, the critical question underpinning this work is: how do the structure and dynamics influence and/or result from increased free volume in matrix-free grafted nanoparticle materials? We conclude that matrix-free grafted nanoparticle constructs allow for precise control of structure-property relationships over multiple length scales, and serve as a novel materials design platform with the potential to function as high performance gas separation technologies.

Contents

List of Figures **v**

List of Tables **viii**

1. Introduction **1**

1.1 Gas Separation via Polymeric Membranes 2

1.2 Structure and Morphology of Polymer Grafted Nanoparticle Systems 7

1.3 Dynamics of Matrix-Free Grafted Nanoparticles 11

2. Polymer-Grafted Nanoparticle Membranes with Controllable Free-Volume **15**

2.1 Materials and Methods 16

2.1.1 Material Synthesis and Sample Preparation 16

2.1.2 Steady-State Permeation 19

2.1.3 Non-Steady State Diffusion with Quartz Crystal Microbalance 20

2.2 Transport in Matrix-Free Polymer Grafted Nanoparticles 21

2.2.1 Diffusion of Light Gases 22

2.2.2 Permeability Enhancement Driven by Free Volume 25

2.2.3 Condensable Penetrant Experiments 30

2.2.4 Aging Effects 32

2.2.5 Computer Simulations 33

3. Determining the Structure of Polymer-Grafted Nanoparticle Membranes **38**

3.1 Materials and Methods 39

3.1.1 Bulk Sample Preparation 41

3.1.2 Thin Film Preparation 42

3.2 Transmission Electron Microscopy 43

3.3 Bulk SAXS and PDF Analysis 44

3.4 Structure of Polymer-Grafted Nanoparticle Membranes with Imbibed Solvent 50

4. Solid to Liquid Transition of Matrix-Free Polymer Grafted Nanoparticles 59

4.1 Materials and Methods 61

4.1.1 Small-Amplitude Oscillatory Shear 63

4.1.2 Creep 64

4.1.3 Non-Linear Start-Up Shear 65

4.2 Linear Dynamic Mechanical Response 65

4.2.1 Scaling of Brush Conformation in Matrix-Free Grafted Nanoparticles 70

4.3 Non-linear Response 78

5. Segmental and Secondary Relaxations Of Matrix-Free Grafted Nanoparticles 83

5.1 Materials and Methods 84

5.2 Segmental (α) Relaxation Dynamics of PMA Nanocomposites 85

5.2.1 Inter-Layer Model for α-Relaxation in Composite Systems 87

5.3 Secondary ($\boldsymbol{\beta}$ and $\boldsymbol{\beta'}$) Relaxation Dynamics from BDS 90

6. Conclusions and Future Work 95

6.1 Polymer-Grafted Nanoparticle Membranes with Controllable Free Volume 96

6.2 Determining the Structure of Polymer-Grafted Nanoparticle Membranes 97

6.3 Solid to Liquid Transition of Matrix-Free Polymer Grafted Nanoparticles 98

6.4 Segmental and Secondary Relaxations of Matrix-Free Grafted Nanoparticles .. 100

6.5 Future Work 101

6.5.1 Improvements to Grafted Nanoparticle Gas Separation Membranes 102

6.5.2 Free-Volume Distribution in the Presence of High Molecular Weight Solvents of Grafted Nanoparticle Materials 104

6.5.3 Dynamics of Matrix-Free Grafted Nanoparticles 105

References **108**

Appendix A – Experimental Methods **116**

A.1 Synthesis of Grafted Nanoparticles 116

A.2 Gas and Vapor Flow Control Apparatus 119

A.2.1 Gas Flow Control 119

A.2.2 Vapor Flow Control 120

A.3 QCM Measurement Technique 121

A.4 Free Volume Characterization 125

A.4.1 Positron Annihilation Lifetime Spectroscopy (PALS) 125

A.4.2 Surface Area Analysis via N_2 Adsoprtion (BET) 125

A.5 Differential Scanning Calorimetry (DSC) 128

A.6 Thermogravimetric Analysis (TGA) 130

A.7 Computer Simulations 130

A.7.1 MD Simulation of Ordered Nanoparticle Lattice 130

A.7.2 Single Particle Surface Analysis 131

A.8 Small Angle X-Ray Scattering (SAXS) 132

A.9 Small Angle Neutron Scattering (SANS) 132

A.9.1 Sample Flow Cell Design for SANS Swelling 132

A.9.2 Solvent Vapor Control Apparatus and Procedure for SANS 134

A.10 Non-Linear Rheology 137

Appendix B - Supplementary Info. (Ch. 2) 141

B.1 Neat Polymer Controls 141

B.2 Bare Particles in Neat Polymer 142

B.3 Effects of Graft Density 143

B.4 Permeance 147

B.5 Infinite Dilution Model 149

B.6 QCM Measurements of Light Gases 150

List of Figures

2.1: Robeson plots comparing the permeabilities of CO_2 and CH_4 22

2.2: Gas permeability properties of PMA-grafted nanoparticles 24

2.3: Single-fit positron (Ps) lifetime in PMA composites 25

2.4: Free volume metrics for PMA-grafted NP Composites 26

2.5: PMA Materials Characterization 28

2.6: Excess Volume and Fractional Free Volume Measurements 29

2.7: Transport properties for a condensable solute in PMA composites 31

2.8: Aging of neat and nanoparticle composite polymer films 33

2.9: Computer simulations of polymer-grafted nanoparticles 35

2.10: Unoccupied volumes in neat and grafted nanoparticle composite materials 36

3.1: Transmission electron microscopy of PMA composites of varying Mn 43

3.2: Transmission SAXS in bulk PMA grafted nanoparticle composites 44

3.3: Structure factor and reduced structure factor for grafted PMA nanoparticles 46

3.4: Probability distribution function $G(r)$ for grafted PMA nanoparticles. 47

3.5: Brush height of grafted nanoparticles versus degree of polymerization 48

3.6: Damped sine wave fits of $G(r)$ for grafted PMA nanoparticles 49

3.7: SAXS intensity upon solvent swelling for various solvent concentrations 51

3.8: Simulations of various particle morphologies with different solvent SLD 53

3.9: SANS intensity upon solvent swelling for various solvent concentrations 54

3.10: Solvent concentration correlation as calculated from fit contrast 57

3.11: Solubility of ethyl acetate as measured by SANS as a function of vapor activity. 58

4.1: van Gurp-Palmen plot for GNP sample 64

4.2: Master curves of PMA-g-SiO2 composites 67

4.3: Shift factors and plateau modulus enhancement of LVE spectrum in GNP systems 68

4.4: Packing fraction of rigid spheres from scaling theory as a function of Mn 72

4.5: Fits of LVE spectra for σ=0.47chains/nm^2 grafted particles 74

4.6: Relaxation times in matrix-free polymer grafted nanoparticles 75

4.7: Colloidal cage size versus brush height 76

4.8: Comparison of viscosity of matrix-free GNPs to star polymer melts..... 77

4.9: Normalized steady-state viscosity as a function of Weissenberg number 78

4.10: Failure strain rate of various GNP and neat PMA samples 79

4.11: Non-linear start up shear of PMA-g-SiO_2 composites..... 80

4.12: Mechanical reinforcement of matrix-free grafted nanoparticles 81

5.1: Segmental relaxation in BDS..... 87

5.2: Temperature dependence of α-relaxation and interfacial layer 89

5.3: Secondary relaxation time distribution as a function of time for neat PMA 91

5.4: Secondary relaxation from BDS in PMA composites 92

5.5: Relative secondary relaxation times of GNP systems 94

6.1: Effects of additional free polymer chains on small gas permeability and selectivity..... 104

6.2: Mean-squared displacement as a function of temperature..... 106

A- 1: Synthetic mechanism of SI-RAFT polymer grafted nanoparticles 117

A- 2: ^{13}C NMR of Activated DoPAT 118

A- 3: ^{1}H NMR of Activated DoPAT..... 118

A- 4: Quartz crystal microbalance analysis methods 124

A- 5: N_2 Adsorption/Desorption Isotherm and Solubility 127

A- 6: Glass Transition Temperature Tg of PMA Grafted Nanoparticles 129

A- 7: Custom sample holder for SANS swelling experiments 134

A- 8: In-situ SAXS verification and controls 136

A- 9: Raw stress versus strain response in start-up of steady shear 137

A- 10: Raw viscosity versus time for start-up of steady shear 138

A- 11: Stress relaxation upon cessation of steady-state flow as a function of time 139

A- 12: Stretched exponential fit parameters 140

B- 1: Neat PMA Transport Data 142

B- 2: Relative permeability of ungrafted silica composites 143

B- 3: Ethyl acetate vapor diffusion in Σ=0.07chains/nm^2 graft density composites 144

B- 4: Ethyl acetate vapor diffusion in Σ=0.43chains/nm^2 graft density composites 145

B- 5: Effect of Aging on low graft density grafted particle membranes. 146

B- 6: Permeance in Σ=0.43chains/nm^2 graft density composites 148

B- 7: Exponential regression of permeability from QCM 150

B- 8: Verification of QCM as a method for measuring light gas diffusion 151

B- 9: Additional light gas permeation for PMA grafted nanoparticle films 151

B- 10: Gas transport in PMMA grafted composites via QCM 151

List of Tables

2.1: PMA-based materials used for transport studies. 18

2.2: PMMA-based materials used for transport studies 19

3.1: Sample information for bulk SAXS and PDF studies 40

3.2: Sample information for TEM, and thin film swelling SAXS/SANS 41

3.3: Fitting parameters of swollen films in SAXS for various solvent concentration 55

3.4: Fitting parameters of swollen films in SANS for various solvent concentration 56

4.1: Sample specifications for rheological studies 62

4.2: Grafted brush dimensions as a function of Mn from scaling theory 71

5.1: BDS Sample Specifications 85

5.2: VFT fit parameters of α-relaxation from BDS 90

5.3: Secondary relaxation processes activation energies 93

A- 1: Fitting parameters of swollen films in SAXS controls 136

Acknowledgements

In my time as a graduate student, I have traveled to two countries and eight states for research alone, and have met so many wonderful, interesting, and brilliant people I am proud to call my peers. There is not enough white space to express my gratitude for the multitude of people who have supported me during the past five years. First and foremost, I would like to thank Professor Kumar for his guidance and wisdom, as a mentor who can always see the bigger picture. Not only is Sanat a renowned scientist, but he is someone who truly sticks by his students. As someone who isn't known for keeping mum and protecting the status quo, Sanat is someone I truly admire for his continual efforts to fight for a fairer system, in particular for women in science.

During my second year, while in the hospital recovering from vascular surgery, I suddenly found out I had been accepted to a program with the Dept. of Energy, and would be abruptly moving to Oak Ridge, TN for nearly a year. At the beginning, it felt a little like I was there against my will, but it turned out to be one of my favorite years of my PhD. At Oak Ridge, my research flourished, and I began the three major projects that would shape my thesis. I would sincerely like to thank Prof. Sokolov for not only serving on my PhD committee, but also for taking me into his group and helping me to formulate several exciting ideas. Also, I want to deeply thank Dr. Shiwang Cheng for being my mentor that year. Shiwang was really the first person I had to show me the ropes in the lab, and I consider him a dear friend and colleague. There were also so many people from the Sokolov group who became good friends of mine, including Vera, Dima, Fei, Adam and especially Bobby, who was instrumental to the success of our dielectric project.

Upon returning from my "sabbatical" in TN, I found that the Kumar group had changed *dramatically* in (perhaps due to?) my absence. This group of peers quickly became my steadfast

teammates, and they have inspired me and supported me ever since. Even in the face of my unrelenting and unbearable optimism, they never tired of me, never gave up on me. Each one of these people I have been so fortunate to get to know are brilliant in their own right, and I have confidence in every single one of them. These members include: Dong, Makoto, Dan S., Kai, Wes, Dan Z., Mayank M., Connor, Mayank J., Clement, Sophia, Alejandro, Gianna, and especially Thi, Sebastian, and Andrew. You last three are my confidants and cheerleaders and have been there for me for every struggle, and share with me just a taste of the glory.

A huge thank you must be given to Prof. Benicewicz and his group, including Yucheng Huang, who provided all the materials used for my thesis. Brian is a brilliant chemist who makes some really fun materials to play with. I must acknowledge Professor Dimitris Valssopoulos and Dr. Jacques Jestin, Daniele Parisi, and Tim Liu for being my mentors and partners on my various projects, none of this would have been possible without you. Also, I would like to thank everyone who helped with the many scattering experiments, without whom this work would not have been successful, including Dr. Paul Butler, Dr. Yiming Mao, and Dr. Lilin He, among others. To the other members of Columbia Chemical Engineering, I also owe you sincere gratitude for being my friends and struggling through this with me. To the classmates I came in with: Natalie, Weiming, Alison, and Chris, I know so many wonderful things await you, and can't wait to see what you accomplish. To the others who have come before and after me: Joe, Vi, Beyza, Harun, Lizzy, Zack, Anna, Jack, Jon, Brian, Christiana, Nick, I feel so privileged to get to know you all. Additionally, a very special thank you to the staff of the Chemical Engineering Department: Kathy Marte-Garcia, Krystal Paulino, Aurna Malakar, Rezarta Binaj, and Ariel Sanchez. There really is no way to adequately thank you for all the tireless work you do to keep this department running.

Of course, this brings me to my wonderful family. I feel your love and your pride, and I am

thankful, even if I would prefer to not draw attention to myself. On my father's side, Laura and Patrick, who housed me while I lived in Knoxville, you have both shown me what it means to know and stay true to oneself and are beautiful people. For the Doerners, I must thank my grandparents for creating such a large and caring family, and loving all of us fiercely and individually. Starting first with the cousins: Matt, Zack, Joey, Dan, Bridget, Katie, Phillip, Alex and Kayla, I have grown up with all of you, you were my first friends. My aunts and uncles (in no particular order): Maggie, Buck, Carol, Rich, Kathy, Craig, Frank, Betsy, Gina, Cale, Susie, and Bob, thank you all for pretending to understand my work, but being interested anyways. To Roya and John, thank you for welcoming me into your family as one of your own. To Dana and Christine, thank you for the bad movie and wine nights, and for always watching Calli when I had to travel so much for my research. To my sister, Hannah, I love you and the light you bring in to every room you enter. I hope you have every opportunity you want to follow your passion and desires. To my father, who has lived his life for my sister and I, and ensured every door we wanted was open to us. And to my mother, my hero, your warmth and strength has inspired me and encouraged me, and you have picked me up every time I faltered. Finally, to Sean, my love, I owe so much of this to you. I am so proud of the team that we are, and I am so grateful for your unwavering support. Thank you for sticking by me and for all the sacrifices you have made for us. I am so excited to see what life brings us. Thank you.

Dedicated to my parents,

Rosemary and Fred

Chapter 1

Introduction

Polymer nanocomposites are attractive due to their ability to combine low-cost, lightweight polymers with inorganic fillers to create materials with tunable mechanical, optical, and dielectric properties[2]. The macroscopic properties of these hybrids are heavily influenced by the multiscale organization as well as complex interactions between the filler and polymer matrix; thus, the remarkable properties of polymer nanocomposites are difficult to control and may be temporally unstable. One popular method to address these instabilities involves covalently linking the polymers to the surface of nanoparticles to create single-component grafted nanoparticles (GNP), which prevents segregation of the nanoparticle cores and significantly improves dispersion.[1,3]

One particular area of interest where performance of polymer nanocomposites, and specifically grafted polymer nanocomposites, is not well studied is that of membranes for gas separation. We find that membranes constructed of matrix-free GNPs, where no additional free polymer chains were added ("matrix free"), exhibited remarkable increases in permeability of both condensable solvents and lightweight gases relative to that of the neat polymer, with minor effects on selectivity (presented in Chapter 2).[4] More interestingly, the matrix-free GNPs displayed a non-monotonic peak in permeability as a function of grafted chain molecular weight, M_n, at a fixed grafting density, σ. Within the context of the interesting transport properties of these materials, this thesis addresses the structure (Chapter 3) and dynamics (Chapter 4 & Chapter 5) of matrix-free GNPs where the polymers are of similar size scale as the nanoparticle cores over a wide range of length (~10nm to >1μm) and time scales (from long-time, GNP diffusion through sub-second

secondary relaxations such as side chain rotation). We compare these properties to that of pure homopolymer melts in order to rationalize unique shifts in properties relevant to applications, such as gas separation membranes.

1.1 Gas Separation via Polymeric Membranes

The U.S. Energy Information Administration projects natural gas consumption will increase from 27.5 trillion cubic feet in 2016 to nearly 35 trillion cubic feet by 2050, with shale gas expected to supply more than half of this increase.[5] While natural gas provides a valuable source of raw materials as well as a clean-burning energy source, processing crude natural gas is technically challenging, costly and energy intensive.

Crude natural gas contains varying levels of impurities with the most critical being acidic gases such as carbon dioxide (CO_2) and hydrogen sulfide, and condensable natural gas liquids (NGLs).[6] Removal of acid gases is vital as they lead to extensive internal corrosion of pipelines, resulting in eventual rupture. For example, in 2000, a natural gas pipeline burst due to severe internal corrosion and the resulting blast killed 12 campers near Carlsbad, NM. [7] Similar to acid gases, NGLs also pose a threat of corrosion if the temperature of the pipeline drops below the dew point and condensate is formed. In addition to the negative impacts, pure NGLs are value-added products and so removal is also economically motivated. The current favored natural gas purification methods require conventional absorbers (acid gases) and cryogenic distillation (NGLs), which are both costly. NGL removal can be exceedingly difficult if mixtures with similar boiling points or azeotropes are present.[8]

The use of polymer membranes to selectively separate gas mixtures for various applications is well-established.[9–18] Membrane separations require a lower energy demand than

conventional technologies (e.g. distillation or adsorption) and are more cost efficient, but on the other hand, are limited by a tradeoff between gas permeability (P_i, proportional to product throughput) and selectivity ($\alpha_{ij} = \frac{P_i}{P_j}$, which dictates product purity). The inverse correlation between P_i and α_{ij} constrains the performance of these materials, and is captured by the empirical Robeson Upper Bound[9–12] which defines the current best possible membranes for a given gas separation. Other practical considerations, such as the temporal and mechanical stability of most polymer membrane materials, have also limited their large scale implementation in many key gas separations.

For many applications, glassy polymers emerge as the best among those available for membrane-based separations. In glassy, nonporous polymers the solution-diffusion mechanism controls transport—solute dissolves into the feed-side membrane surface and diffuses through. The material's permeability is then given by the expression $P_i = K_i D_i$ where K_i is the partition coefficient and D_i the diffusion coefficient.[10–12,19,20] Glassy polymers are typically diffusion selective, that is, α_{ij} is primarily controlled by the difference in D_i between the two permeating species. A useful concept here is statistical "free volume", the unoccupied volume in the condensed state subject to rapid spatio-temporal fluctuations.[19–22] This is to be distinguished from static micro/nano-porosity, i.e., static voids in the material with well-defined, temporally stable geometric characteristics. Free volume fluctuations in polymer-based materials often arise from inefficient polymer chain packing coupled to local chain dynamics. It is generally well-accepted that D_i can be manipulated by free volume variations, which is thus thought to be highest in amorphous polymer systems that possess a stiff backbone, and possibly local kinks due to geometric isomerism.[23] Such materials also inevitably exhibit high glass transitions. To date, these

architectures are almost always achieved by synthetic means,[13,24] e.g., synthesis of new polymers with bulky side groups and/or stiff, irregular backbones, that serve to frustrate local packing and hinder chain dynamics. For example, for CO_2/CH_4 separations there have been >300 unique polymers synthesized. These synthetic approaches have demonstrated the value of enhancing and controlling membrane free volume. It is relevant to note that in many cases polymers designed with high free volumes are susceptible to degradation in performance associated with aging as the non-equilibrium glassy polymers relax to a more efficient packing state.[25–28] For example, Poly(trimethyl-1-silyl pentyne) (PTMSP) one of the most permeable polymers studied in the literature, loses up to 90% of its O_2 permeability within 10 days of initial membrane fabrication.[29] Several studies have examined the effect of aging on membrane permeability. These have shown a temporal decrease in permeability directly correlated with an apparent reduction in the free volume available for molecular transport.[27] Therefore, an important practical limitation of many current membrane systems is that free volume, and thus permeability, is difficult to systematically tailor in a temporally stable fashion. The stable control of free volume to rationally design membranes thus remains an open challenge.[9,13,19]

It has been well-established that mixed matrix "composite" systems of nanoparticle filler dispersed in polymer can substantially increase the mechanical strength relative to that of a neat polymer melt [2,30] and reduce physical aging.[31,32] Both of these effects are critical parameters limiting implementation of membranes in industry. In pioneering experimental work, Freeman et al. found that the addition of bare nanoparticles to a glassy polymer can also favorably modify the free volume of the polymer.[33–35] This methodology empirically achieves large increases in both P_i and reverse selectivity relative to the pure polymer for CH_4/ nC_4H_{10} in poly(4-methyl-1-pentyne) membranes. This result is surprising as conventional composite theory (e.g., Maxwell model)

predicts that the permeability should decrease with increasing filler volume fraction ϕ, $P_\phi = P_b\left(\frac{1-\phi}{1+\frac{\phi}{2}}\right)$, where P_ϕ and P_b are the permeabilities of the composite and neat polymer, respectively, without affecting selectivity.[36] Freeman et al. hypothesized that their unexpected results arise from additional free volume caused by the incompatibility of the hydrophilic nanoparticle and hydrophobic polymer.[37] Unfortunately, this incompatibility commonly causes the nanoparticle dispersion state to be strongly affected by membrane preparation. For example, Paul et al. [38] report very different effects of nanoparticle addition on permeability, which appear to be intrinsically linked to the various nanoparticle dispersion states obtained from different processing methods. The stability of the nanoparticle dispersion can also be significantly affected by the presence of a permeating species in the composite material, which can cause the polymer phase to swell and the dispersion to rearrange. For example, Hoang et al. have shown that the total number of quantum dot aggregates in a poly(methyl methacrylate) (PMMA) film exposed to chloroform decreased significantly as the loading of chloroform in the composite increased.[39] Other work by Janes showed how the dispersion state of silica nanoparticles in poly(methyl acrylate) (PMA) is altered upon solvent annealing.[40] Thus, while improved performance is sometimes observed, this outcome is not reproducible, controllable or temporally stable.

Covalently grafting polymers to nanoparticle surfaces on the other hand has been shown to mitigate some of undesirable effects of morphological instability found in conventional nanoparticle/polymer composites. Previous work has established that polymer tethered nanoparticles cannot spuriously aggregate and can sometimes crystallize into well-defined ordered arrays, with the grafts filling the space between the cores.[3,41] Stabilizing the dispersion, may afford more control over the performance in gas separation membranes. Simultaneously, these

hierarchical nanoparticle architectures can be systematically manipulated through parameters such as grafting density and grafted chain length, which may result in precise tunability and/or control without resorting to more intensive synthetic methods.

Building on these insights, Chapter 2 systematically explores the capabilities of a novel mixed matrix construct composed purely of spherical nanoparticles isotropically grafted with long polymer chains and investigate their potential as high-performance separation membranes.[42] Steady state permeation of both light gases (e.g. CO_2, CH_4, C_4H_{10}) and condensable solvent vapor are investigated using a permeation cell. This method involves measuring the equilibrium downstream pressure of a given penetrant at a known temperature and upstream pressure. Additionally, we study the kinetic diffusion using a quartz crystal microbalance (QCM) technique. The QCM can detect nanogram mass changes in real time as a film absorbs a given penetrant species, from which the diffusivity and solubility can be extracted. To study the free volume of these grafted nanoparticle membranes, we use positron annihilation lifetime spectroscopy (PALS), which quantifies the size of a "free volume element". The overall fractional free volume can then be calculated using detailed density measurements of the composite and compare to the neat polymer melt. We address the aging of these materials by systematically testing the permeability over the course of several months to years. Finally, we use molecular dynamics simulations to predict how the structure of these materials may affect the distribution of free volume, and therefore the permeability of small penetrants.

To better comprehend the results presented in Chapter 2, we study the structure of matrix-free grafted nanoparticles in systems where the size of the polymer brush is relatively of the same size scale as the nanoparticle core. The dry-state dispersion structure as a function of graft density and molecular weight is extensively studied via transmission electron microscopy (TEM) and

small angle X-ray scattering (SAXS). Additionally, we probe the distribution of a small molecule penetrant in a swollen film of matrix-free GNPs to investigate whether the grafted brush swells homogenously or solvent is preferentially absorbed to discreet locations within the film using *in-situ* SAXS and small angle neutron scattering (SANS). Results of the morphology studies are presented in Chapter 3. Furthermore, we probe the dynamics of such matrix-free composites over a broad range of time scales. Mechanical rheology studies in both the linear and nonlinear regime are presented in Chapter 4 are used to study the relaxation processes from the polymer segment through entire grafted nanoparticle diffusion and give insight to long-time dynamics which may affect transport properties, specifically aging characteristics. In Chapter 5, broadband dielectric spectroscopy measurements are used to study segmental and secondary relaxation processes of matrix-free grafted nanoparticle materials and how differences from the pure polymer melt or physical mixtures of linear chains and bare nanoparticles can explain gas transport mechanisms of these materials. We supply in the remainder of this introduction brief overviews of each study.

1.2 Structure and Morphology of Polymer Grafted Nanoparticle Systems

The structure of polymer grafted nanoparticles, with or without free polymers, has been intensively investigated in recent years due to their benefit of enhanced control over the spatial distribution of the fillers within the composite. [1,3] Various parameters such as the molecular weight of the grafted chains, grafting density, as well as the interactions between the brush and any matrix chains, were found to have dramatic effect on the dispersion behavior.[3,42–45] The macroscopic properties of these hybrid materials are heavily influenced in turn by the multiscale organization

of the grafted particles. In Chapter 3 we investigate the structure of these materials to explore the origins of the non-monotonic trend with graft molecular weight of membrane performance (and the related apparently enhanced free volume) using a combination of microscopy and small angle scattering. This section provides a brief overview of the key aspects of scattering theory and our experimental approach.

The elastic interaction of matter with a beam of energy (light/X-rays) or particles (neutrons) can give detailed information on the arrangement of atoms and molecules as well as relatively large particles and crystal grains. For example, when a neutron from an incident beam interacts elastically with the nucleus of an atom from the sample in question, it is scattered in a different direction. The difference in the incidence, k_i, and scattered, k_f, wave vectors is defined as the scattering vector, $q = k_i - k_f$. The magnitude of q is defined as: $q = \frac{4\pi}{\lambda}\sin\theta/2$, where λ is the wavelength of the neutron beam (both incident and scattered if the collision is elastic) and θ is the angle between the incident and scattered vectors. Experimentally, we can measure the scattering intensity (number of scattered neutrons in a given solid angle) from n particles in a solution as a function of q:

$$I(q) = \sum_i^n [(\Delta\rho_i V_i)^2 P(q)]\, S(q) \tag{1.1}$$

where $\Delta\rho_i$ is the difference in scattering length density (i.e. the contrast) between the particles and solvent, V_i is the volume of a particle, $P(q)$ is the particle form factor and $S(q)$ is the structure factor. The scattering length density measures the interaction between the incoming neutron and nucleus of atoms in a molecule/particle. The term $\sum_i^n [(\Delta\rho_i V_i)^2 P(q)]$ defines the *intra-particle* interactions, summed over all the particles in the system. The form factor contains information regarding the geometry of the particles (e.g. spheres, rods, micelles, etc.). The structure factor

defines the *inter-particle* interactions and contains information on how the particles are distributed in space. In the dilute limit, $\lim_{n\to 0} S(q) = 1$. By fitting the scattering intensity function with various theoretical models, we can gain quantitative information about the particle shape, size and distribution in space. The same principles apply to the scattering of X-rays, except that ρ_i measures the interaction between an incident X-ray and the electrons of an atom instead of the nucleus.

However, because neutron scattering interacts with the nuclei of a sample, this technique benefits from the ability to manipulate $\Delta\rho_i$ through isotopic labeling, specifically the exchange of deuterium atoms for hydrogen atoms. In general, the substitution of D for H atoms does not significantly alter the properties of a material, but the interaction of a D atom with a neutron is very different than that of an H atom. The ability to change the contrast of the system offers the potential to amplify or suppress the scattering signal relative to other species within the sample to probe structures of various constituents and length scales. This is a particularly powerful tool in multi-component and/or polymeric systems where various structures can be parsed out through clever isotopic labeling schemes which would otherwise be indistinguishable using other methods such as X-ray scattering.

In one line of investigation, we measure the dry state structure using SAXS (coupled with TEM) to understand how molecular weight and grafting density affect core particle arrangement. We adapt a pair distribution function analysis (PDF) commonly used in atomic systems to analyze nanoparticle correlations embedded in the SAXS data. Taking the Fourier transform of the $S(q)$, yields the pair-correlation function, $G(r)$, which describes the probability of finding another atom (or particle center) at a given distance r from a reference atom. By analyzing the $G(r)$ in real space, we can identify more subtle effects of M_n on the structure of these materials such as the correlation length and directionality of any ordered structures that may exist. We also apply this

analytical method to a similar range of M_n for a higher grafting density to show the effect of grafting density on the structure. We demonstrate that for a range of molecular weights and two grafting densities, the core particles are isotropically well dispersed. Moreover, the inter-particle spacing increases monotonically as molecular weight increases and the brush scales as highly stretched as a function of molecular weight.

Additionally, the transport data suggest that over the range of graft molecular weight where permeability is enhanced, the polymer chains likely stretch to fill the interstitial voids between the nanoparticles cores, thus sacrificing some of their conformational entropy. We seek macroscopic manifestations of this chain stretching. Two possibilities are considered: (i) the polymer specific volume increases homogeneously and isotropically in the nanocomposite (relative to the neat polymer), or (ii) discreet, local regions between grafted particles where the chains are maximally stretched so that when a penetrant molecule is placed in these regions, the chains can assume more favored, undistorted conformations. This, in turn, creates a driving force for penetrant uptake, where solvent is preferentially segregated within the interstitial spaces. The preferential placement of the solvent (if any) could provide a means to understand the mechanism by which the GNPs yield higher membrane permeabilities for gases. Therefore, in the second part of Chapter 3, we investigate the morphology of core particles in a thin film as it swells in solvent using *in-situ* SAXS. Furthermore, we attempt to determine if the solvent preferentially accumulates in specific regions of the films by using contrast variation SANS and systematically varying the scattering length density of the solvent. We find that as films of matrix-free grafted nanoparticles swell with a small molecule solvent, the penetrate is absorbed homogeneously within in the film and therefore we conclude the enhanced free volume of these materials is distributed homogeneously within the polymer corona.

1.3 Dynamics of Matrix-Free Grafted Nanoparticles

As macromolecular constructs, polymeric systems exhibit multiple modes of relaxation on various length scales. For simple systems of linear homopolymers, on the shortest length and time scales, the secondary relaxation processes (*e.g.* β, γ) are generally attributed to localized side group rotation off a single backbone monomer. The characteristic relaxation time of this process has an Arrhenius temperature dependence with an activation energy ~2-20kT (where k is the Boltzmann constant and T is temperature in Kelvin).[46,47] On a slightly larger length scale of order ~ a few monomers, the so-called Kuhn segments cooperatively relax together. This process is typically called the segmental relaxation process (τ_0) or alpha process (τ_α). The temperature where τ_α = 100 seconds is typically comparable to the calorimetric glass transition temperature with a cooling rate of 10°C/min. The temperature dependence of this process can be empirically described by Vogel-Fulcher-Tammann (VFT) equation or Williams-Landel-Ferry equations (WLF) which is more frequently used for polymers.[48,49] When many Kuhn segments move together, the chain relaxes within a "tube" of a defined size, where motion is confined by neighboring chains.[47,50,51] When the chains are short, i.e. $M_n < 3M_e$, where M_e is the entanglement molecular weight, the melt is considered to be "unentangled". In this case, the Rouse time, τ_R, is defined as the time required for the chain to diffuse a distance on the order of its size and scales as $\tau_R \sim \tau_\alpha N^2$ where N is the number of Kuhn segments per chain.[52] When $M_n > 3M_e$, entanglement dynamics become important.[47,51] In this regime, chain relaxation can only be realized through diffusion along topologically defined tubes. As the chain ends gradually relax around the entanglement points through reptation, eventually the chain is freed from these local constraints. The characteristic

chain relaxation time is $\tau_d = 3Z\tau_R$ according to the Edwards tube model, where $Z = {M_n}/{M_e}$ is the number of entanglements per chain.[47,53]. Following this regime, terminal flow is achieved where the individual polymer coils are no longer entangled with their neighbors and achieve liquid-like flow past one another.

The addition of nanoparticles to a polymer matrix with strong particle-polymer attractions has been shown to affect strongly the relaxation processes introduced above due to strong surface anchoring (from either adsorption or covalent grafting). For example, in terms of segmental dynamics, it was hypothesized chain segments closest to the particle surface were immobile, creating a "dead" or "glassy" layer.[54] More recently, it has been suggested that this interfacial layer is still mobile, although the relaxation time scales may be significantly longer than that of the bulk polymer.[55–59] In matrix-free grafted polymer nanocomposites, it has been shown that these systems behave akin to soft glasses and generally their dynamics are even slower than conventional mixed composites. [44,45,60,61] For example, Kim et al. reported studies on grafted chain dynamics in matrix-free systems, and found that for short *cis*-1,4-polyisoprene chains densely grafted to silica nanoparticles, chain dynamics are slowed by orders of magnitude compared to untethered chains.[61] These effects were most profound at low grafting density and molecular weights below M_e. To explain their findings of the larger separation between the chain dynamics and segmental dynamics in tethered chains versus untethered chains of comparable M_n, they proposed that grafted chains interpenetrate into the brushes of neighboring grafted particles in an attempt to uniformly fill the space between the particle cores. The entanglements between the grafted nanoparticles render the anchor points more or less "fixed", and the polymer chains become "jammed". In the jammed state, the energy required for the chains to disentangle and flow is higher than the thermal energy in the system. Similarly, for star polymers, researchers have found that for arm lengths longer than

the entanglement molecular weight, these systems must first undergo arm-retraction for the system to relax fully, adding an additional activated barrier for relaxation.[62–65]

Here we provide a systematic characterization of the dynamics of matrix-free grafted nanoparticles ranging from secondary relaxations through the terminal regime as a function of graft density and brush molecular weight, which has to date not yet been performed. We study the effects of grafting as well as confinement imposed by neighboring grafted particles on the relaxation mechanism of these systems. Using mechanical rheology in the linear regime, we show in the first half of Chapter 4 that the Rouse dynamics of the grafted polymer chains appear unaffected when compared to the pure polymer melt. However, the long-time reptation and diffusion of an entire grafted particle is slowed by several decades in frequency, and this retardation of dynamics is most heavily influenced by chain molecular weight. We postulate the slowed dynamics leads to the reduction in aging effects on the permeability. Additionally, we find a cross over molecular weight where these systems transition from a more liquid-like system to that of a colloidal solid. Interestingly, this transition appears in the same molecular weight range as the peak permeability enhancement detailed in Chapter 2. Therefore, we develop a scaling theory to explain how brush architecture affects the long-time diffusion and this mechanical transition. Furthermore, we comment on the effects of grafting on the mechanical properties of these materials using both linear and non-linear rheology, the latter of which is detailed in the second part of Chapter 4.

Acknowledging, however, that molecular diffusion occurs on much shorter time scales relative to that of polymer chain reptation, we also probe the segmental and secondary relaxation processes of GNPs and compare to those of the neat polymer melts using broadband dielectric spectroscopy (Chapter 5). We show that the presence of nanoparticles significantly slows the

segmental relaxation time, however in the grafted nanoparticle systems, the secondary relaxation processes shows non-monotonic behavior with molecular weight. For low and high M_n, the grafted system essentially follows the neat secondary dynamics. But for intermediate M_n, we see the grafted system has *faster* secondary dynamics than the corresponding neat. The faster secondary dynamics may further confirm there is more local free volume in the intermediate M_n grafted samples, and hence faster diffusion, that was explored in Chapter 2.

The behavior of matrix-free GNP materials is clearly more complex than that of conventional mixed composites. In addition to enhanced control of nanoparticle dispersion, these hierarchical systems have surprising transport and mechanical properties which would be unexpected from a purely combinatorial perspective. This class of materials may therefore have far ranging applications, a few of which we explore in the remainder of this thesis.

Chapter 2

Some of the content of this chapter is adapted with permission from C. R. Bilchak, E. Buenning, *et al.*, "Polymer-Grafted Nanoparticle Membranes with Controllable Free Volume," *Macromolecules*, vol. 50, no. 18, pp. 7111–7120, 2017. *Copyright 2017 American Chemical Society.*

Polymer-Grafted Nanoparticle Membranes with Controllable Free-Volume

Baker[13,24], suggests that the best hopes for transformative improvements in membrane performance is by using novel materials and constructs, including metal-organic frameworks, molecular sieve materials, and mixed matrix membranes. Our method, then, to creating next-generation gas separation materials is that of matrix-free polymer grafted nanoparticle membranes. This approach naturally circumvents the issues of phase separation between the inorganic nanoparticle core and the organic polymer tether, by a phenomenon that is analogous to microphase separation in diblock copolymers.[66–68] Computer simulations demonstrate that these systems must reconcile the conflicting drive for the nanoparticles to locally order against the polymer chains having to distort to fill the interstices (see below). This competition evidently creates spatial regions of somewhat lower density over a range of polymer graft densities and chain lengths. Multiple experimental probes verify this picture, and imply that this additional free volume in the composites leads to *elevated* permeabilities for both light gases and condensable solutes. Thus, one can manipulate solute permeabilities predictably by varying graft density and chain length. The grafting process is also shown to mechanically reinforce the polymer. Importantly, aging effects for glassy systems are significantly reduced by the presence of the nanoparticles, a significant advantage over conventional synthetic schemes to increase free volume

using pure polymers. This new construct therefore offers multiple benefits in the context of gas separation membranes.[13]

2.1 Materials and Methods

In this section, we briefly describe the synthetic pathway of the grafted nanoparticles and the experimental protocols for transport measurements. More detailed synthetic information and experimental details for other test methods can be found in Appendix A.

2.1.1 Material Synthesis and Sample Preparation

Polymethylacrylate (PMA) and poly(methylmethacrylate) (PMMA) grafted nanoparticles were synthesized by surface initiated reversible addition-fragmentation chain transfer polymerization (SI-RAFT) technique (see section A.1 for more detailed information on the nanoparticle synthesis).[69,70] The RAFT agent 2-(dodecylthiocarbonothioylthio)propanoic acid (DoPAT) was used for the RAFT polymerization. All chemicals were obtained from either Fisher or Acros and used as received unless otherwise specified. Spherical silica nanoparticles (14±4 nm diameter) were obtained from Nissan Chemical. 3-Aminopropyldimethylethoxysilane was purchased from Gelest, Inc. DoPAT was purchased from Boron Molecular, Inc. Methyl acrylate (MA, 99%, Acros) and methylmethacrylate (MMA, 99%, Acros) were purified by filtration through an activated basic alumina column. Azobisisobutyronitrile (AIBN) was twice recrystallized from ethanol before use.

A typical example of the polymerization method is described here: DoPAT functionalized nanoparticles (DoPAT-NP) (0.35g, 0.43 chains/nm^2) were dispersed in 14mL DMF and 7.37mL methyl acrylate (0.081 mol). AIBN, dissolved in DMF (0.356mL, 0.01M), was added to the

solution, and finally the mixture was transferred into a dried Schlenk flask. (The methymethacrylate polymerization followed the literature.[70])

The mixture was degassed, backfilled with nitrogen, and then placed in an oil bath at 60 °C. The polymerization solution was quenched in ice water after 2.25 hours. THF (20mL) was added to the flask and the solution was poured into hexanes (120mL) to precipitate PMA-grafted nanoparticles. The PMA-grafted silica nanoparticles were recovered by centrifuging at 3000 rpm for 10 min. The nanoparticles were subsequently dispersed in 50mL THF and precipitated in 100ml methanol. This dispersion-precipitation process was repeated another five times to collect the grafted nanoparticles. Molecular weights and dispersity were determined using gel permeation chromatography (GPC) equipped with a Varian 290-LC pump, a Varian 390-LC refractive index detector, and three Styragel columns (HR1, HR3 and HR4, molecular weight range of 100-5000, 500-30000, and 5000-500000, respectively). THF was used as eluent for GPC at 30℃ and a flow rate of 1.0 mL/min. The GPC was calibrated with poly (methyl methacrylate) (PMMA) standards obtained from Polymer Laboratories. Graft densities were determined using thermogravimetric analysis (TGA).

The antioxidant Irganox 1010 was added at 0.25wt.% relative to the polymer to minimize oxidation during any subsequent annealing. All solid composites were cast from THF and dried in a covered PTFE petri dish for 2 days, then annealed under vacuum at room temperature for 8 hours, and finally under vacuum at either 80^{o}C (PMA materials) or 150°C (PMMA materials) for an additional 3 days before any further characterization. All thin-film composites were spin-cast (Laurell Technolgies, North Wales, PA) from 50-80mg/ml THF on to the chosen substrate. Prior to spin coating, the substrates were immersed in piranha solution (3:1 mixture of 18M sulfuric acid and 30% hydrogen peroxide/water solution (Fischer Scientific, NJ)) for approximately one minute.

Substrates were then rinsed with deionized water and methanol three times each and cleaned in a UV/O_3 chamber for 15 minutes to grow a surface oxide layer of 1.5nm as measured by ellipsometry (α-SE spectroscopic ellipsometer, J.A. Wollaam). The films were then annealed in the same manner described above. Details of materials used in this study are found in Table 2.1 and Table 2.2 for PMA and PMMA-based materials, respectively. However, due to exceptionally limited quantities of material, we are unable to report weight fractions of the low graft density (σ=0.07chains/nm^2) PMA grafted particles and some PMMA grafted particles.

Table 2.1: PMA-based materials used for transport studies.

Graft Density Σ (chains/nm²)	**Molecular Weight M_n g/mol**	**Polydispersity Đ**	**Volume Fraction ϕ_{SiO_2}**
Neat PMA	25,600	1.07	N/A
	46,100	1.11	
	65,000	1.14	
	77,600	1.12	
	96,500	1.16	
	135,000	1.20	
0.43	26,900	1.14	0.20 ± 0.006
	38,100	1.11	0.15 ± 0.008
	62,000	1.13	0.10 ± 0.006
	77,100	1.15	0.081 ± 0.007
	92,100	1.13	0.059 ± 0.003
	132,100	1.18	0.036 ± 0.001
0.07	22,900	1.18	*unavailable*
	52,900	1.21	
	72,000	1.24	
	103,000	1.18	
	158,200	1.16	

Table 2.2: PMMA-based materials used for transport studies

Graft Density **Σ** **chains/nm²**	**Molecular Weight** M_n **g/mol**	**Polydispersity** **Đ**	**Weight Fraction** ω_{SiO_2}
Neat PMMA	24,100	1.13	N/A
	60,400	1.08	
	111,600	1.14	
0.44	25,300	1.07	0.25
	62,400	1.08	0.13
	69,200	1.10	*unavailable*
	78,200	1.13	0.10
	90,400	1.13	*0.091*
	113,600	1.17	*unavailable*

2.1.2 Steady-State Permeation

Steady-state permeability of small gases was measured with a closed-volume manometric apparatus previously described elsewhere.[71] Films were solvent cast from solutions of 35-50 mg/ml of sample in THF in tall-form Teflon petri dishes, with thicknesses ranging between 35-50 microns. The films were then exposed to an upstream gas species i at ≈1.3bar (gauge), and permeability P_i was calculated from the flux as the gas was allowed to diffuse through the membrane into a downstream chamber of known volume for at least 1 hour using the relation:

$$P_i = \frac{V\ell}{RTA\,\Delta p}\left(\frac{dp_d}{dt}\right)_{t\to\infty} \tag{2.1}$$

where Δp is the pressure difference across the membrane, ℓ is the sample thickness, A is the sample area, V is the volume of the downstream chamber, R is the universal gas constant, and dp_d/dt is the rate of change of the downstream pressure. Temperature, T, was held constant at 35°C. CO_2, CH_4, and N_2 were tested for σ =0.43 chains/nm^2 composites with graft M_n 27kDa

38kDa, 62kDa, 92kDa and 132kDa. nC_4H_{10} was tested for PMA composites with M_n 38kDa, 62kDa, 92kDa and 132kDa. Neat PMA data were taken from Chiou et. al., 1985[72] for comparison purposes, and was independently measured using QCM sorption experiments (see below). Neat PMMA data was taken from Robeson, 1991[73] and also compared with QCM experiments.

2.1.3 Non-Steady State Diffusion with Quartz Crystal Microbalance

The quartz crystal microbalance (QCM) technique is used to measure K_i and D_i for both light gas and condensable vapors penetrants through monitoring of the mass uptake of a chosen penetrant into a polymer film deposited on a quartz crystal. This allows for highly precise measurements of solubility and diffusion constants. QCM transducers are driven at the fundamental resonant frequency by a feedback control oscillator. For light-gas experiments, we use a QCM with dissipation monitoring (QCM-D) (Biolin Scientific) which allows us to measure the energy dissipation as well as higher harmonics as a film oscillates. This allows for superior noise reduction and measurements of much subtler frequency changes. For organic solvent penetrants we use "standard" QCM instrumentation (i.e. no dissipation monitoring), (Inficon Inc.). QCM crystals with gold electrodes for light gas experiments (14mm diameter, AT-cut 34°10', nominal bare frequency at 4.95Hz) were purchased from Biolin Scientific. Crystals for vapor penetrants experiments (1-inch diameter, AT-cut, 5MHz nominal frequency, 10 Ω nominal resistance) were purchased from Inficon Inc. As-received crystals were cleaned according to procedures above. Bare crystal resonant frequencies and resistances (f_q and R_q, respectively) were recorded using either a Biolin QSesne Explorer QCM-D or a Maxtek RQCM (Inficon Inc.) for light gas and vapor sorption experiments, respectively, prior to spin coating polymer films to check for crystal integrity and "taring" for use as a microbalance. Multiple data readings in two separate holders were taken for each crystal to ensure accuracy, and did not vary by more than ±2Hz, or

±0.01Ω. Crystals with initial resistances greater than 10.5Ω indicate damage and were either re-cleaned as described above or discarded.

Polymer and polymer nanocomposite films were cast on the cleaned quartz crystals via spin coating. Films were spun at speeds ranging from 900-1100rpm for 55-60 seconds. Film thicknesses were measured using ellipsometry and confirmed with a Datek contact profilometer post-test. Thickness values from these two techniques agreed to within 10nm for both neat and composite materials. Both neat PMA and composite films spun under these conditions yielded film thicknesses of 550-600nm. Uniform films with thicknesses of 85-2000nm can be easily prepared using this technique. The crystals were loaded into the respective QCM instrument and gas or vapor penetrants were then flowed over the crystal, while the frequency change of the sensor is monitored throughout the experiment. This provides *in situ* mass uptake measurements of the penetrant in the polymer film. Penetrant flow rates and compositions are controlled using a custom gas handling apparatus equipped with mass flow controllers (Alicat Scientific, Tucson, AZ). Extensive information about the gas handling system, as well as QCM experimental procedure, is provided in Appendix A.

2.2 Transport in Matrix-Free Polymer Grafted Nanoparticles

Here we present transport data for several neat and grafted composite systems for a variety of gases as well as solvent vapor. Additional transport data, including experimental controls, can be found in Appendix B. We provide materials characterization in order to determine how grafting polymers to the surface of nanoparticles affects the transport properties of small penetrants in thin membranes.

2.2.1 Diffusion of Light Gases

Figure 2.1A shows the ideal selectivity of CO_2 over CH_4 as a function of CO_2 permeability in PMA-grafted nanocomposites compared with that of neat PMA. P_i's from freestanding 50μm thick films of the grafted nanoparticles by steady state permeation are in quantitative agreement with data on supported ~0.5-1.5μm thick films by QCM. These data indicate that permeability is unaffected by thickness in this range.[74,75] Figure 2.1B shows analogous QCM results from ≈1μm thick spin-cast films of PMMA grafted nanoparticles. Clearly, the grafted nanocomposites *do not* follow Maxwell's theory, which would predict decreases in permeability and no changes in selectivity, but rather display *enhanced permeability* relative to the corresponding neat polymers. It is important to note that these enhancements occur in both rubbery and glassy materials.

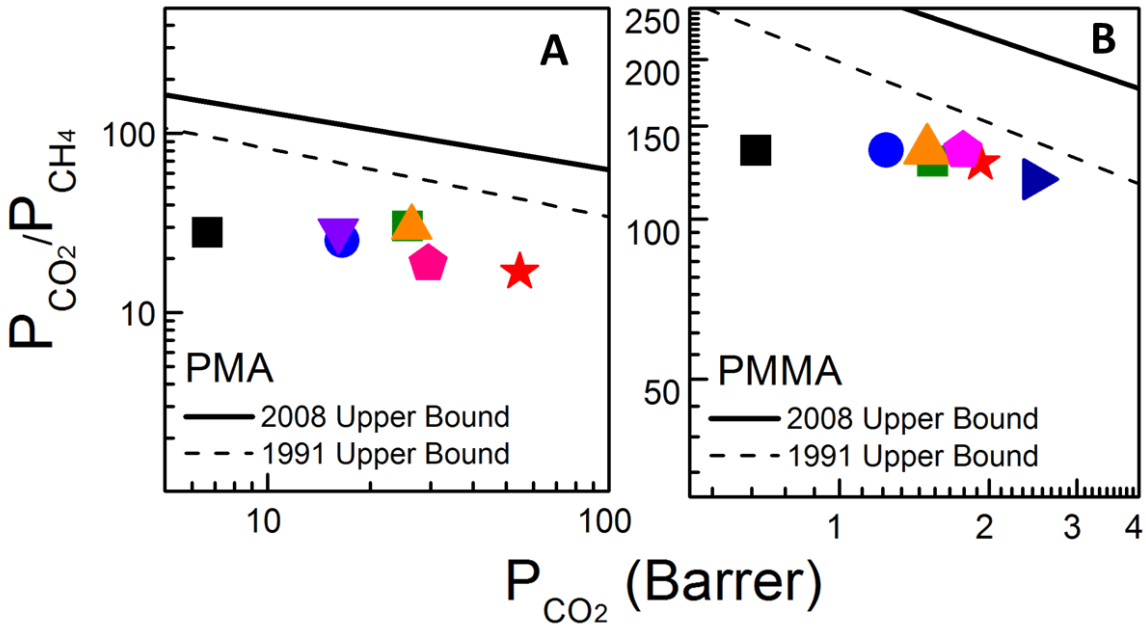

Figure 2.1: Robeson plots comparing the permeabilities of CO_2 and CH_4 in (A) PMA- and (B) PMMA-grafted nanoparticle composites for various brush M_n. [11] PMA composites with graft lengths of (●) 27kDa, (▼)38kDa, (⬟) 52kDa, (■) 62kDa, (★) 92kDa, and (▲) 132kDa compared with (■) neat PMA. PMMA composites with graft lengths of (●) 27kDa, (■) 62kDa, (⬟) 69kDa, (▶) 78kDa, (★) 90kDa, and (▲) 113kDa, compared with (■) neat PMMA. $\Sigma \approx 0.4$chains/nm^2 for both PMA and PMMA grafted particles.

The observed permeability enhancements can be analyzed from two viewpoints. First, the slope of the PMA data on a Robeson plot decreases as the size disparity of the gas pairs becomes larger (Figure 2.2A $m_{C_4H_{10}} < m_{CH_4} < m_{N_2}$). The slope of CO_2/CH_4 data (-0.31) is in good agreement with literature values of the upper bound slope for this gas pair (-0.30). It has been theorized previously[11] that the upper bound slope is related to the relative sizes of the gas molecules being considered; this serves as an indication that the grafted nanoparticle membranes are separating the gas pairs based on size sieving, and not on solubility differences.

Furthermore, the enhancements in P_i can be controlled effectively by variations in chain length. Figure 2.2B shows a non-monotonic trend ("volcano plot") for permeability as a function of PMA graft M_n at a fixed grafting density (σ= 0.43 chains/nm^2) for CO_2, N_2, and CH_4. nC_4H_{10} also shows the same trends, and similar results are found for the PMMA analogs (Appendix B, Figure B- 10). As an illustrative example, we focus on the relative permeability, P_ϕ/P_b, of CO_2. The permeability of grafted nanoparticle composites with short chains (<50kDa) shows a distinct increase when compared to the pure polymer and the Maxwell model (which predicts $P_\phi/P_b \leq 1$ for all M_n), with the degree of enhancement increasing with M_n. P_ϕ/P_b then increases substantially at intermediate chain lengths, before decreasing at large chain lengths. However, these large chain length materials still have $P_\phi/P_b>1$, indicating they are more permeable than pure PMA. The PMA composite displaying the maximum permeability in this series (i.e., M_n= 92kDa) is the same for all four gases and shows about an order of magnitude increase relative to the pure polymer; for example, P_{CO_2}= 56.1$\pm$0.1 Barrer in the most permeable PMA composite, but it is only 6.7$\pm$0.15 Barrer in the pure PMA (See Figure B- 8).

Figure 2.1A further shows that there are only minor changes in selectivity of CO_2 over CH_4 even when the CO_2 permeability increases by nearly an order of magnitude; For example,

P_{CO_2}/P_{CH_4} of the most permeable composite deceases by ≈ 35% when P_{CO_2} increases by over 800%. Similar results are found for the PMMA systems, Figure 2.1B where P_{CO_2}/P_{CH_4} appears to be even less affected. The selectivity of CO_2 over N_2 is also unaffected across the same range in CO_2 permeability in the PMA composites (Figure 2.2A and Figure B- 9). Evidently, these grafted nanoparticle composites exhibit unexpected shifts to the "right" on the Robeson plot when M_n changes, towards the upper bound, with the best PMMA system nearly on top of the 1991 upper bound.[12]

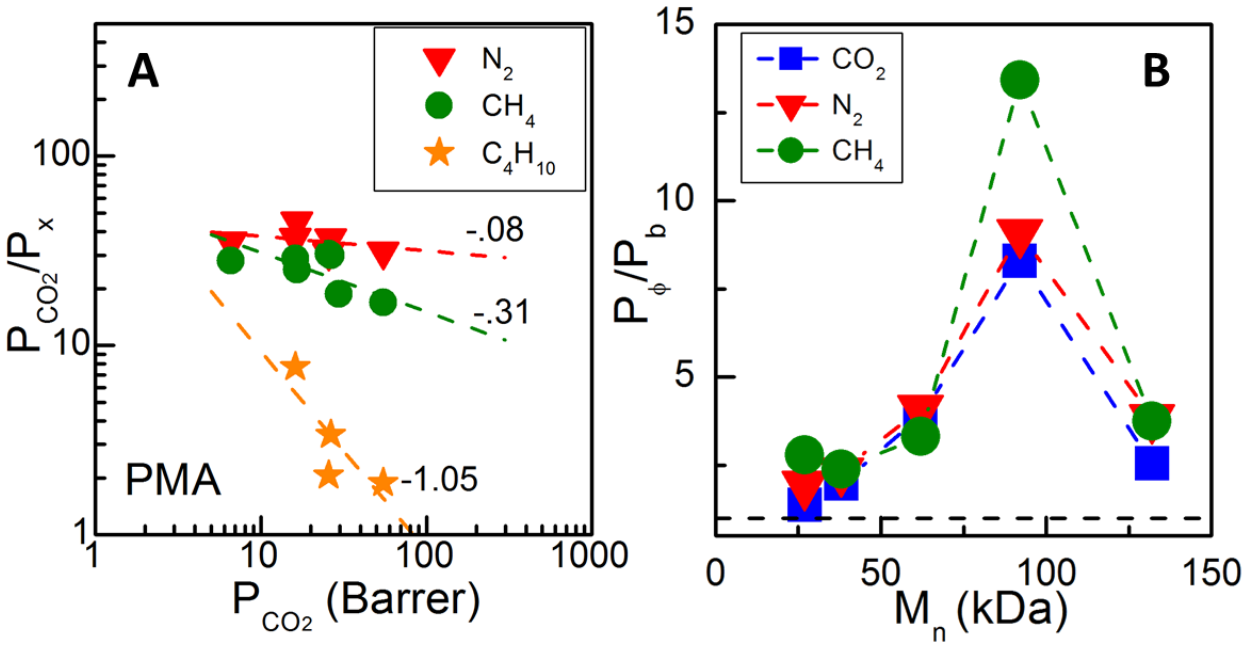

Figure 2.2: Gas permeability properties of PMA-grafted nanoparticles (Σ= 0.43 chains/nm^2). (A) Comparison of the slopes of the selectivity/permeability line for CO_2 and three light gases. The slope of the line decreases monotonically as the size disparity between the gas molecules increases; the slope of the CO_2/CH_4 line agrees with literature. (B) Increases in measured gas permeability relative to that of neat PMA (i.e., "volcano plot") for grafted systems. Neat PMA is presented as a dashed line at $P_\phi/P_b = 1$

Note that these materials are competitive with commercial cellulose acetate membranes with respect to CO_2 permeance, a measure of permeability that has been normalized to the

thickness of the material being considered. For example, a 500nm thick PMA composite film with M_n= 92kDa has a permeance of 115GPU, which is comparable to that of commercial cellulose acetate (≈100GPU).[76]

2.2.2 Permeability Enhancement Driven by Free Volume

The "volcano" shape of relative permeability versus PMA graft M_n at fixed σ = 0.43 chains/nm^2 (Figure 2.2B) is remarkably similar to trends observed for the free volume element size from positron annihilation lifetime spectroscopy (PALS) (Figure 2.3, Figure 2.4A).[33,34]

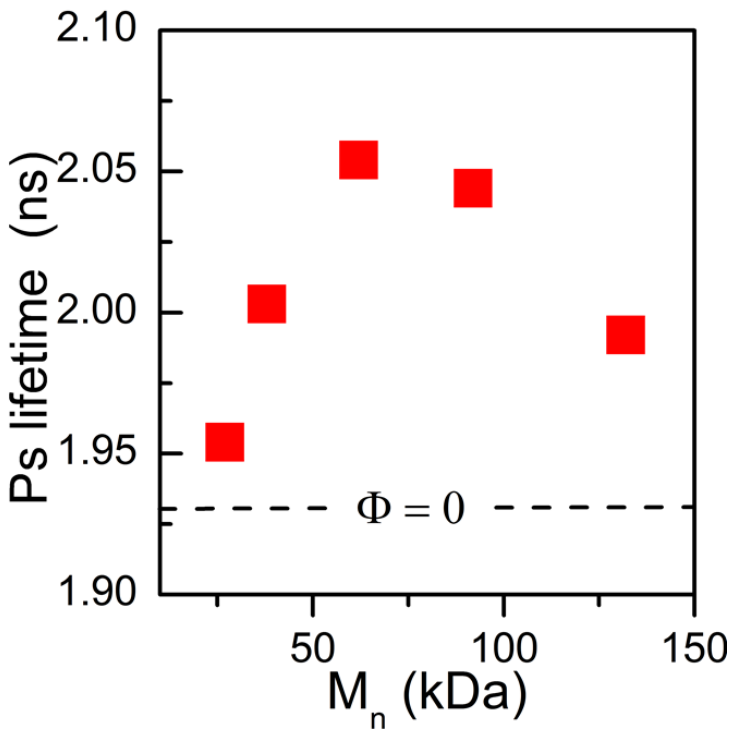

Figure 2.3: Single-fit positron (Ps) lifetime in PMA composites

The lateral size for the PALS-derived free volume "elements" is 4-5Å, comparable to the Kuhn length of the polymers, consistent with the local fluctuating nature of this free volume metric. The apparent connection between enhanced free volume and "static" excess volume is supported

by room temperature pycnometry, which is used to compute the excess volume $\tilde{V}$ relative to volume additivity: $\tilde{V} = \frac{1}{\rho_c} - \frac{\omega_{NP}}{\rho_{NP}} - \frac{\omega_{poly}}{\rho_{poly}}$, where ω is the weight fraction, ρ is the density and the

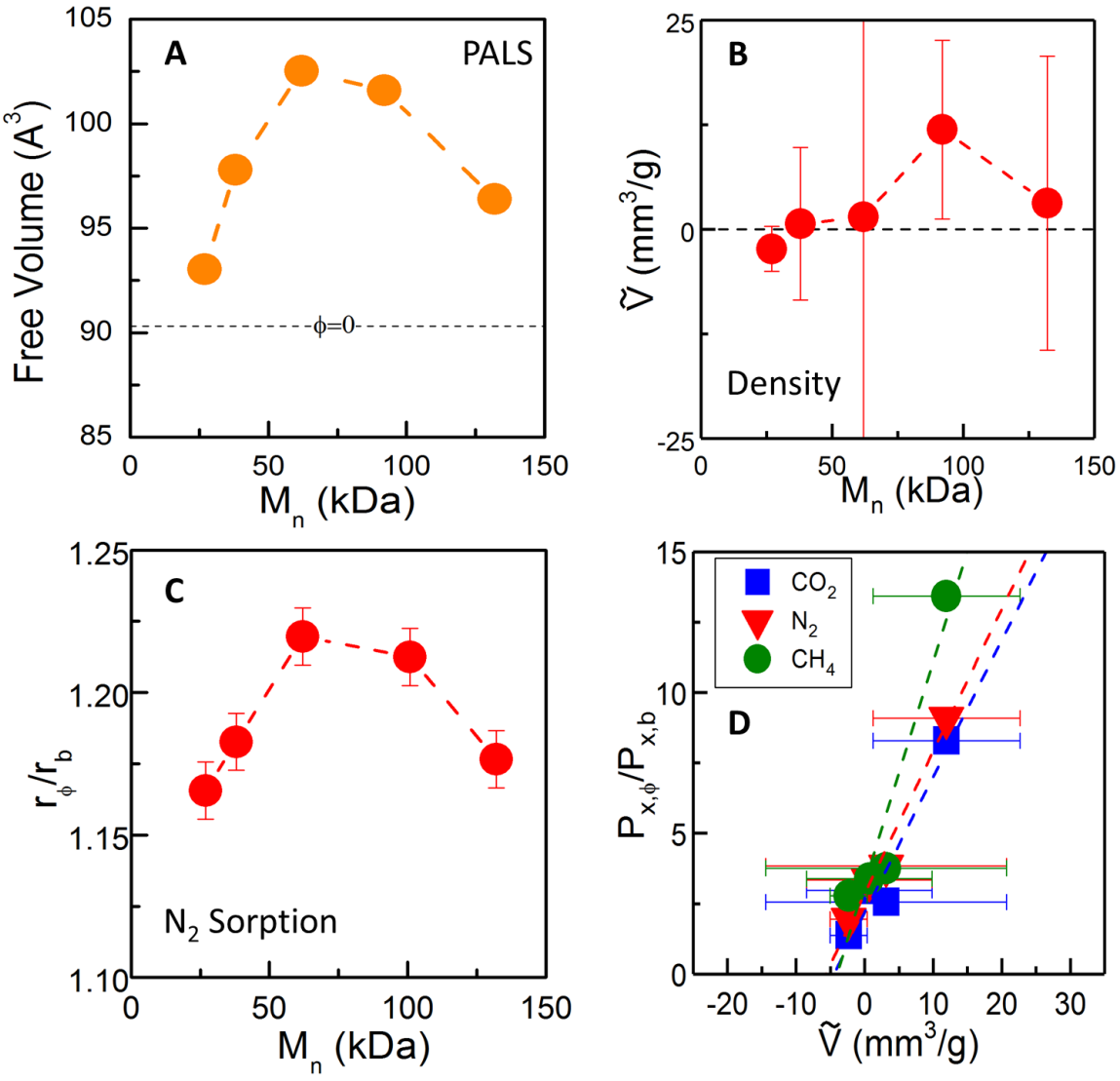

Figure 2.4: Free volume metrics for PMA-grafted NP Composites (Σ=0.43cchains/nm^2). (A) Measured free volume element size from PALS experiments as a function of the composite brush M_n. The volume size clearly displays a non-monotonic $M_n$dependence. (B) Excess volume $\tilde{V}$ computed from pycnometry experiments. $\tilde{V}$ can be related to Fractional Free Volume, FFV (see supplementary information). (C) Relative apparent pore sizes (r_i) in composites from N_2 isotherms. The pore size increases found from sorption and free volume element sizes measured from PALS are strongly correlated (see Supplementary information). (D) Correlation between relative gas permeability increases and $\tilde{V}$ for the three light gases examined

subscripts c, NP and $poly$ denote the composite, nanoparticle, and polymer, respectively. Despite the large relative error arising from uncertainty in ω_{NP}, it is clear that the intermediate chain length systems have the largest excess volume, Figure 2.4B. The silica volume fraction (ϕ) was calculated as:

$$\phi = \frac{\omega \rho_c}{\rho_{SiO2}} \tag{2.2}$$

where ρ_{SiO_2} and ρ_c are the density of bare silica nanoparticles and the PMA composites, respectively. The effective density of the polymer brush in the composite can be estimated based on volume additivity:

$$\rho_{m,eff} = \frac{(1-\omega)\rho_c}{(1-\phi)} \tag{2.3}$$

A summary of ω, ϕ, and ρ data are shown in Figure 2.5. The data indicate while the density of neat PMA is relatively independent of molecular weight, $\rho_{m,eff}$ in PMA composites is up to 1% *lower* than bulk PMA melts of comparable density, with a local minimum for moderate chain length. These slight reductions in polymer phase density can indicate significant enhancements in available "free volume". This is further reinforced by the good correlation between $\tilde{V}$ and the relative permeability increases for CO_2, N_2, and CH_4 as shown in Figure 2.4D. It should be noted that the relatively large error in $\tilde{V}$ arises from the error in measurements of ω and not in the measurement of ρ_c from pycnometry.

An additional important metric for gas transport via a free volume mechanism is the fractional free volume (FFV), a method of comparing the amount of free volume in polymers. Merkel et al. suggest the following relation based on material specific volumes[38]:

$$FFV = \frac{V_{sp} - V_0}{V_{sp}} \tag{2.4}$$

V_{sp} is the polymer bulk specific volume; in this case we use the effective matrix specific volume of the composites derived from $\rho_{m,eff}$. V_0 is the volume taken up by the polymer chains and cores, and may be estimated using the van der Walls volume (V_{vdw}) and group contribution methods:

$$V_0 = 1.3V_{vdw} \tag{2.5}$$

We use the calculation of V_{vdw} proposed by Zhao et al. to estimate the polymer chain volume of

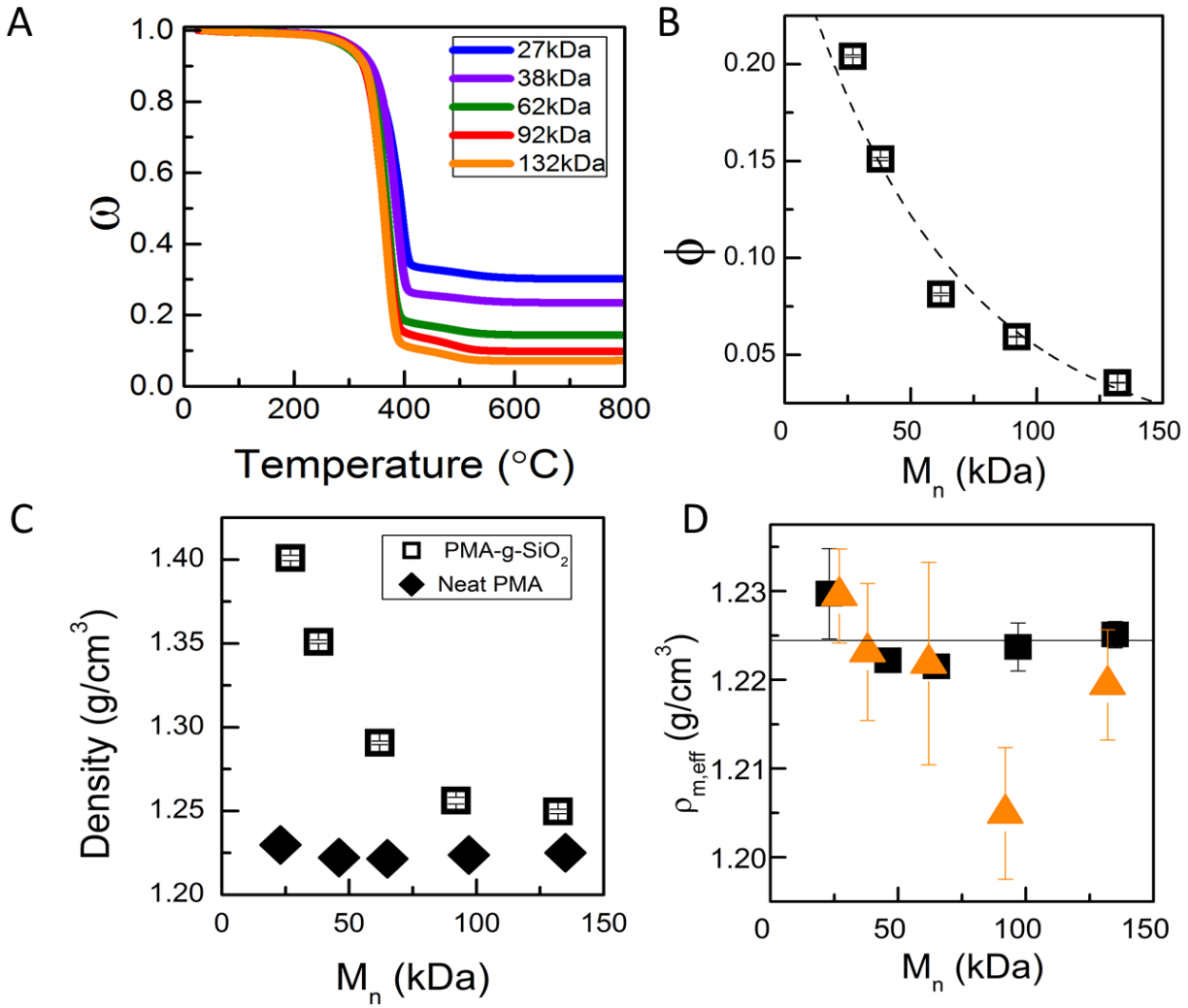

Figure 2.5: PMA Materials Characterization. (A) Thermogravimetric analysis signature for PMA composites; (B) Volume fraction of silica nanoparticles of PMA composites of various M_n (Σ = 0.43chains/nm^2). Error bars within symbol; (C) Raw densities of PMA composites (Σ = 0.43chains/nm^2) compared to neat PMA (◆). Error bars within symbol; (D) Effective polymer matrix density of the composites (▲) compared with that of neat PMA (■) as a function of M_n

each brush molecular weight.[77] A comparison of FFV between the composites is shown in Figure 2.6A. Neat PMA FFV was estimated by using the average measured specific volume of 23kDa, 46kDa, 65kDa, 97kDa, and 135kDa samples. The composites at intermediate chain length clearly have a substantially increased FFV, with a maximum FFV in 92kDa composites. Even with the

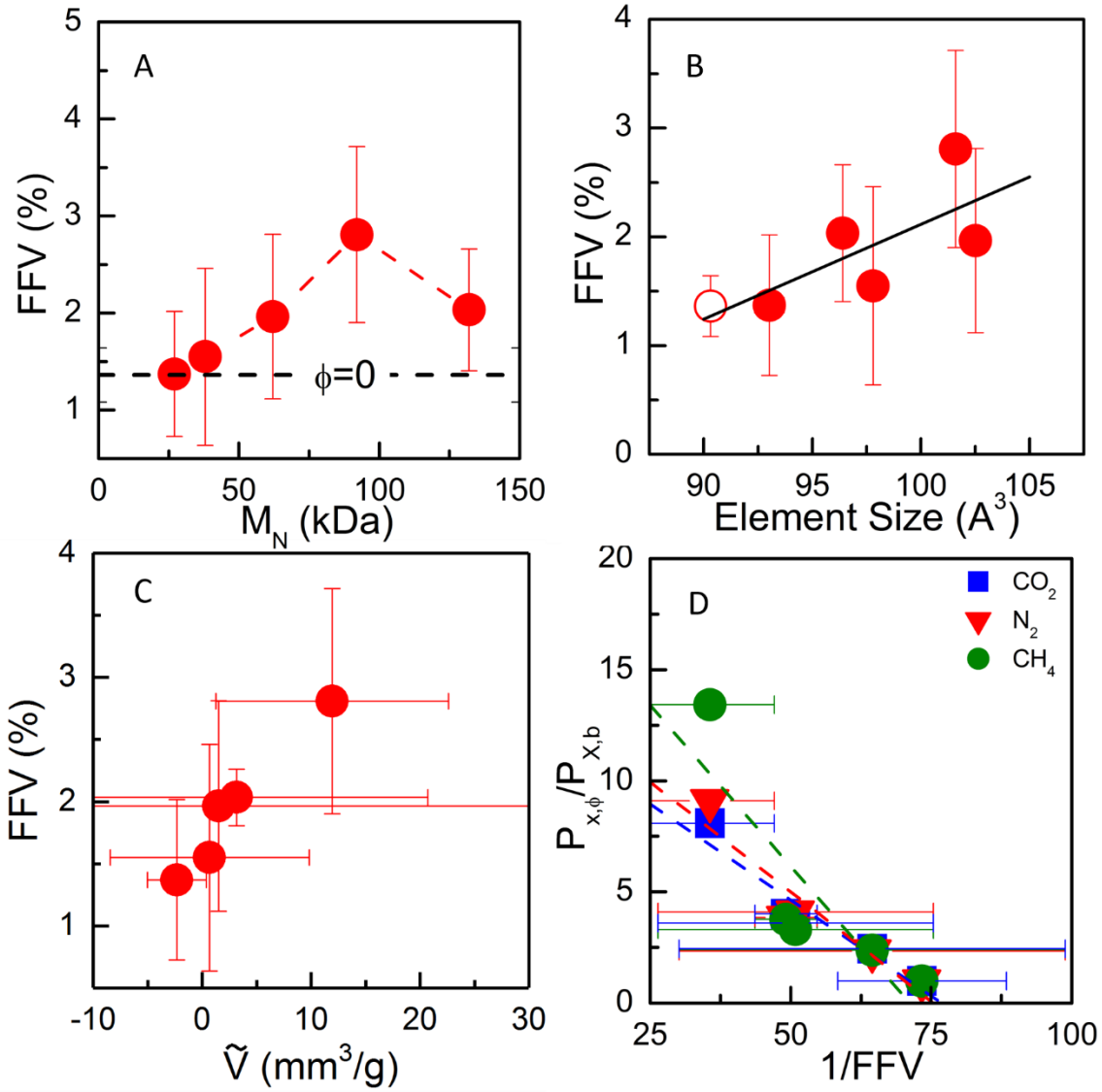

Figure 2.6: Excess Volume and Fractional Free Volume Measurements. (A) Calculated Fractional Free Volume (FFV) of PMA composites compared to neat PMA; (B) Correlation of FFV with free volume element size of PMA composites (●) and neat PMA (◯) as measured by PALS; (C) Correlation of FFV and excess volume determined by pycnometry; (D) Relative permeability dependence on 1/FFV for three light gases.

large error bars, it is clear that some composites possess FFVs significantly different than that of the neat PMA melt. Furthermore, the FFV and calculated $\tilde{V}$ correlate very well (Figure 2.6B**)**. This result is unsurprising as both measurements are related to the composite brush density which displays similar trends with molecular weight. The correlation between FFV and free volume element size measured from PALS is shown in Figure 2.6C. Again, despite the large error in FFV, the two measures of free volume correlate reasonably well within the uncertainty of the measurements. The quantity 1/FFV also correlates well with the relative gas permeability increases in the composites (Figure 2.6D). Since the excess volume is related to the fractional free volume (FFV),[33] the data indicate that intermediate M_n possesses the highest amount of FFV (Figure 2.6).

Finally, this excess volume can also be indirectly probed using N_2 adsorption isotherm data at 77K, where the material is glassy. With the caveats that this measurement is sensitive to sample preparation and to the amount of time the sample is held at 77K during the measurement, this provides a measure of the frozen, static pore size in the medium. Presumably, this is related to the pycnometry data in the room-temperature liquid state. The PMA composites clearly exhibit higher apparent pore sizes and surface areas from BET model fits (Figure 2.4C and Figure A- 5D), again implicating volume increases. Indeed, the excess volume from pycnometry and macroscopic gas permeabilities are linearly correlated (Figure 2.6D). Each of these facts support the hypothesis that free volume changes result in the permeability enhancements seen in the polymer-grafted nanoparticle membranes.[19,33]

2.2.3 Condensable Penetrant Experiments

Linear sorption measurements using the QCM apparatus allows for the independent measurement of K_i and D_i in supported films in the thickness range 300-1500nm, much closer to

thicknesses used in industrial applications than those used in permeation experiments. Experiments that directly measure both K_i and D_i can also provide insight as to how these properties are altered in the different nanoparticle composites, and their individual contributions to the observed permeability increases. Figure 2.7shows results for a condensable solute, ethyl acetate, in PMA composites with σ = 0.43 chains/nm^2 at fixed penetrant partial pressures (additional grafting densities and partial pressures are in Appendix B section B.3). As with the light gases, the permeability of ethyl acetate in the grafted system is elevated relative to neat PMA (and the Maxwell prediction) for low M_n (Figure 2.7A). As PMA M_n increases, a prominent maximum in permeability is seen with $P_\phi/P_b \approx 4$ at intermediate M_n (62kDa). For larger M_n, the relative permeability decreases, but remains above the neat polymer. We find that K_i is increased by only ~30% independent of M_n, indicating somewhat enhanced sorption in these elevated free volume structures, but that the chain length does not appear to have any significant effect. By contrast, the D_i increases by a factor of ≈3, qualitatively similar to the trends observed for P_i (Figure B- 4D and Figure B- 4C, respectively). This indicates that the permeability enhancements

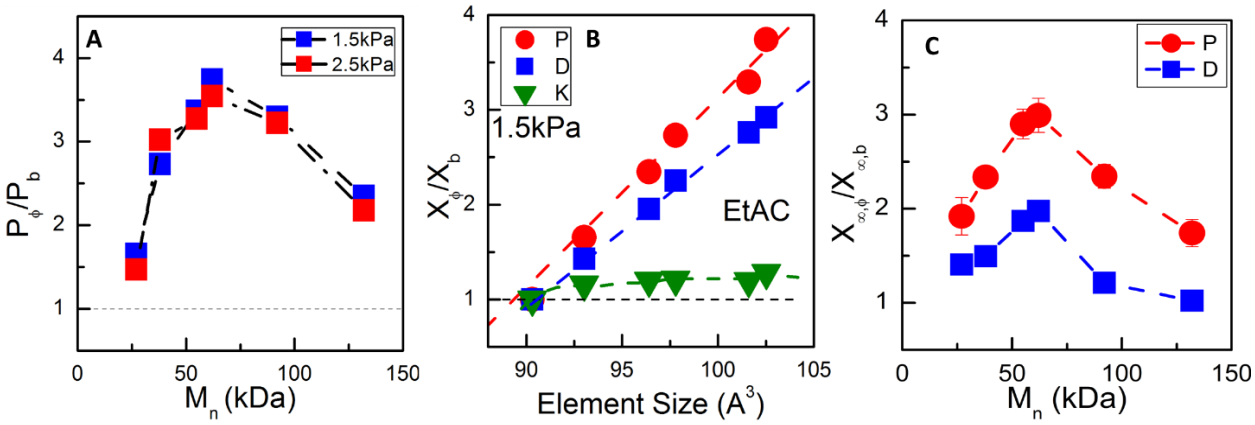

Figure 2.7: Transport properties for a condensable solute in PMA composites (A) "Volcano plot" of relative permeability of ethyl acetate as a function of M_n at two partial pressures. (B) Correlation of P_ϕ/P_b (●), D_ϕ/D_b (■), and K_ϕ/K_b (▼), for ethyl acetate versus free volume element size as measured by PALS for a single experimental partial pressure; (C) Relative increase of P_i and D_i at infinite dilution for ethyl acetate as a function of PMA graft M_n.

seen here are a direct result of elevated diffusion. Analogous with the P_i from the light gas permeation, we find excellent correlation between the "free volume element" size, in this case derived from PALS, and P_i and D_i (Figure 2.7B). Importantly, the data indicate that the increase in relative permeability is primarily due to changes in D_i, consistent with permeability enhancement via free volume. Extrapolation of P_i and D_i to the infinite dilution limit (Figure 2.7C), show the same trends, and clearly indicate that the changes observed reflect an inherent membrane property, and not a solute concentration effect. This implies that the composite materials are natively more permeable than the corresponding neat polymer, a fact that is supported by the increased free volume as measured by PALS and excess volume measured by pycnometry. This is also consistent with the slope of the CO_2/CH_4 Robeson line in Figure 2.1A, which argues against solubility-driven effects.

2.2.4 Aging Effects

Importantly, we find no measureable effects on CO_2 permeability despite aging for up to 10 weeks for the PMMA composites (Figure 2.8A). This is in contrast to the permeability of CO_2 in neat PMMA, which decreases by up to 25% over the same 10-week time frame. These data show that performance degradation in glassy PMMA can be significantly reduced when the chains are grafted to nanoparticles. This has important practical implications for polymer membrane materials that have superior transport properties but undergo severe aging, such as PIMs and TR polymers.

Figure 2.8B illustrates that the PMA grafted nanoparticle systems show no aging effects in the presence of the ethyl acetate for up to 1 year. Additional aging experiments (Appendix B, Figure B- 5) show that the permeability of similar PMA-grafted nanoparticle composites (σ=0.07chains/nm^2) remains constant for up to 2 years. This result in rubbery materials is

particularly interesting due to the tendency of ethyl acetate and other condensable penetrants to cause significant structural rearrangement in physical mixtures of nanoparticle and PMA, which may alter transport properties.[40] This provides evidence that the nanoparticle composite materials are stable, even in the presence of high loadings (~10%wt) of solvent. Chemical stability such as this is advantageous in many industrial membrane applications, including methanol/MTBE vapor separations and robustness against contaminant poisoning.[13]

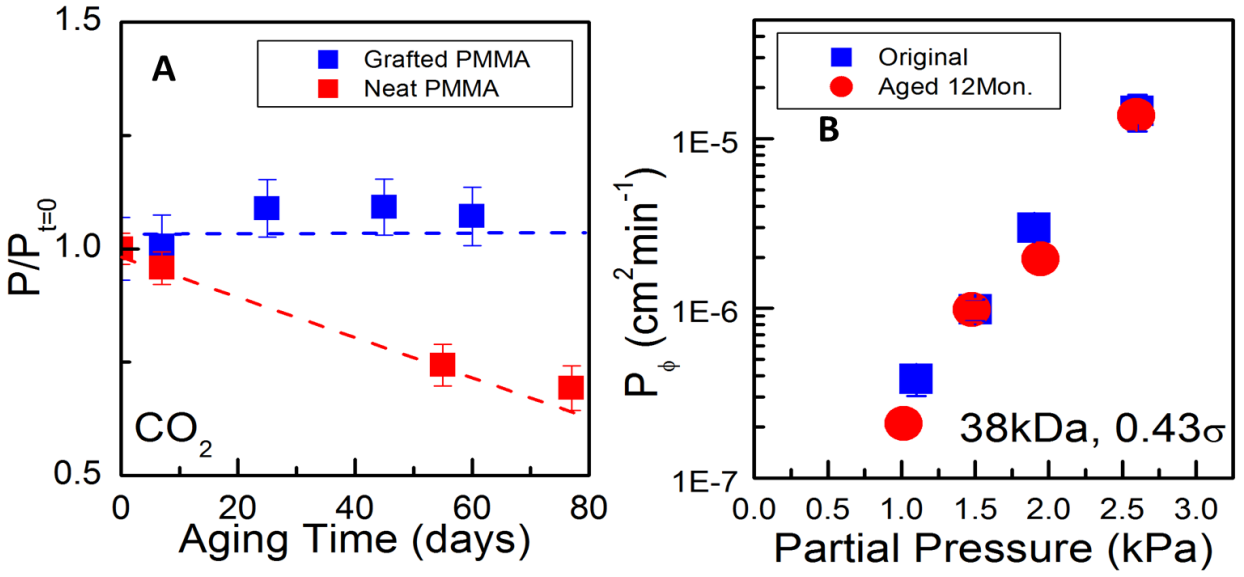

Figure 2.8: Aging of neat and nanoparticle composite polymer films. (A) Effect of aging time on CO_2 permeability in neat PMMA and in a PMMA-grafted nanoparticle composite with M_n =62kDa and Σ= 0.44 chains/nm^2. (B) Time dependence of ethyl acetate permeability in a grafted composite. Additional time points and samples are shown in the supplementary information.

2.2.5 Computer Simulations

To further support the proposed free volume picture, we simulated isolated polymer-grafted nanoparticles using a coarse-grained model. Figure 2.9A-C show a series of ensemble averaged conformations of single particles (diameter=7, monomer diameter=1) with 30 chains each with chain lengths of (Figure 2.9A) 5, (Figure 2.9B) 10, and Figure 2.9C) 30 monomers. If we were to naively scale both the nanoparticle size and the brush size to be commensurate with

the experiments then these simulations would correspond to PMA M_n of 40k, 130k, and 300k at a fixed graft density of σ = 0.7 chains/nm^2, which is higher than the experimental graft densities discussed in this study.

Figure 2.9C shows that, for sufficiently long grafted chain lengths, the corona appears isotropic, which presumably facilitates crystallization in other matrix-free grafted nanoparticle systems. In contrast, the nanoparticles with shorter chain length grafts have asymmetric corona shapes. It is important to note that these single particle simulations are performed in the absence of any other particles (i.e., the particles are in dilute solution) and will not necessarily represent the conformation of the polymer corona in the presence of other nanoparticles.

To investigate the polymer corona structure at higher nanoparticle concentrations, we also simulated multi-nanoparticle systems where the nanoparticles are placed on a face centered cubic (FCC) lattice. The simulation snapshots shown here are composed of 200 polymer chains, each with 10 monomers, grafted onto a nanoparticle with a diameter of 10 monomers. Figure 2.9D highlights the nanoparticle cores. Ongoing studies are relaxing this assumption and are allowing the nanoparticles to form the structures that they prefer – the results of this more sophisticated analysis is deferred to future work. To accommodate this nanoparticle packing, the grafted coronas are forced to assume anisotropic shapes to fill the interstitial spaces and attempt to maintain a uniform polymer density, Figure 2.9E. In fact, the corona shape is consistent with the Wigner-Seitz cell of the FCC lattice, namely a rhombic docadecahedron**.** Thus, chains located along the [011] direction are compressed, while chains along the [001] direction stretch to fill the interstitial space between the spherical cores. Figure 2.9F shows monomer density profiles as a function of radial distance away from the center of a particle core, expressed in units of monomer size σ. Monomers near the surface of the particle (for example, at σ=5) appear to have densities similar

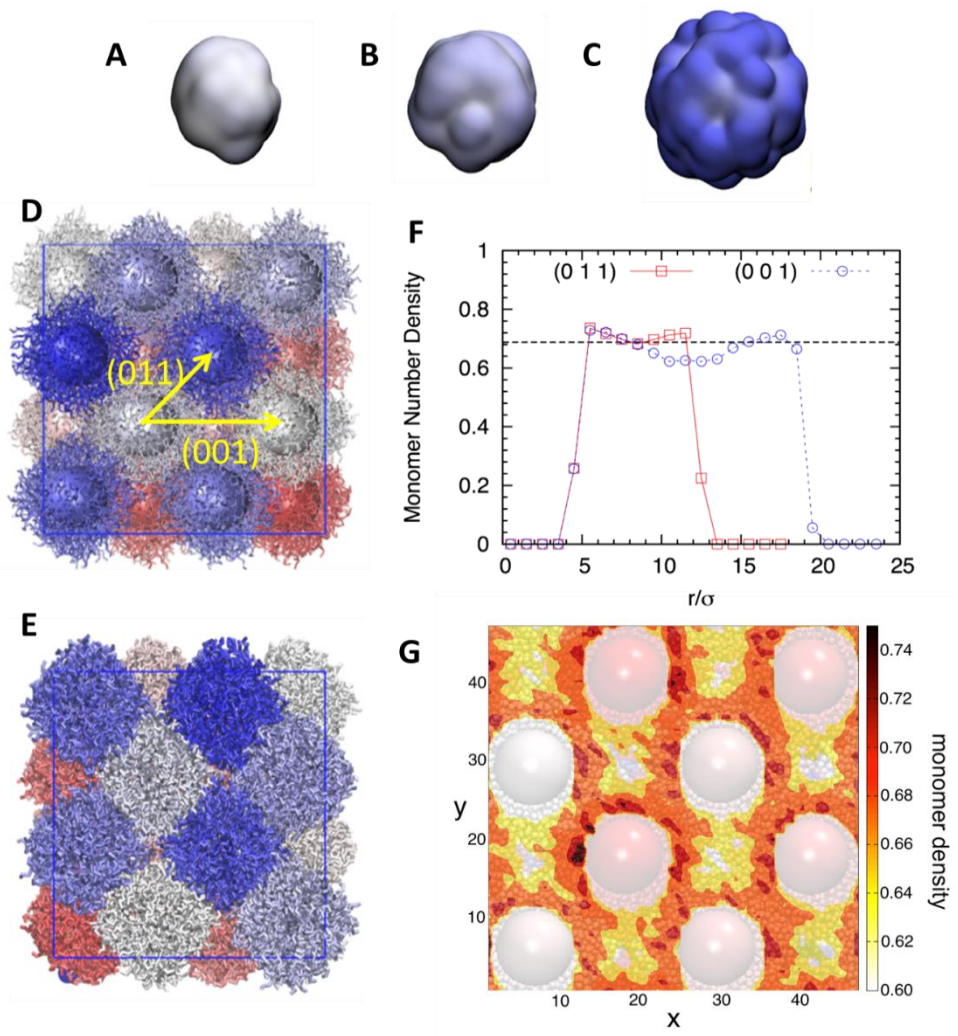

Figure 2.9: Computer simulations of polymer-grafted nanoparticles. (A-C) Coarse-grained computer simulation results of single-grafted nanoparticles for (A) short (N=5), (B) medium (N=10) and (C) long (N=20) chain lengths (30 chains per particle); particle diameter=7, monomer size=1; (D,E) Coarse-grained molecular dynamics simulations of polymer grafted nanoparticle assemblies highlighting the polymer corona distortion from an isotropic spherical shell to allow for filling space. The particle diameter is 10, and the monomer size is 1. 200 chains of 10 monomers are uniformly grafted to each particle, and the particle initial positions are fixed. (D) highlights the nanoparticle core, while (E) highlights the polymer corona. (G) Monomer density histogram corresponding to the corona in (D) and (E), showing the chain density dependence in the (001) and (011) directions. The x-axis is radial distance away from the particle core (r), normalized to the size of the particle (σ). (G) "Heatmap" of monomer density in nanoparticles (diameter=10) grafted with polymer chains (monomer diameter=1, chain length=10, 200 chains per particle, averaged over 500 simulations). The interstitial regions in the structure have moderately reduced polymer density relative to the rest of the corona structure.

to that of the simulated neat polymer melt. However, the monomer density is reduced along the [001] direction near the lattice interstices (at distances of $10<\sigma<15$). This is consistent with the polymer chains stretching in this direction. This corona distortion, which results from a compromise between nanoparticle ordering and chain packing, increases the free volume, as shown in the corresponding "heatmap" of monomer density generated as an average of 500 independent simulation snapshots, Figure 2.9G. Since density has been shown to be related to free volume[33], these regions of decreased density should lead to free volume increases. This is corroborated by the experimentally measured densities of the composites, Figure 2.5D. Figure 2.10 shows the measured unoccupied volume as a function of simulation temperature for a pure polymer and a polymer-grafted nanoparticle system. In both cases, the polymer chains are composed 10 monomers of size σ; the grafted nanoparticle system is composed of 100 chains grafted onto a nanoparticle of diameter 10σ. The unoccupied volume is calculated by collecting all of the volume

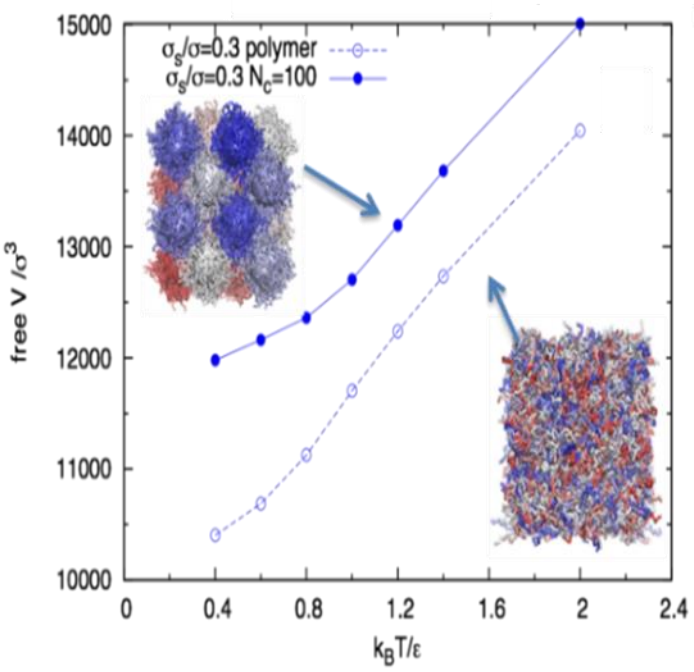

Figure 2.10: Unoccupied volumes in neat and grafted nanoparticle composite materials

of the simulation box that is not taken up by either the nanoparticle or the polymer chains. From here it is obvious that the grafted nanoparticle arrays indeed possess increased unoccupied volume when compared to a pure polymer of identical M_n. However, we do not make the claim that unoccupied volume and free volume are equivalent or related to each other.

The combination of the PALS free volume experiments, multi-nanoparticle simulations, and experimental and computational density calculations argue that the free volume in grafted nanoparticles can be suitably controlled to enhance material permeability while also increasing the chemical, mechanical and temporal stability of the polymer brush. Based on insights of these computer simulations, we explore further the structure of these materials and how structure may influence transport properties in Chapter 3.

Chapter 3

Determining the Structure of Polymer-Grafted Nanoparticle Membranes

In this chapter, we explore the structure of matrix-free grafted nanoparticles from the nanometer to micrometer length scales. In the first part of this study, we probe the particle distribution in the dry state. Using a combination of transmission electron microscopy (TEM) and small angle X-ray scattering (SAXS), we find that the nanoparticle cores are uniformly well dispersed and the distance between nanoparticle cores increases with increasing M_n. While we do not observe long range crystalline order directly from microscopy, we cannot rule out any short range anisotropy from SAXS looking in Fourier space alone. Instead, we adapt a pair distribution function analysis (PDF) commonly used in atomic systems to investigate the structure in real space. For these systems, PDF analysis confirms these materials are isotropic for a wide range of M_n for two different graft densities. Therefore, the anomalous transport behavior cannot be attributed to the dry state structure alone.

Therefore, using a custom vapor handling system which allows for precise solvent environment, in the second part of this chapter we investigate the effect of ethyl acetate (EtAC) solvent on the swollen state microstructure of poly(methyl acrylate) grafted silica nanoparticles (PMA-g-SiO_2) films at equilibrium. We first investigate the effect of solvent concentration on the overall nanoparticle organization using *in-situ* SAXS. However, subtle differences in system contrast will significantly affect the overall scattering intensity function, and potentially allow us

to identify distinct morphologies of the grafted chains and/or solvent distribution within the film. Therefore, we also conduct SANS experiments using a custom sample holder, and systematically vary the contrast (via precise mixtures of protonated and deuterated solvent) to evaluate whether any heterogeneity in the solvent distribution within a thin film of matrix-free GNPs exists as it swells. Through this approach we find that solvent is present uniformly in the polymer layer at all concentrations that were experimentally accessible. Thus, we believe the main consequence of grafting chains to the nanoparticles is to isotropically increase the molar volume of the polymer phase relative to its neat polymer analog, a finding that is consistent with macroscale dilatometry measurements that are not sensitive to spatial variations in density.

3.1 Materials and Methods

We study matrix-free PMA grafted nanoparticles (core diameter 15 ± 4nm) prepared using methods detailed in sections 2.1.1 and A.1. The antioxidant Irganox 1010 (BASF, Germany) was added to all samples at a concentration of 0.1wt% relative to the polymer mass to prevent degradation during annealing and drying between swelling experiments. Protonated ethyl acetate (≥99.5% purity) was purchased from Sigma Aldrich (St. Louis, MO, U.S.A.) and used as received. Per-deuterated ethyl acetate-d8 (99.5% atom D, 99% CP) was purchased either from Sigma Aldrich or Cambridge Isotopes Labs (Tewksbury, MA, U.S.A) and used as received. Silicon wafers (1in diameter, CZ grown, (100) orientation) were purchased from Wafer World (West Palm Beach, FL, U.S.A.). Muscovite mica sheets were purchased from Electron Microscopy Sciences (Hatfield, PA, U.S.A.) Indium wire for sample cell gaskets and leak prevention was purchased from Sigma Aldrich. Samples used for bulk SAXS and PDF analysis are detailed in Table 3.1. Samples used in TEM and bulk SANS studies are detailed in Table 3.2 . Sample 43-55 was used

for all SAXS and SANS swelling experiments. Details on experimental protocols can be found in Appendix A, sections A.8-A.9.

Table 3.1: Sample information for bulk SAXS and PDF studies

Sample Name	Graft Density σ chains/nm^2	Molecular Weight M_n g/mol	Polydispersity Đ	Weight Fraction Silica (wt%)
47-29	0.47	29,800	1.14	$23.8 \pm 3x10^{-3}$
47-41		41,100	1.16	$19.0 \pm 3x10^{-1}$
47-65		65,200	1.20	$10.7 \pm 8x10^{-2}$
47-79		79,200	1.20	$10.5 \pm 3x10^{-2}$
47-101		100,900	1.28	$7.1 \pm 3x10^{-2}$
47-132		132,500	1.29	$5.2 \pm 3x10^{-4}$
66-31	0.66	31,400	1.13	$20.8 \pm 1x10^{-1}$
66-41		40,600	1.15	$15.0 \pm 9x10^{-2}$
66-62		61,700	1.19	$11.7 \pm 9x10^{-3}$
66-82		82,200	1.18	$8.6 \pm 5x10^{-1}$
66-106		106,300	1.32	$5.0 \pm 2x10^{-2}$
66-129		128,900	1.35	$4.1 \pm 1x10^{-1}$

Table 3.2: Sample information for TEM, and thin film swelling SAXS/SANS

Sample Name	Graft Density σ chains/nm²	Molecular Weight M_n g/mol	Polydispersity Đ	Weight Fraction Silica (wt%)
43-27	0.43	26,900	1.14	$30.2 \pm 1x10^{-3}$
43-38		38,100	1.11	$23.1 \pm 6x10^{-2}$
*43-55		55,300	1.16	$16.8 \pm 2x10^{-3}$
43-62		62,000	1.13	$12.9 \pm 2x10^{-1}$
43-92		92,100	1.13	$9.8 \pm 1x10^{-3}$
43-132		132,100	1.18	$5.9 \pm 1x10^{-2}$

*Sample for thin film swelling in SAXS/SANS only

3.1.1 Bulk Sample Preparation

Bulk samples for dry SAXS measurements were prepared by filtering approximately 10-15ml of solution (depending on initial solution concentration) through a 2um PTFE syringe filter into a 20ml PTFE crucible. The crucibles were covered with a Pyrex dish to slow solvent evaporation, which reduces air bubbles in the samples and allows for facilitated molding. The samples were first dried in a fume hood for 3-5 days at room temperature, and then transferred to a vacuum oven. Samples were annealed for 3 days under vacuum at 80°C followed by 24 hours at 110°C. Samples were molded into 8mm by approximately 1mm disks by loading approximately 60-70mg of dry sample to an 8mm vacuum mold. Vacuum was applied inside the mold by connecting a hose on the chamber to the inlet of an air compressor. The mold was heated to 80°C for 2-3 hours and then allowed to gradually cool to room temperature, still under vacuum conditions. Samples were then removed from the mold and stored in a dry box until measuring to

prevent absorption of water vapor from the atmosphere. Table 1 shows information on samples studied for bulk material characterization.

3.1.2 Thin Film Preparation

SANS samples

Silicon wafer supports were cleaned immediately prior to use in a basic piranha solution followed by UV ozone oven (details of this cleaning procedure are found in section 2.1.1). Stock solution of the grafted nanoparticles (8wt% in THF) was filtered with a 2μm PTFE filter and approximately 0.7-0.8ml solution was dispensed onto the polished side of a silicon wafer, ensuring the entire surface was fully covered. The wafer was then spun at 1000rpm for 60s using a Laurell Technologies (North Whales, PA, U.S.A.) spin coater. The wafers were transferred to a vacuum oven and annealed for 3 days at 80°C and were stored in a dry box prior to use. Film thicknesses were measured on multiple points with an α-SE spectroscopic ellipsometer (J.A. Wollaam, Lincoln NE, U.S.A.).

SAXS samples

Mica disks (9.5mm diameter, ~0.15mm thick) were used for swelling experiments with SAXS. The disks were first cleaned with methanol and then the top layer was carefully peeled off with a clean razor blade to expose a fresh surface. The surface was fully covered with the same stock solution as above and spun and annealed using identical conditions as the silicon wafers described above.

3.2 Transmission Electron Microscopy

In-plane TEM microscopy of the matrix-free grafted nanoparticles of a range of M_n (σ=0.43chains/nm^2) was performed by drop casting from dilute solution onto lacey carbon grids. The micrographs reveal the grafted particles are uniformly well dispersed, and the average inter-particle spacing increases with M_n (Figure 3.1). Although the particles do not appear to exhibit any long range crystalline order, it is difficult to assess whether any short range order may be present in bulk samples, so we turn to transmission small angle scattering in the following sections.

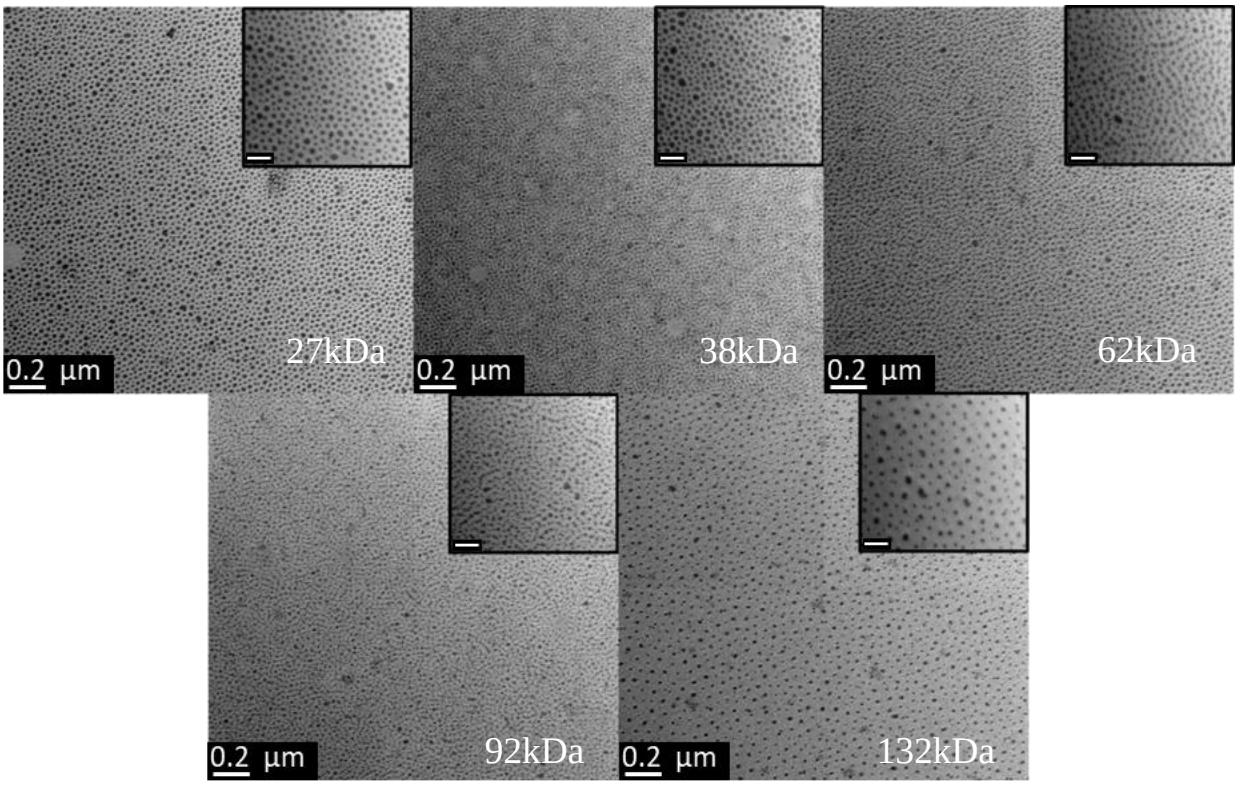

Figure 3.1: Transmission electron microscopy of PMA composites of varying M_n (Σ=0.43chains/nm^2). Scale bars of insets are 100nm

3.3 Bulk SAXS and PDF Analysis

We measure the structure of the matrix-free grafted nanoparticles in bulk using transmission SAXS. Absolute intensities, $I(q)$ as a function of scattering vector, q, are shown in Figure 3.2 for a range of M_n at two grafting densities: σ=0.47chains/nm^2 ("medium") and σ=0.66chains/nm^2 ("high"). Refer to Table 3.1 for sample details.

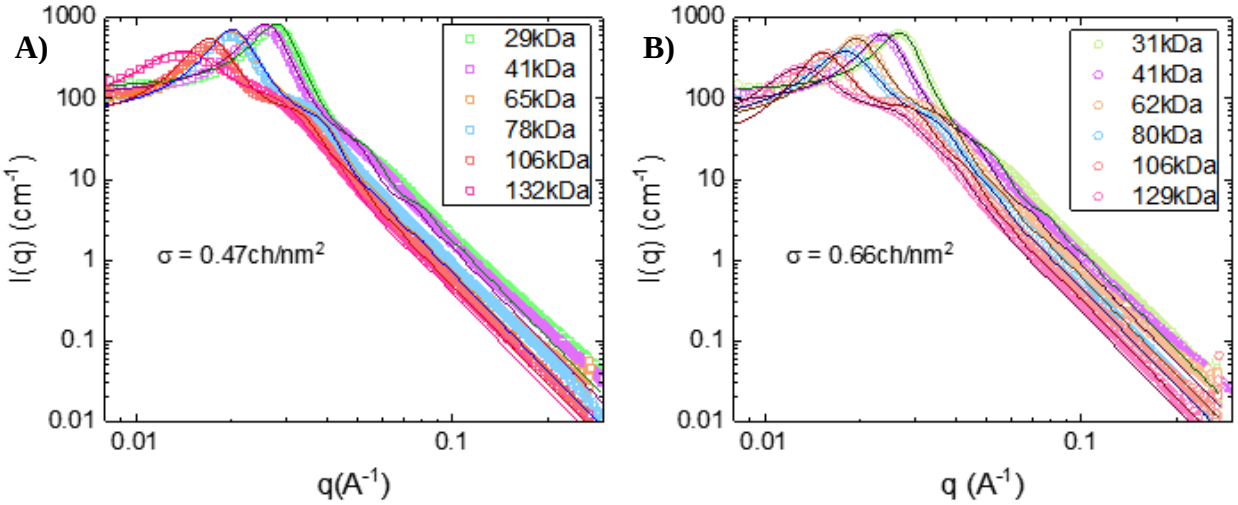

Figure 3.2: Transmission SAXS in bulk PMA grafted nanoparticle composites. Absolute scattering intensity for (A) σ=0.47chains/nm^2 and (B) σ=0.66chains/nm^2. Lines are fits using polydisperse spheres form factor and Percus-Yevick structure factor.

As M_n increases, the location of the structure peaks shifts to lower q, suggesting the inter-particle distance is increasing monotonically with chain length. The data are reasonably fit in Fourier space using a polydisperse spherical form factor and a hard sphere interaction (Percus-Yevick) structure factor. However, Hansen has suggested that the first peak of the inter-particle structure factor exceeds 2.85 in crystalline samples.[78] Our fitted values are well below this value, so we conclude that these systems do not exhibit long-range, crystalline order.

Therefore, we adapt a pair distribution function analysis (PDF) commonly used in atomic systems to investigate the structure in real space to determine whether the grafted particles order (in crystalline lattices or otherwise) on the local scale.[79–81] Using an experimental structure factor, $S(q)$, obtained by diving the scattering intensity, $I(q)$, by the form factor, $P(q)$, of bare silica nanoparticles suspended in dilute solution, a reduced structure factor, $F(q)$, is calculated as:

$$F(q) = q[S(q) - 1] \tag{3.1}$$

Taking a sine Fourier transform of $F(q)$ yields a pair distribution function, $G(r)$. In this case, $G(r)$ refers to the probability of finding nanoparticle core pairs at distance r apart, calculated as:

$$G(r) = \frac{2}{\pi}\int_{q_{min}}^{q_{max}} F(q)\sin(qr)\,dq \tag{3.2}$$

By analyzing the $G(r)$ in real space, we can identify more subtle effects of M_n on the structure of these materials such as the persistence length and directionality of any ordered structures that may exist.

Figure 3.3 shows $S(q)$ and $F(q)$ for various M_n for both medium and high graft density. Refer to Table 3.1 for sample details. Figure 3.4 shows $G(r)$ for medium and high graft density for various M_n. The PDF analysis is very sensitive to slight variations and/or kinks in the data, therefore we use only data collected from one sample to detector distance (SDD) ("SAXS" configuration, see section A.8 for details) due to the error associated with "stitching" data from multiple SDDs. Despite collection times >2hrs, the signal to noise ratio limited the q_{max} between 0.05-0.075A^{-1}. Note that the first small features at small r are not structurally real, but give an indication as to the quality of the data, so we therefore include them.

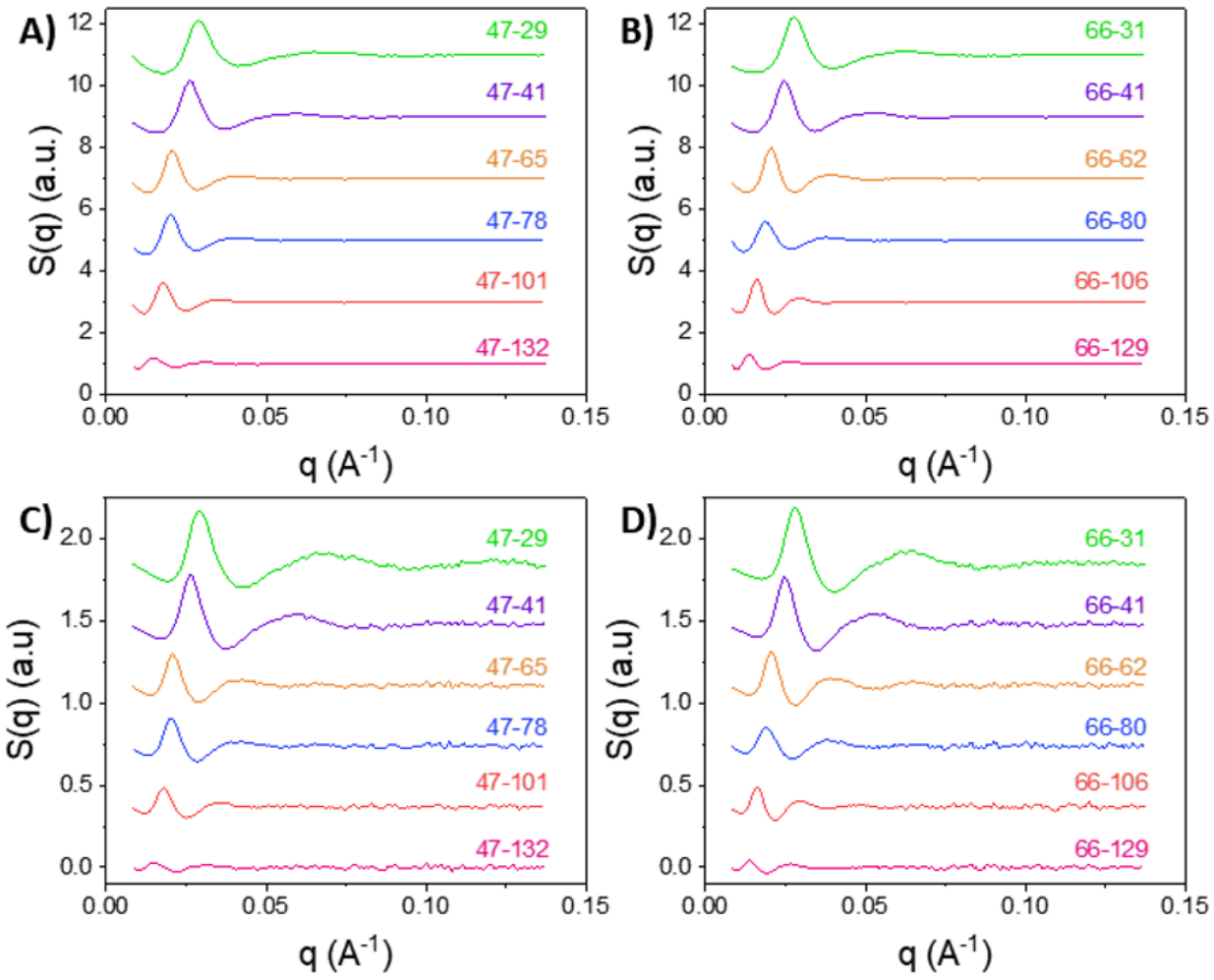

Figure 3.3: Structure factor and reduced structure factor for grafted PMA nanoparticles with graft density σ =0.47chains/nm^2 (A and C) and σ =0.66chains/nm^2 (B and D). Curves are shifted vertically for visual clarity

The $G(r)$ show that as chain length increases, the inter-particle spacing increases, as evidenced from the position of the first peak. Higher-order features are visible for low M_n samples, but the coherence decays rapidly as M_n increases. Additionally, as M_n increases, the peaks broaden, signaling the distribution of shell sizes increases as chain length increases.

The first-nearest neighbor inter-particle spacing is extracted as the first peak position, ${G(R)_1}^*$ (Figure 3.5). The brush height on a single particle, $h = [{G(R)_1}^* - d]/2$, where the bare

core particle diameter, d, is measured as 14nm from fits of a form factor in dilute solution. Regression analysis of $\log(h)$ versus $\log(N)$ (where N is the degree of polymerization defined from the *weight* average molecular weight, M_w) shows the brush is significantly stretched, with a scaling exponent of ~0.7. Based on work by Dukes et al., for the graft densities studied here, the behavior of these particles appears to be within the regime where the brush conformation transitions from that of a concentrated polymer brush regime (CPB) to a semi-dilute polymer brush regime (SDPB).[82] However, as our systems are solvent and matrix free, we postulate that the brush conformation at large r is more "Gaussian-like" (θ-solvent conditions) instead of swollen (good solvent). But, on average the overall brush height still scales as $\sim N^{0.7}$ due to the highly stretched inner core. We detail these scaling arguments later in Chapter 4.

Additionally, fitting the $G(r)$ with a single damped sine wave can determine whether these systems exhibit any local ordered structures or are isotropic in all directions. Any ordered structures, such as crystalline grains, strings, etc. will have a directional anisotropy, and thus

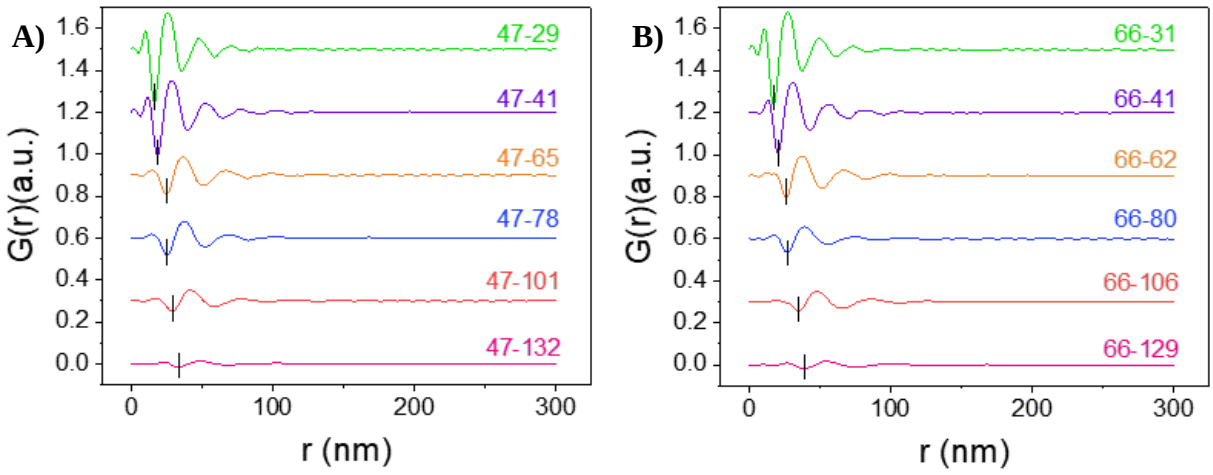

Figure 3.4: Probability distribution function $G(r)$ for grafted PMA nanoparticles with graft density (A) σ=0.47chains/nm^2 and (B) σ=0.66chains/nm^2. Curves are shifted vertically for visual clarity. Black vertical hash marks indicate lower r limit where below this value, data are unphysical yet indicate data quality.

multiple spatial frequencies, therefore $G(r)$ could not be described by a sine wave with a single frequency. The sine wave is described as:

$$G_c(r) = C \sin\left(2\pi \frac{r}{\lambda} + \phi\right) \exp\left(-\frac{{q_{damp}}^2 r^2}{2}\right) \tag{3.4}$$

where C is the scaling constant, λ is the wave length, ϕ is the phase shift and q_{damp} is the damping factor. Figure 3.6 shows damped sine wave fits to the $G(r)$ for various $M_n$for σ=0.47chains/nm^2 and σ=0.66chains/nm^2, respectively. At low M_n, the $G(r)$ is well described by the damped sine wave fitting for both graft densities. However, around 78-80kDa, the damped sine wave begins to deviate from the data after the second peak, with the fit underestimating the peak positions of the

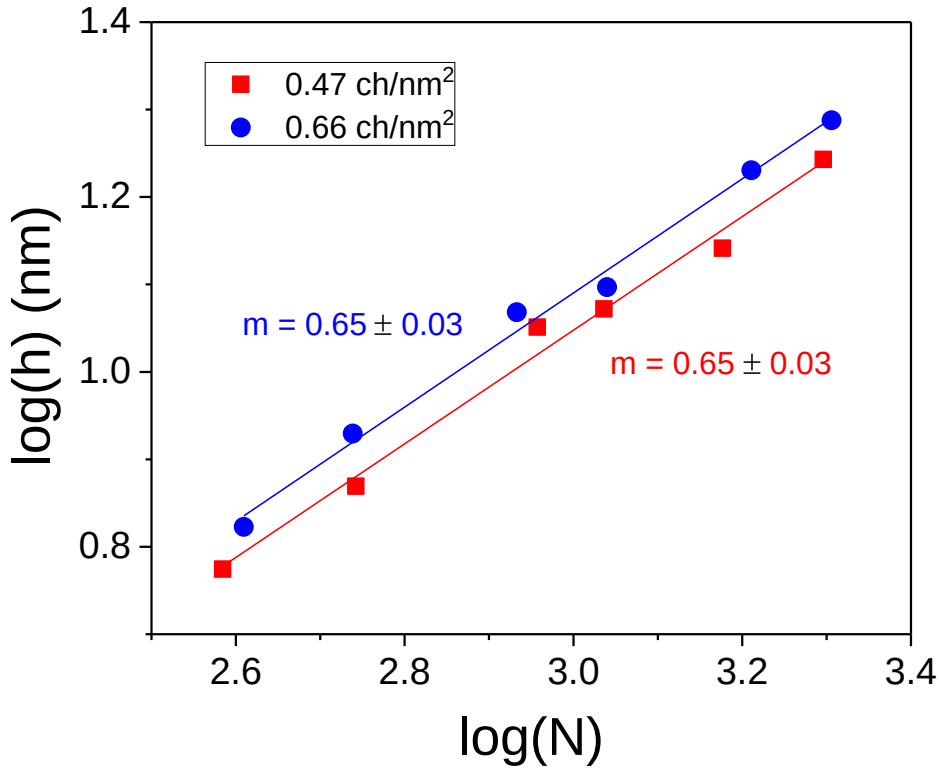

Figure 3.5: Brush height of grafted nanoparticles versus degree of polymerization

higher-order features. This discrepancy increases as M_n increases further. However, because the first peak is still captured for all samples by the damped sine wave fit, we can conclude these materials are completely isotropic regardless of graft density or chain length.

As a result of densely grafting from a curved surface, the brush conformation contains a relatively rigid, stretched inner regime and a more Gaussian-like outer regime. The rigid shell results in the core particle distribution remaining more or less fixed. Thus, particles with small M_n are uniformly spaced, but their placement is random and the $G(r)$ is well described by a damped sine wave even for the second and third nearest neighbor shells. As M_n increases beyond the critical crossover, the length of the Gaussian ends increases, while at the same time, the overall polydispersity of the chains increases. Chain segments in this regime are more flexible, therefore while the first nearest neighbor shell has an average distance that is captured by the damped sine wave, fluctuations in the higher order shells might arise from this softer interaction parameter,

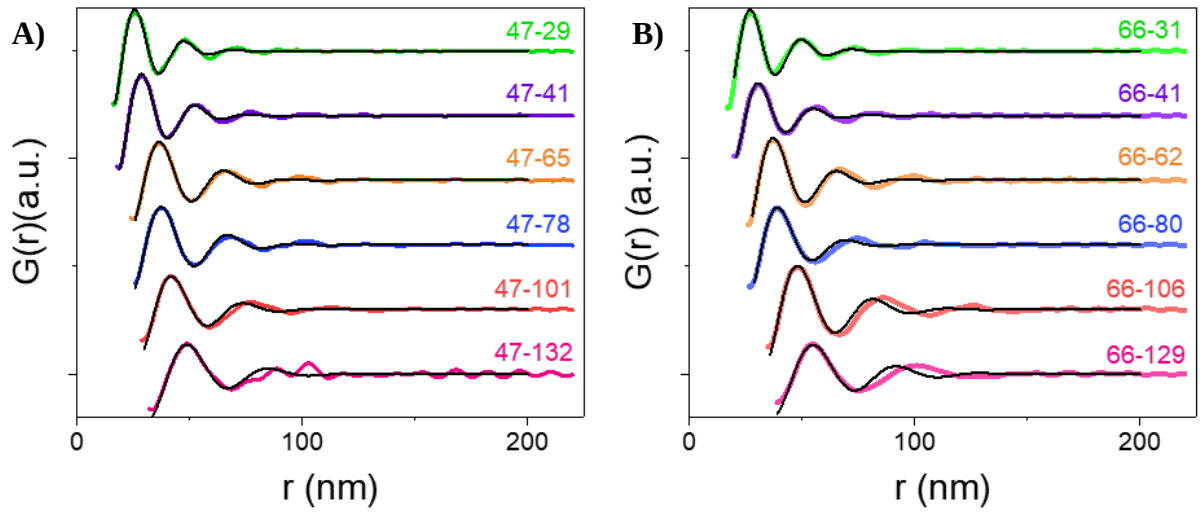

Figure 3.6: Damped sine wave fits of $G(r)$ for grafted PMA nanoparticles with graft density (A) σ=0.47chains/nm^2 and (B) σ=0.66chains/nm^2. Curves are shifted vertically for visual clarity. Note the amplitudes are rescaled so that each curve is of comparable scale.

which explains why the damped sine wave is less accurate at predicting the second and third nearest neighbor shells. This flexibility continues to increase as M_n increases.

PDF analysis shows that for the range of M_n for the two graft densities studied, these systems are uniformly dispersed, yet completely isotropic, even on local length scales. The average spacing between particles extracted from a $G(r)$ matches that of a Percus-Yevick structure factor fit, showing that this model is adequate for modeling our system.

3.4 Structure of Polymer-Grafted Nanoparticle Membranes with Imbibed Solvent

Wafers of PMA-g-SiO_2 (sample 43-55) were prepared using the above method. For SANS measurements, ten wafers were used in the sample cell. The thickness of each film was measured using ellipsometry with an average film thickness of 766 ±40 nm; for SANS absolute intensity conversion, the total dry sample thickness used was 7.66 x 10^{-3} mm. The same sample wafers were used for all measurements at both SANS beamlines. For consistency, the dry films were measured on both beamlines and swollen states are compared to the dry film data from the respective beamlines they were measured on. Additionally, relative differences in the background for each respective beamline are responsible for the discrepancies in the high-q intensities.

Figure 3.7 shows the evolution of the 1D scattering intensity as a function of equilibrium solvent concentration in SAXS using purely hydrogenated solvent ("EtAC-h_8"). As the concentration of solvent absorbed into the film increases, the peaks shift systematically to lower q, indicating that the inter-particle distance of the silica cores increases. As a first-pass approximation, if the system is incompressible, the pressure exerted on the cores by the addition of the solvent is uniform on average in all directions, regardless of where the solvent is located

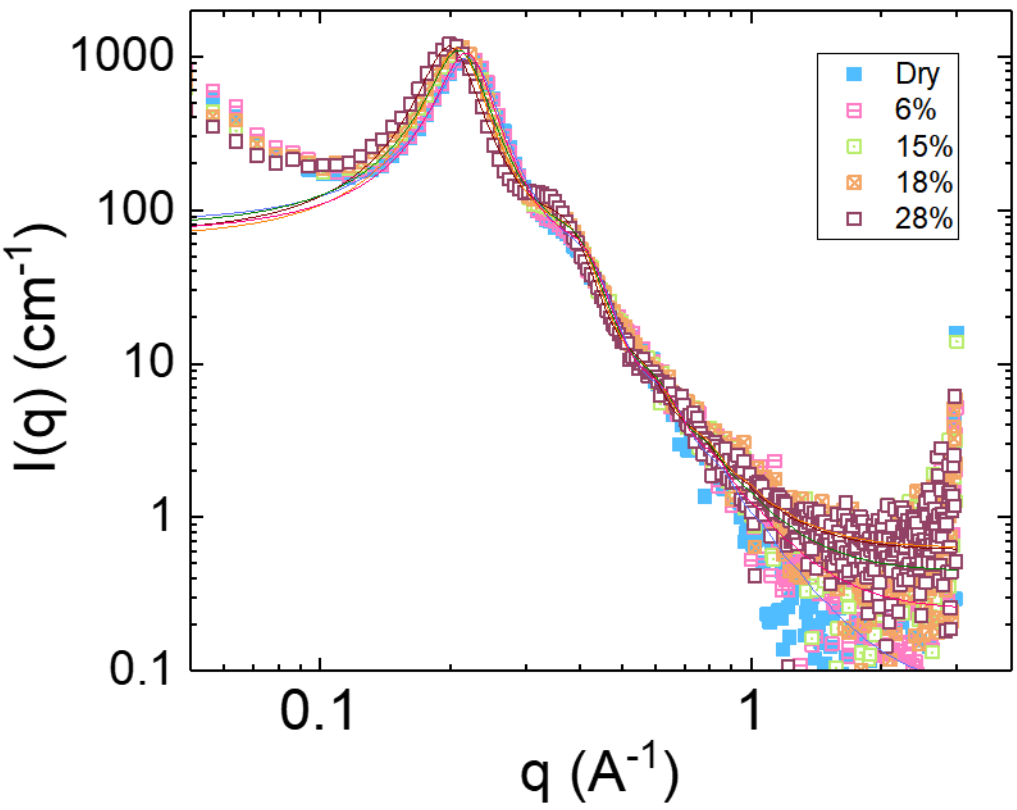

Figure 3.7: SAXS intensity upon solvent swelling for various solvent concentrations [$\phi_s(V)$]

with respect to the polymer chains (for example, homogenously distributed between the entire brush or segregated to the outside of the grafted corona). Assuming the structure factor is dominated by the silica cores, we fit the peak position using a hard-sphere interaction (Percus-Yevick) structure factor. The change in inter-particle spacing relative to that of the dry film can then be directly calculated from the difference in the hard sphere interaction radius between the wet $R_{HS,w}$ and dry $R_{HS,d}$ states. The concentration of solvent in the film based on a volume argument, $\phi_s(V)$ can then be calculated as:

$$\phi_s(V) = 1 - \left(\frac{R_{HS,w}}{R_{HS,d}}\right)^{-3} \tag{3.1}$$

However, to fully fit the intensity spectra and determine where the solvent molecules are

located with respect to the polymer chains, we must first determine the appropriate form factor model of the swollen grafted particle systems. In other words, SAXS cannot tell us whether the solvent is swelling the grafted brushes or not since there is no specific contrast with the polymer. Therefore, we turn to solvent labeling and neutron scattering. Figure 3.8 shows simulations of three different possible morphologies with varied neutron solvent SLD values. Case 1 depicts spherical particles dispersed in a homogenous fluid of average scattering length density, where the solvent fully wets the polymer chains. Case 2 shows spherical particles grafted with Gaussian polymer chains where the solvent can penetrate to the core *in-between* the chains, but is excluded from the polymer coil. Finally, Case 3 depicts a spherical core-shell model where the solvent does not penetrate the polymer brush. In all cases, a polydispersity of approximately 30% in the silica cores is included. Additionally, in order to decouple effects of SLD and changes to inter-particle spacing, we fix the structure factor parameters. These simulations show significant differences in structure can be readily identified by the effect of the solvent SLD: if the swelling is homogenous, the intensity scales linearly with the contrast variation as seen for Case 1. Conversely, if the brush contributes to the scattering, the intensity systematically increases, as seen for Case 2 and Case 3.

To identify the spatial distribution of solvent in the swollen film, we measure various solvent concentrations in SANS with EtAC-h_8, in addition to purely deuterated solvent ("EtAC-d_8") and a 46vol% H:54vol% D solvent mixture ("EtAC-mix"). The ratio of the H:D mixture was chosen to have the same scattering length density of the cores (based on a silica density of 2.0696 g/cm^3 previously measured using gas pycnometry[4]) to enhance the grafted chains signal as much as possible. However, covalently grafting the polymer chains to the nanoparticles renders this system as a pseudo-two-phase system: the grafted particles and solvent. Therefore, the complete matching of the silica core cannot be achieved. Some contrast between the silica and the

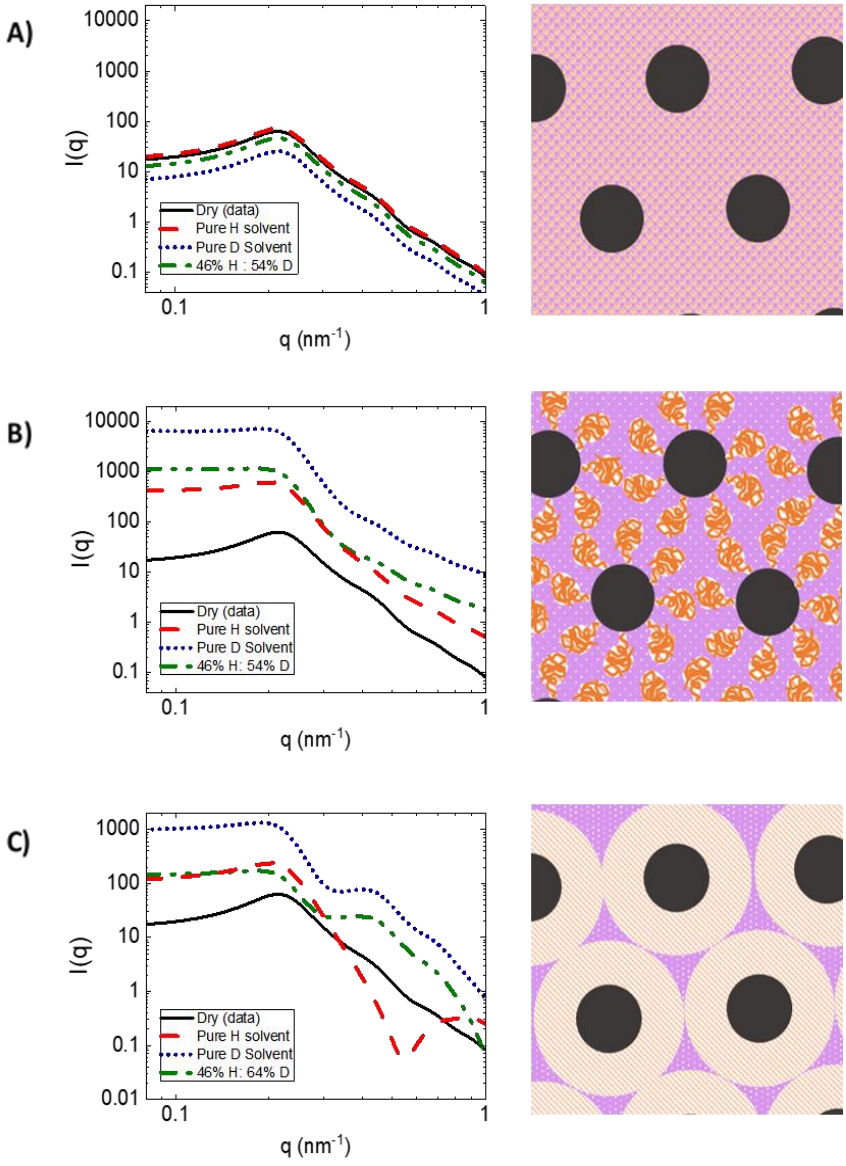

Figure 3.8: Simulations of various particle morphologies with different solvent SLD. (A) Case 1: hard spheres in fluid; (B) Case 2: Hard spheres grafted with Gaussian polymer coils in a solvent; (C) Case 3: Spherical core-shell particles in a solvent

surrounding environment will always exist, no matter the solvent SLD. Figure 3.9 shows the evolution of the 1D intensity upon swelling at equilibrium for various solvent concentrations and contrasts in SANS. At the lowest concentration of solvent for SANS, there is no obvious change to the peak position; this condition appears to be the limit where the film can absorb solvent but

not swell. As solvent concentration increases, the distance between the silica cores increases, as seen by shifting of the peaks to lower q. For all concentrations in SANS, with purely protonated solvent, EtAC-h_8, the intensity increases with increasing solvent concentration. On the other hand, when protonated solvent is switched for the mix solvent and deuterated EtAC-d_8, the intensity systematically drops.

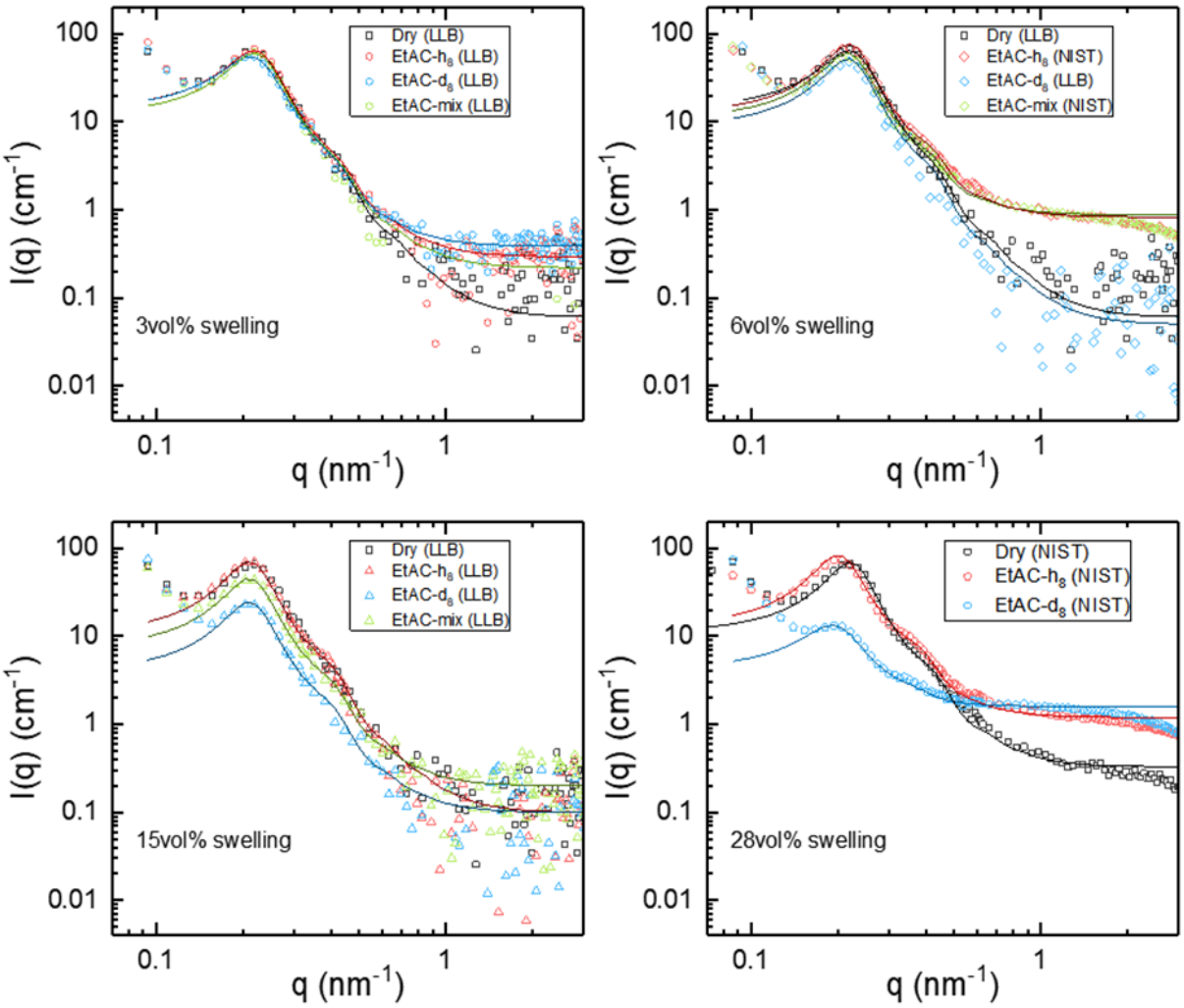

Figure 3.9: SANS intensity upon solvent swelling for various solvent concentrations $\phi_s(V)$.(A) 3vol%; (B) 6vol%; (C) 15vol%; (D) 28vol% with EtAC-h_8 (red), EtAC-d_8, and EtAC-mix (green). Black curves correspond to dry films (no solvent). Symbols correspond to data and lines correspond to fits. "NIST" indicates data were run on NG-7 beamline at the NCNR and "LLB" indicates data were collected on the PA-20 beamline at the LLB.

Fitting parameters using the above method can be found in Table 3.3 and Table 3.4 for SAXS and SANS experiments, respectively. To confirm films are at equilibrium after 30min, fitting parameters as a function of vapor exposure time in SAXS are found in Table A- 1.

Table 3.3: Fitting parameters of swollen films in SAXS for various solvent concentration conditions. $\phi_{HS,w}$ refers to the vol. fraction of hard sphere interactions from a Percus-Yevick S(Q).

$\phi_s(V)$	Solvent Type	$\phi_{p,w}$*	σ	Core Radius (nm)	η X 10^{-10} (cm^{-1})	$R_{HS,w}$ * (nm)	ϕ_{HS}*	$\phi_s(\eta)$
Dry	N/A	0.102*	0.28	7.01	6.641	14.6*	0.41*	N/A
Re-Dry	N/A	0.103*	0.28	7.01	6.641	14.6*	0.40*	N/A
6%	h_8	0.096	0.28	7.01	6.814	14.9	0.33	6.2
15%	h_8	0.088	0.28	7.01	7.074	15.4	0.40	15.6
15%	d_8	0.089	0.28	7.01	7.103	15.4	0.40	16.3
20%	h_8	0.082	0.28	7.01	7.180	15.7	0.41	19.4
28%	h_8	0.074	0.28	7.01	7.448	16.3	0.40	29.0

** refers to dry state ($\phi_{p,d}$, $R_{HS,d}$, $\phi_{HS,d}$)*

The scattering intensity at all solvent concentrations most closely resembles Case 1 of the simulations. Therefore, we first attempt to fit the swelling intensity spectra with a hard-sphere model. However, to properly fit the data and account for the contrast between particle, polymer, and solvent in the system, it is critical to first convert the data to absolute intensity by accounting for differences in film thickness upon swelling. Based on changes in inter-particle spacing obtained from hard sphere structure factor fits, the thickness of the swollen film is calculated as:

$$l_w = l_d \left(\frac{R_{HS,w}}{R_{HS,d}}\right)^3 \tag{3.2}$$

where the subscripts d and w refer to the "dry" and "wet" states, respectively. The absolute intensity is then calculated by multiplying I(q) by a correction factor of l_w/l_d. Additionally, the

new effective volume fraction of particles in the wet state, $\phi_{p,w}$ is therefore calculated as:

$$\phi_{p,w} = \phi_{p,d}\left(\frac{R_{HS,w}}{R_{HS,d}}\right)^{-3} \tag{3.3}$$

Table 3.4: Fitting parameters of swollen films in SANS for various solvent concentration conditions and solvent contrast ("solvent type"). $\phi_{HS,w}$ refers to the volume fraction of hard sphere interactions from a Percus-Yevick structure factor.

$\phi_s(V)$	Solvent Type	Beam Line	$\phi_{p,w}$*	σ	Core Radius (nm)	η X 10^{-10} (cm^{-1})	$R_{HS,w}$* (nm)	$\phi_{HS,w}$*	$\phi_s(\eta)$
0% (dry)	N/A	LLB	0.102*	0.28	7.17	1.921	13.80*	0.33*	N/A
	N/A	NIST	0.102*	0.28	6.99	1.921	13.74*	0.32*	N/A
3%	h_8	LLB	0.102	0.28	7.17	1.955	13.73	0.33	3.8
	d_8	LLB	0.102	0.28	7.17	1.775	13.77	0.30	3.5
	mix	LLB	0.101	0.28	7.17	1.865	13.75	0.32	3.1
6%	h_8	NIST	0.095	0.28	6.99	1.987	14.15	0.34	7.5
	d_8	LLB	0.094	0.28	7.17	1.628	14.15	0.33	6.9
	mix	NIST	0.095	0.28	6.99	1.815	14.07	0.33	5.6
15%	h_8	LLB	0.086	0.28	7.17	2.063	14.45	0.32	16.6
	d_8	LLB	0.086	0.28	7.17	1.220	14.41	0.32	16.4
	mix	LLB	0.088	0.28	7.17	1.653	14.40	0.33	14.0
28%	h_8	NIST	0.079	0.28	6.99	2.154	15.40	0.33	27.0
	d_8	NIST	0.078	0.28	6.99	0.870	15.15	0.28	24.5

** refers to dry state ($\phi_{p,d}$, $R_{HS,d}$, $\phi_{HS,d}$)*

Combined with the hard sphere Percus-Yevick structure factor model, the 1D intensities, $I(Q)$, are well fit using a spherical form factor (with a constant background). After accounting for minor differences in fitting parameters due to slight variations in resolution of each beamline, the absolute value of the difference between the dry and wet inter-particle spacing is the same for a given concentration on both beamlines. After adjusting for absolute intensity using the first-pass

approximation for l_w and $\phi_{p,w}$ upon swelling detailed above, the contrast parameter of the form factor, η, is fit to the adjusted intensity with $\phi_{p,w}$ fixed.

Alternatively, we can also compute the volume fraction of solvent independently from η:

$$\phi_s(\eta) = \frac{S_p - \eta - S_{poly}}{S_s - S_{poly}} \tag{3.4}$$

where S is the scattering length density and the subscripts p , s, and $poly$ refers to the silica particles, solvent, and polymer brush, respectively. If values of the volume of solvent in the film obtained from both equations 1 and 4 are comparable, this method provides a self-consistent check on the assumption that the film swells isotropically and the solvent wets the polymer brush homogeneously. Moreover, the change in inter-particle spacing is also found to be the same for all solvent SLD values at a given concentration, indicating no preference by the film for H or D solvent (Figure 3.10).

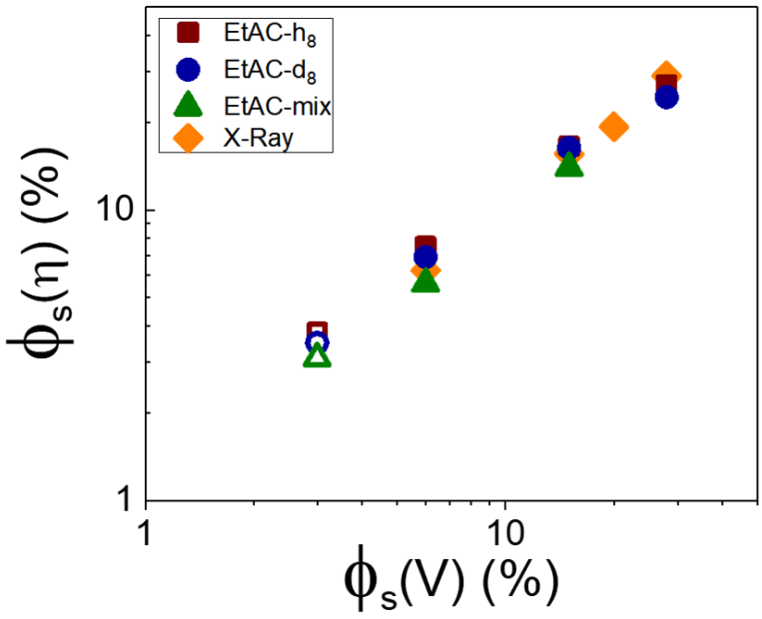

Figure 3.10: Solvent concentration correlation as calculated from fit contrast using a hard sphere form factor model [$\phi_s(\eta)$] versus concentration calculated based on isotropic volumetric changes calculated from changes in structure factor interparticle spacing [$\phi_s(V)$]. Open symbols are for the case where solvent concentration was not high enough to disturb core particle spacing, thus the concentration from contrast fits are plotted against an average value.

Finally, we verify the solvent concentration in the films agree with previous data and that the custom flow cell operates as expected. Figure 3.11 compares the solubility of ethyl acetate in PMA GNP films as a function of reduced pressure (partial pressure of ethyl acetate normalized to the saturated vapor pressure at 20°C). Data are compared to solubility of neat PMA films as reported by Fujita et al.[83] In order to make a direct comparison to the neat PMA performance, grafted film solubility is normalized by a correction factor, S_ϕ / S_b, which is the ratio of solubility in the polymer phase of the grafted system to that of the pure neat melt as measured by QCM.[4] We find excellent agreement between the solvent content measured by SANS to other direct gravimetric methods, further validating our results.

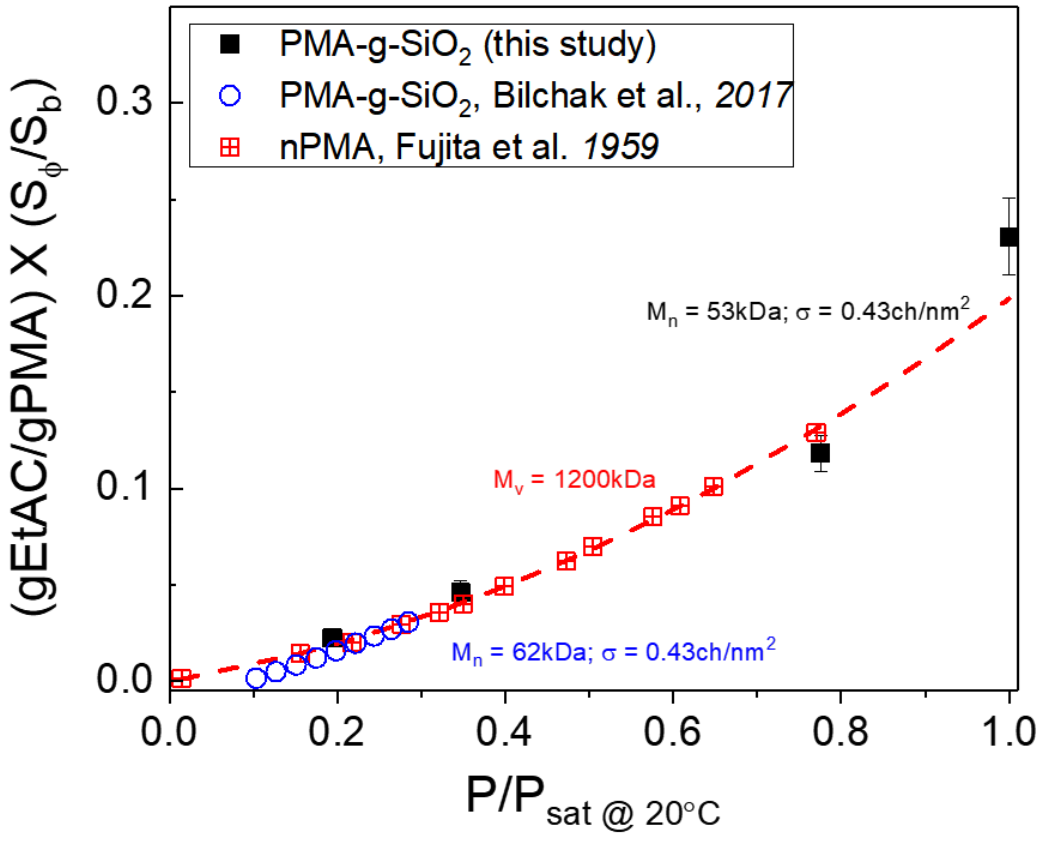

Figure 3.11: Solubility of ethyl acetate as measured by SANS as a function of vapor activity.

Chapter 4

Solid to Liquid Transition of Matrix-Free Polymer Grafted Nanoparticles

Here we study the effects of brush height and graft density on the rheological response in both the linear and nonlinear viscoelastic regime to elucidate how the individual particle structure influences the mechanical response of matrix-free polymer grafted nanoparticles (GNPs). In turn, we examine how the dynamics may provide deeper insight into the mechanism of diffusion and molecular transport in these materials. Using different rheological techniques such as small amplitude oscillatory shear (SAOS) over a range of temperatures, in addition to creep tests, we obtain master curves covering nearly 16 decades in frequency. A rich and unexpected dynamic emerges from the linear response, suggesting these materials exhibit two main relaxation modes: polymeric and colloidal. Whereas the former is attributed to the fast dynamics, reminiscent of the entangled networks formed by the equivalent neat polymers, the latter is encountered at long deformation times, where a colloidal plateau becomes more prominent as chain length decreases (chain lengths $< 10M_e$, where M_e is the entanglement weight of neat PMA (~8800 g/mol[84]).

We propose a hierarchical relaxation mechanism: first the polymeric arm retraction dynamic, similar to that found in star polymer melts[64], and then (where applicable), the colloidal "cage-hopping", defined as the time needed for a single grafted particle unit to exchange position with the next nearest neighbor, analogous to glassy spherical colloids.[85] The polymeric response can be fit with a Branch-on-Branch (BoB) model developed for stars and, when applicable, this can be combined with a mode coupling theory (MCT) to fit the colloidal response. We postulate

that the brush conformation imposed by grafting from a highly curved surface renders these particles as soft, but relatively incompressible spheres with a strongly stretched, rigid inner brush and an outer, Gaussian regime. The radius of the effective rigid sphere is therefore defined as the radius of the silica core plus the thickness of the stretched inner brush.

For samples with low M_n, the total volume fraction of the rigid spheres is high, and the system is tightly packed. In this regime, following the arm retraction mechanism, a colloidal relaxation process dominates the relaxation mechanism, as evidenced from a low frequency plateau which spans several decades. As M_n increases and the volume fraction of rigid spheres decreases to just below that of close-packed spheres, this colloidal process is still present, but the modulus and frequency range are significantly reduced. The behavior of intermediate M_n systems, therefore, is in transition from a colloid-dominated to that of a polymer-dominated system. Finally, for large M_n, the total volume fraction of the rigid spheres is further reduced, and the Gaussian-like regime controls the relaxation dynamics. Samples with high M_n, therefore behave similarly to star polymer melts, and the colloidal process disappears. Interestingly, this solid-to-liquid transition occurs at the chain length where a peak in the permeability occurs, suggesting that the complex mechanical response may be linked to the remarkable transport properties of these materials. However, why long-time response is related to transport mechanisms which occur on the order of ~1s remains unclear. Nevertheless, the significantly longer relaxation times of the GNPs compared to the neat polymer analogs may be related the demonstrably better aging properties of these systems.

Finally, we also study the nonlinear start-up shear response of these materials, which show that for systems with weak to no colloidal behavior, the modulus is significantly increased compared to the corresponding neat melts. On the other hand, where the colloidal mode dominates

the relaxation mechanism (small M_n) experience brittle fracture at strain rates smaller than experimentally accessible. These results indicate in addition to their enhanced transport properties, GNPs with specific brush dimensions may provide mechanical reinforcement, which could prove potentially beneficial to a multitude of applications, including gas separation membranes.

4.1 Materials and Methods

We used 14nm diameter spherical silica nanoparticles from Nissan Chemical (MEK-ST). Polymethylacrylate (PMA) grafted nanoparticles (PMA-g-SiO2) of two grafting densities, σ, and various M_n (Table 4.1) suspended in THF were synthesized using previously documented methods[4]. The antioxidant Irganox 1010 (BASF, Germany) was added to all samples at a concentration of 0.1wt% relative to the polymer mass to prevent degradation during annealing. Samples were prepared by solvent casting in PTFE dishes and allowed to dry at ambient conditions for 2 days, followed by annealing in a vacuum oven at 80C for three days. Afterwards, all samples were stored in a dry box. Silica concentration was determined using thermal gravimetric analysis (TGA) (Discovery TGA, TA Instruments, New Castle DE, USA) by ramping the temperature to 700°C at 10°/min in oxygen.

To mold the samples for SAOS and creep testing, approximately ~65-75mg of material was loaded into an 8mm diameter stainless steel vacuum mold to yield disks of approximately 800-1000μm in thickness. Vacuum was applied inside the mold by connecting a hose on the chamber to the inlet of an air compressor. The mold was heated to 80°C for 2-3 hours and then allowed to gradually cool to room temperature, still under vacuum conditions. For creep measurements, the 8mm disks were trimmed of excess material and used as-is. For SAOS

experiments well above T_g, the 8mm geometry was used. Near T_g (~35-20°C), samples were punched into 4mm disks and a 4mm parallel plate geometry was used to minimize instrument compliance. Samples for non-linear viscoelastic (NLVE) experiments were also molded using the 8mm vacuum mold, however only 20-30mg of material was used, resulting in disks of approximately 400μm in thickness. Between SAOS and creep testing, or creep tests at different stresses, or repeated NLVE testing after sample failure/fracture, disks were remolded to "rejuvenate" the sample. We verify subsequent remolding does not damage samples by obtaining identical responses in SAOS and/or creep compared to fresh material.

Table 4.1: Sample specifications for rheological studies

Sample Name	Graft Density σ chains/nm²	Molecular Weight M_n g/mol	Polydispersity Đ	Weight Fraction Silica (wt%)
47-29	0.47	29,800	1.14	$23.8 \pm 3\times10^{-3}$
47-41		41,100	1.16	$19.0 \pm 3\times10^{-1}$
47-65		65,200	1.20	$10.7 \pm 8\times10^{-2}$
47-79		79,200	1.20	$10.5 \pm 3\times10^{-2}$
47-101		100,900	1.28	$7.1 \pm 3\times10^{-2}$
47-132		132,500	1.29	$5.2 \pm 3\times10^{-4}$
66-31	0.66	31,400	1.13	$20.8 \pm 1\times10^{-1}$
66-41		40,600	1.15	$15.0 \pm 9\times10^{-2}$
66-62		61,700	1.19	$11.7 \pm 9\times10^{-3}$
66-82		82,200	1.18	$8.6 \pm 5\times10^{-1}$
66-106		106,300	1.32	$5.0 \pm 2\times10^{-2}$
66-129		128,900	1.35	$4.1 \pm 1\times10^{-1}$
N-23	Neat	23,100	1.09	N/A
N-44		43,800	1.13	
N-63		62,800	1.17	
N-95		95,700	1.19	
N-125		125,000	1.23	

4.1.1 Small-Amplitude Oscillatory Shear

SAOS experiments were conducted on a DHR-3 stress-controlled rheometer (TA Instruments, USA) using either 8 or 4mm parallel plate geometry. Frequency sweeps were conducted from 100 – 0.1 rad/s at 5°C intervals from 80°C to 30°C and at 2-3°C intervals between 27°C to 20°C. Samples were allowed to equilibrate for at least 10-15 minutes at each temperature before measuring. Although samples contain an antioxidant and are always far below the measured degradation temperature of approximately 350°C as obtained from TGA analysis (Figure 2.5A), temperature control in the DHR-3 is maintained using air in a convection oven. Therefore, we limit exposure times above 60°C to less than 3 hours total to prevent thermal oxidation. Strain amplitude sweeps were conducted at 100rad/s at each temperature, and a strain amplitude was chosen to be within the linear response regime for each frequency sweep. Time-temperature superposition (TTS) with a reference temperature of 60°C was used by shifting data horizontally to generate master curves over a large frequency range. It is not obvious that TTS will be applicable to the grafted particle systems *a priori*, so we verify in Figure 4.1 that the phase shift, δ, as a function of complex modulus, G^* (also known as a van Gurp-Palmen[86] plot) is a continuous spectrum, even for the case of low M_n/high particle loading (sample 47-29). In principle, we can also shift the data vertically, but we find that horizontal shifts are sufficient and reduce uncertainty imposed by the origin of the vertical shifts.[87]

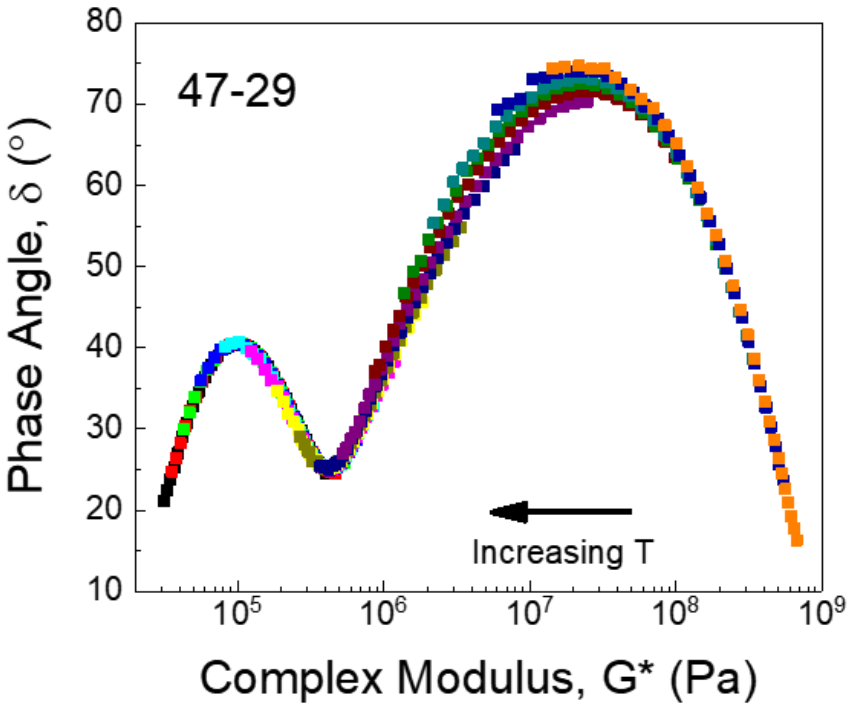

Figure 4.1: van Gurp-Palmen plot for GNP sample with M_n=29kg/mol and σ=0.47chains/nm^2. Phase angle, δ as a function of complex modulus, G^* at various temperatures (different colors). Measured frequency range for each temperature measurement 100-0.1 rad/s.

4.1.2 Creep

Creep experiments were conducted on an MCR-702 stress-controlled rheometer (Anton Paar, Austria). Samples were equilibrated for 20min at 80°C and temperature control was ensured by a control system which has intermediate characteristics between a Peltier cell and a convection oven with nitrogen gas continuously fluxing inside the chamber. Prior to creep testing, a frequency sweep was conducted to ensure the response was the same on different instruments and geometries. Creep experiments were conducted at constant stress for at least 10^5s and up to 10^6s. Measurements were conducted at three different stresses between 50Pa and 100Pa to ensure a linear viscoelastic

response. Creep compliance was converted to dynamic moduli using a nonlinear regularization method.[88] Data were then shifted to a reference temperature of 60°C using shift factors from the SAOS experiments. After the creep experiment, a dynamic frequency sweep test was performed to check the health of the sample due to potential degradation issues after a prolonged exposure to elevated temperature.

4.1.3 Non-Linear Start-Up Shear

NLVE experiments were conducted on an Ares strain-controlled rheometer (TA Instruments) using a cone partition plate[89–93] (CPP) geometry with a 6mm inner plate and an 8mm outer stationary plate to delay complications of edge fracture. Temperature control was achieved using a convection oven with nitrogen gas continuously fluxing inside the chamber. The gap was zeroed after thermal equilibration at 80°C. The samples were loaded with a final measuring gap of 50μm and the normal stress was allowed to fully relax before measuring. A frequency sweep was conducted before start-up of steady shear to ensure identical sample response on the different geometry. Start-up of steady shear measurements were conducted at various shear rates, $\dot{\gamma}$, beginning at $0.01s^{-1}$ and increasing at even intervals (3 steps per decade) until sample fracture/failure. Shear times were adjusted to ensure steady state was achieved. Stress relaxation upon cessation of shear was monitored, and the sample was allowed to fully relax before beginning a new measurement.

4.2 Linear Dynamic Mechanical Response

Linear viscoelastic (LVE) master curves constructed using time-temperature superposition (reference temperature, T_{ref} = 60°C, creep stress, σ = 100Pa) for varied M_n at σ = 0.47chains/nm^2

and 0.66chains/nm^2 are found in Figure 4.2A and Figure 4.2B, respectively. Neat PMA response is shown in Figure 4.2C, and horizontal shift factors as a function of temperature are plotted in Figure 4.3A along with WLF fits. Neat PMA follows expected behavioral trends as a function of M_n. First, the onset of the glassy regime shifts to lower ω as M_n increases, due to differences in T_g. Additionally, for the 23kDa sample, we do not observe an entanglement plateau, but instead the sample exhibits terminal flow following the Rouse regime. This behavior is expected for $M_n < 3M_e$, where the chains are not sufficiently long enough to entangle.[47,51] For larger M_n, the entanglement plateau extends over systematically larger frequency windows for increasing M_n before finally reaching the terminal flow regime. Additionally, the plateau modulus, G_0, is constant with M_n for neat PMA. We confirm for the linear system the zero-shear viscosity obtained from the loss modulus in the terminal regime scales as $\eta \sim {M_w}^{3.4}$.[94,95]

For the grafted particle systems of both moderate and high σ, the LVE behavior shows three striking differences compared to the corresponding neat systems. First, the glassy and rouse regimes more or less superimpose, regardless of M_n. This appears consistent with prior work which found that T_g of the GNP systems is constant over the range of M_n studied[4]. Second, for all GNP samples, the entanglement plateau is elongated relative to that of neat PMA for comparable $M_n$by decades of ω. We remark here on the prominent entanglement plateau for the sample with the shortest chains, M_n=29kg/mol. Because $M_n < 3M_e$, we do not expect to see an entanglement regime *a priori*. However, simulations by Zhou and Larson show that star polymers with short, weakly entangling arms, the effective friction imparted on these arms is significantly higher.[96] Thus, the effective entanglement molecular weight is lower for short arms. This has also been observed in comb polymers experimentally.[97] Additionally, G_0 increases slightly with decreasing

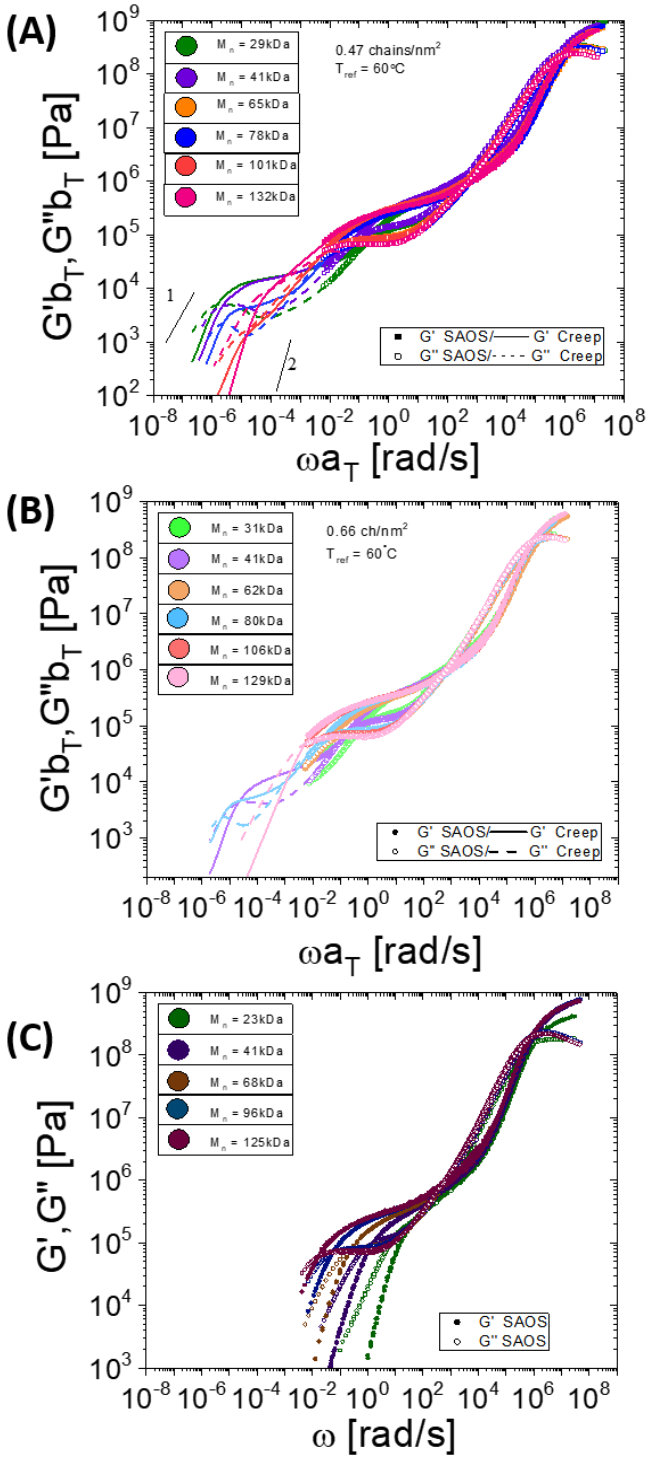

Figure 4.2: Master curves of PMA-g-SiO2 composites for (A) σ =0.47ch/nm^2; (B) σ =0.66ch/nm^2 and neat PMA melts for various M_n. Curves are shifted with T_{ref} = 60°C

M_n (increasing core weight fraction, ϕ) although this effect is less than predicted by the Guth-Gold relationship (Figure 4.3B).[98] We note the terminal regime does not appear within the frequency window accessible below 80°C (set as the upper temperature limit to protect the samples from thermal degradation) using SAOS, so here we turn to creep measurements to extend the accessible frequency range and investigate the long-time behavior of these systems. Using this technique, we observe the third significant difference between the GNP and linear systems. For $M_n >$ 100kDa, following the entanglement plateau, a slight shoulder appears before terminal flow is finally achieved. Qualitatively, this system appears somewhat similar to a linear PMA system, albeit with larger M_n. For intermediate M_n below the

100kDa threshold, a small crossover regime appears followed by an entirely separate low-ω plateau with very low modulus at low frequency. As M_n decreases further, this crossover regime disappears and the low-ω plateau extends in frequency range with increased modulus. In the lowest M_n, this low-ω plateau dominates the spectra and extends for approximately 6 decades in

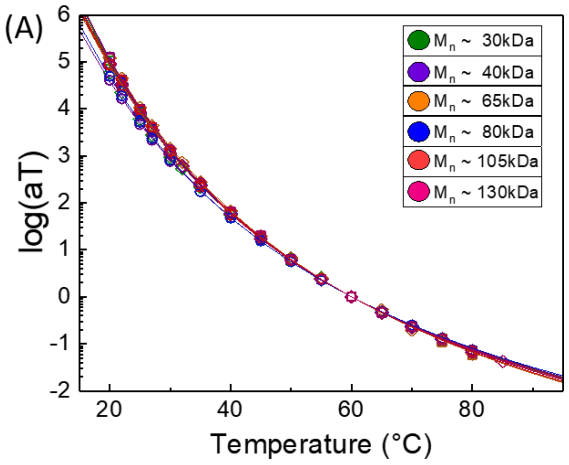

Sample	T_{ref} (°C)	C_1	C_2 (K)
N-23	60	6.52	95.0
N-44		6.31	91.5
N-63		6.59	92.1
N-98		6.19	90.0
N-125		6.26	90.8
47-29	60	6.06	88.6
47-41		6.22	89.2
47-65		6.36	91.5
47-78		6.19	90.0
47-101		6.21	90.6
47-132		6.33	90.3
66-31	60	6.61	97.4
66-41		6.40	91.2
66-62		6.83	95.8
66-82		6.13	92.5
66-106		6.60	93.1
66-129		6.16	89.0

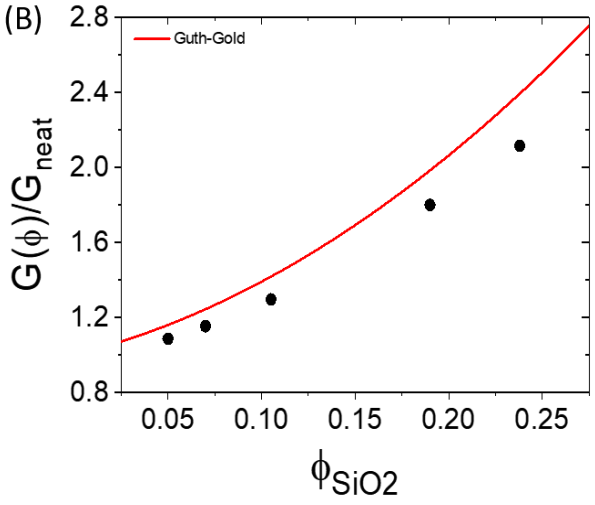

Figure 4.3: Shift factors and plateau modulus enhancement of LVE spectrum in GNP systems. (A) TTS horizontal shift factors of SAOS frequency sweeps as a function of temperature (reference temperature is 60°C) for neat PMA (◇), σ=0.47chains/nm^2 (□), and σ=0.66chains/nm^2 (○). Lines represent William-Landell-Ferry (WLF) fits, parameters in table; (B) Normalized plateau modulus against silica fraction. Red line representing the Guth-Gold equation, $G_\phi/G_{neat} = 1 + 2.5\phi + 14.1\phi^2$.[98] Plateau modulus estimated as the storage modulus corresponding at the minimum in $\tan\delta$.

ω, showing that these materials exhibit much slower dynamics than the linear melts. However, despite the large range of M_n and therefore ϕ, the polymeric response is identical in these systems for fixed σ.

We postulate that the complex dynamics of these matrix-free GNP systems can be broken down into two main categories: that of the polymer chain response and the colloidal, "cage-escape" response of the entire grafted particle which manifests as the low-ω plateau. A rational analog of these GNP systems is that of star polymers, which can be considered grafted particles with a point-size core. In a manner equivalent to the case of "multi-arm" stars[62–64], the grafted chains must first disengage with entanglements between neighboring particles/stars and retract back towards their own core. Next, because the chains are tethered at one end, the entire grafted particle/star must exchange position with the nearest neighbor in order for the system to flow. This activated process is controlled by friction imposed by neighboring particles, the magnitude of which is influenced by not only the volume fraction of cores but also the flexibility of the chains at the edge of the corona. We postulate that depending on M_n, the volume fraction of the rigid inner regimes may or may not be sufficiently large that the rigid spheres contact one another. Said another way, if the Gaussian regime is sufficiently large, the cores do not feel their nearest neighbors, and only the outer Gaussian regime dictates the relaxation via the arm retraction mechanism. However, when the volume fraction of the rigid regime increases, the system approaches the limit of packed spheres. At this point the friction in the system depends not only on the outer polymer brush, but the friction imposed by the influence of neighboring cores, which manifests as the low-ω colloidal process. We detail the brush conformation as a function of molecular weights using scaling arguments in the following section.

4.2.1 Scaling of Brush Conformation in Matrix-Free Grafted Nanoparticles

Although several other researchers have developed theories to describe the brush conformation of densely grafted spherical particles in solvent or in the presence of matrix chains,[82,99,100] we are constrained by the incompressibility condition in a solvent-free state and so we therefore assume the ends of the brushes must be space filling. Thus, we assume the conformation far from the particle surface is Gaussian-like, although we acknowledge this is a rough, first-pass approximation. In order to calculate the sizes of the stretched, rigid and Gaussian regimes, we use the following expressions:

$$R^3 \sim {R_{core}}^3 + g v_0\left(\sigma 4\pi {R_c}^2\right) \tag{4.1}$$

$$\sigma\left(\frac{R_c}{R}\right)^2 b^2(N-g) \sim \sqrt{(N-g)} \tag{4.2}$$

where N is the total number of monomers in a single chain, R_{core} is the radius of the silica core, R is the radius of the concentrated brush regime *plus* R_{core}, b is the Kuhn length, v_0 is the monomer volume, (calculated via the atomic and bond contribution method[77]), σ is the grafting density and g is number of monomers in the rigid, concentrated brush regime (CBR) of a single chain. Equation 4.2 is based upon the assumption that outside the CBR, the chains are space filling and the total monomer fraction from all chains approaches 1. The term $\sqrt{(N-g)}$ from equation 4.2 defines the size of the Gaussian regime. Rearranging equation 4.2 to solve for g yields:

$$g \sim N - \frac{1}{\sigma^2\left(\frac{R_{core}}{R}\right)^4 b^4} \tag{4.3}$$

Substituting equation 4.3 into 4.1 we obtain:

$$\frac{4}{3}\pi\frac{\left(R^3-{R_{core}}^4\right)}{fv_0}+\frac{1}{\sigma^2\left(\frac{R_{core}}{R}\right)^4 b^4}-N\sim 0 \quad (4.4)$$

where f is the total number of chains per particle. We calculate the dimensions for various M_n for both σ=0.47chains/nm^2 0.66chains/nm^2 assuming a core radius of 8nm in Table 4.2. The height of the CPB region, h_{CPB} is calculated as $R-R_{core}$ and compared to measured brush height from SAXS (see section 3.3). The molecular weight of the Gaussian regime, $M_{n,G}$ is calculated as $(N-g)*M_{monomer}$ where the mass of the PMA monomer, $M_{monomer}$, is taken as 86g/mol. We use these values as an estimate to the transition between the rigid CPB and Gaussian regimes, although we acknowledge there is likely not a sharp cutoff at a fixed critical radius, and rather that the polymer brush confirmation changes gradually as a function of distance from the surface of the nanoparticle.

Table 4.2: Grafted brush dimensions as a function of M_n from scaling theory. R_{core}=8nm

Sample	N	g	R	h_{CPB} nm	h_{tot} nm	$h_{tot,SAXS}$ nm	$M_{n,G}$ kg/mol
47-132	1534	897	19.3	11.3	18.5	17.5	54.8
47-101	1174	701	17.9	9.9	16.1	14.0	40.6
47-78	907	552	16.7	8.7	14.0	11.8	30.5
47-65	721	446	15.6	7.6	12.4	11.3	23.7
47-41	477	300	14.0	6.0	9.8	7.4	15.2
47-29	337	213	12.8	4.8	8.0	6.0	10.6
66-129	1500	960	21.9	13.9	20.6	19.4	46.4
66-106	1233	803	20.7	12.7	18.7	17.0	37.0
66-80	930	619	19.1	11.1	16.1	15.5	26.7
66-62	721	488	17.8	9.8	14.1	11.7	20.0
66-41	477	330	15.8	7.8	11.3	8.5	12.6
66-31	360	252	14.7	6.7	9.6	6.7	9.3

Furthermore, we can calculate the packing fraction of the rigid spheres as $\eta_{rigid} = C\frac{4\pi}{3}\rho R^3$, where ρ is the number density of silica cores and C is a dimensionless scaling constant (Figure 4.4). As a function of M_n, a plateau emerges where the packing fraction approaches some asymptotic limit at high ϕ_{SiO_2}/low M_n. When C=1, the packing density approaches 0.74, or the packing density of close packed spheres with crystalline order; however, we show in Chapter 3 that these systems are isotropic and non-crystalline. Therefore, we select C such that η_{rigid} approaches 0.58, or packing fraction of hard spheres at the glass transition.[101] This validates the idea that in samples which exhibit the low-ω colloidal plateau, the system resembles that of a true colloid system, based on the conformation of the brush. The transition from colloid-dominated to polymer-dominated appears where the volume fraction of the rigid cores falls just below that of a colloidal glass.

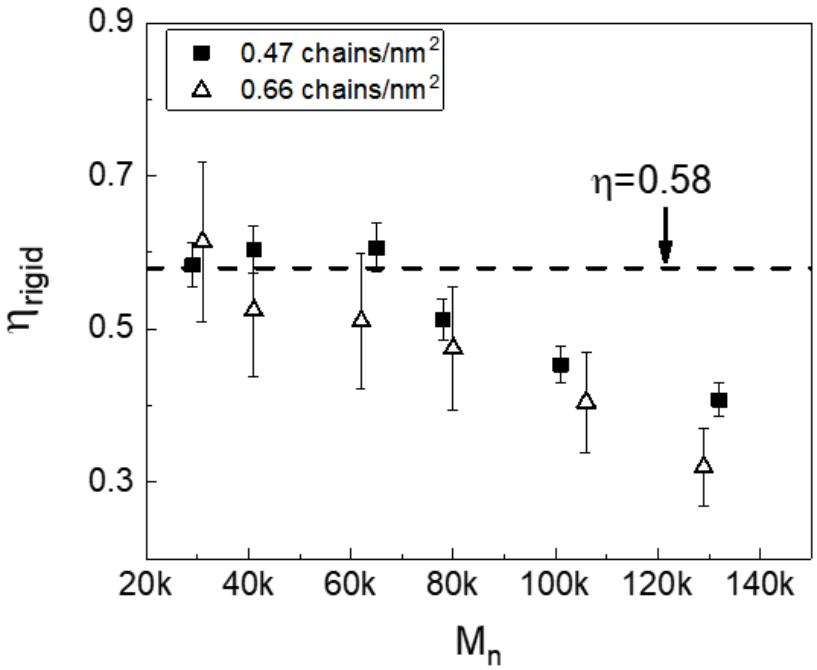

Figure 4.4: Packing fraction of rigid spheres from scaling theory as a function of M_n. Dashed line represent packing fraction at the glass transition of hard spheres, 0.58. Error analysis from polydispersity of core size and number density of silica cores.

Based on the above calculations, the polymeric, or arm retraction mode, is modeled using the Branch-on-Branch (BoB) model.[102] However, the question remains: what fraction of the grafted chain actively participates in the arm retraction mechanism? We therefore fit the data assuming either i) the full chain participates in arm retraction or ii) only the Gaussian regime retracts, thus the effective molecular weight used as a model parameter is $M_{n,G}$. For samples which exhibit a low-ω plateau, we combine the BoB model with the linear viscoelasticity model for colloidal hard sphere suspensions based on mode coupling theory (MCT)[65,103,104]:

$$G'(\omega) = G_P + G_\sigma \left[\Gamma(1-a')\cos\left(\frac{\pi a'}{2}\right)(\omega t_\sigma)^{a'} - \beta\Gamma(1+b')\cos\left(\frac{\pi b'}{2}\right)(\omega t_\sigma)^{-b'}\right] + G'_D(\omega) \quad (4.5)$$

$$G''(\omega) = G_\sigma \left[\Gamma(1-a')\sin\left(\frac{\pi a'}{2}\right)(\omega t_\sigma)^{a'} - \beta\Gamma(1+b')\sin\left(\frac{\pi b'}{2}\right)(\omega t_\sigma)^{-b'}\right] + G''_D(\omega) + \eta_\infty\omega \quad (4.6)$$

$$G'_D(\omega) = G''_D(\omega) = \frac{6}{5\pi}\frac{k_B T}{a^3}\phi^2 g(2a,\phi)[\omega\tau_D]^{1/2} \quad (4.7)$$

Figure 4.5 shows fits for various samples for σ =0.47chains/nm^2. We find that the entanglement plateau is well fit using the BoB model. For large M_n, it appears that only the outer Gaussian portion of the chain participates in arm retraction. As M_n decreases, apparently the full chain participates in the arm retraction mechanism. This transition occurs where the packing fraction shows these sample transitions to a colloidal system. This perhaps indicates that confinement effects result in overlap of neighboring brushes; thus the chains must retract further to disengage from neighboring particles to increase in the more tightly packed systems. Additionally, although the MCT model was developed for hard spheres up to the glass transition, it has been shown that it can be nicely extended to highly concentrated suspensions of latex particles,[105] PNIPAM microgels,[106,107] and star polymers.[65] In our case, we demonstrate the MCT model can effectively capture the colloidal plateau by simply using hard-spheres parameters.

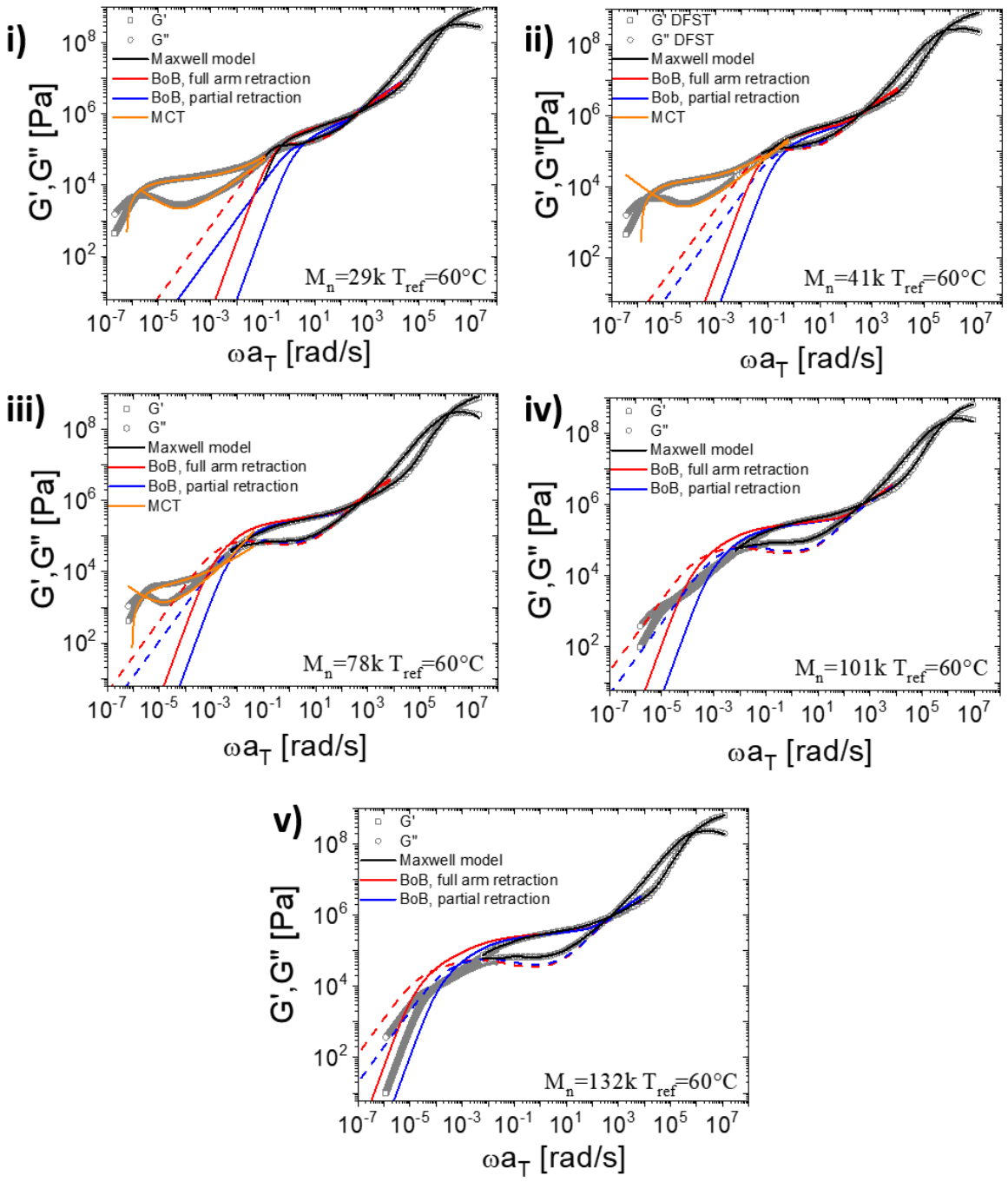

Figure 4.5: Fits of LVE spectra for σ=0.47chains/nm^2 grafted particles. Data are represented by symbols, G' (□) and G''(○); black lines represent high-ω Maxwell model fits; BoB model fits assuming both full and partial arm retraction are shown by red and blue lines, respectively. If a secondary plateau is present, MCT fits are shown by orange lines. Fits are shown for i) 29kDa; ii) 41kDa; iii) iii) 78kDa; iv) 101kDa; v) 132kDa.

The divergence of the loss modulus at low frequencies occurs because the model does not include a dissipative term which describes the hopping dynamics as discussed by Crassous et al.[106] Additionally, the small crossover found for moderate M_n systems may be as a result of convolution between the arm retraction and colloidal modes, although this is not yet well understood

A plot of the terminal relaxation time, τ_{term} as well as the relaxation time for arm retraction τ_{arm} as a function of reduced molecular weight (Figure 4.6) shows more clearly the two distinct processes in the GNPs. A deviation in behavior as a function of M_n is found between 80kDa-100kDa. The terminal relaxation characteristic time, is taken directly from the lowest G'/G'' crossover, but the arm retraction time is taken from the BoB model fits. Note further that one could estimate the characteristic times from $\tan\delta$ in reasonable agreement (and with an identical trend) with those reported in Figure 4.6A. However, due to the convolution of the two processes, it is difficult to assess unambiguously (Figure 4.6B) where the arm retraction process relaxation occurs for high M_n, so we stick to those based on the model.

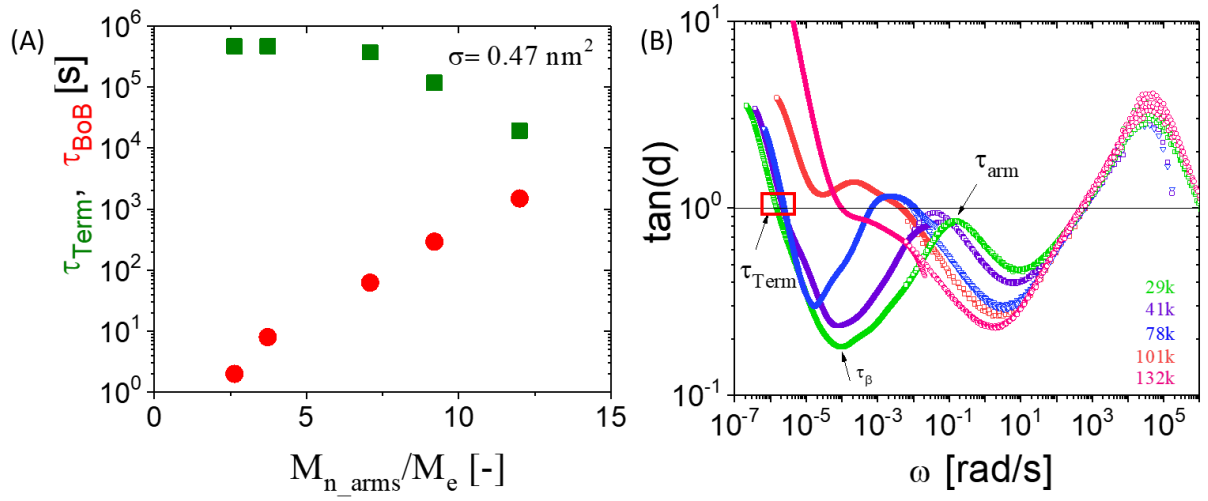

Figure 4.6: Relaxation times in matrix-free polymer grafted nanoparticles. (A) Arm relaxation times from BoB model as a function of reduced molecular weight for PMA grafted composites with σ=0.47chains/nm^2. (B) $\tan\delta$ as a function of frequency for PMA grafted composites with σ=0.47chains/nm^2. For higher molecular weights where the arm and colloidal relaxations are not well separated, estimating the characteristic times of the arm retraction is inexact, thus we stick to values from model fits as described above.

Furthermore, from rubber elasticity theory, the characteristic length, ξ, can be defined as the length scale through which stresses are translated throughout the network.[84] We can adapt this to the characteristic length for the colloidal network as $\xi = \left({kT}/{G'_{0,colloidal}}\right)^{\frac{1}{3}}$ where $G'_{0,colloidal}$ is the plateau modulus of the low frequency, or colloidal, plateau. Indeed, when plotted against brush height as measured by SAXS, ξ agrees exceptionally well with h (Figure 4.7), confirming the low-ω plateau pertains to the "cage-hopping" mechanism of individual grafted particles. Finally, in Figure 4.8 we compare the normalized viscosity as a function of reduced molecular weight (M_n/M_e) of the grafted silica particles to that of conventional star polymer melts.[62,108] It is clear that for the high molecular weight systems, the dynamics are dominated by the polymeric behavior, and these systems approach that of star polymers. Interestingly, this structural and mechanical transition also appears in the M_n range where the relative permeability enhancement of small gases is maximized. Although the diffusion of small gases occurs on much shorter time scales than the colloidal relaxation process, the linear mechanical properties allude to

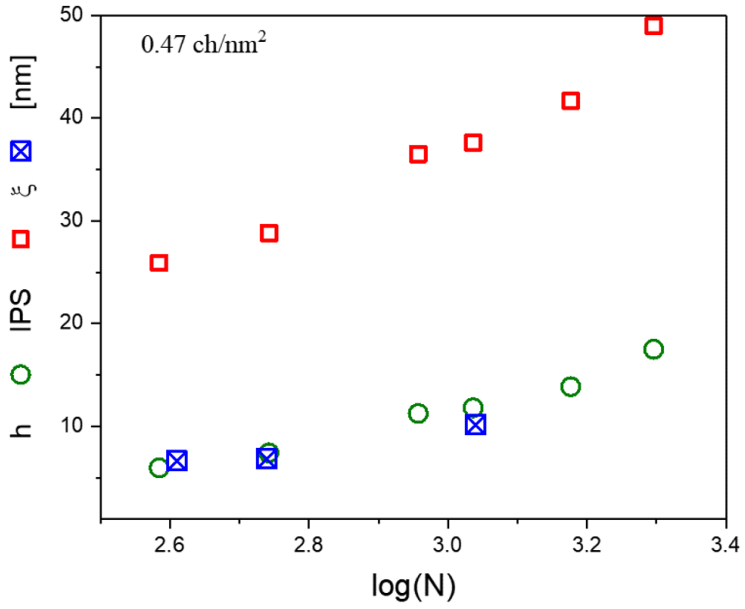

Figure 4.7: Colloidal cage size versus brush height, h and center-to-center inter-particle spacing (IPS) from SAXS as a function of degree of polymerization

heterogeneous structural signatures not previously detected in morphological characterization of the bulk. It is feasible that this structural transition would also affect faster dynamics properties which may be more relevant to the diffusion time scales, which we probe further in Chapter 5.

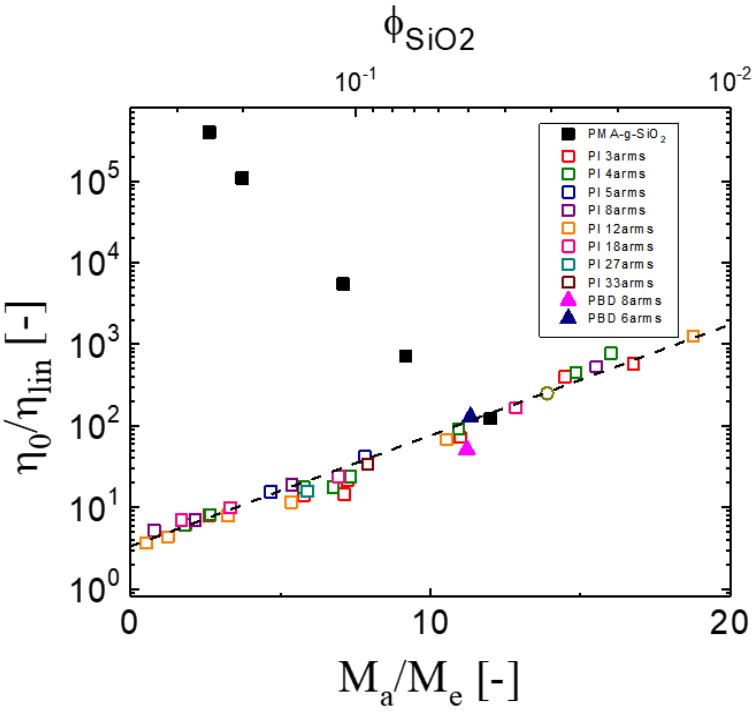

Figure 4.8: Comparison of viscosity of matrix-free GNPs to star polymer melts. [62,108]

Finally, in Chapter 2, we showed that membranes of matrix-free GNPs suffered significantly less from aging problems relative to neat linear melts. We postulate that the retardation of the terminal flow regime by several decades even at temperatures well above T_g, in addition to the permanently frustrated packing caused by grafting, leads to no change in permeability after aggressive thermal annealing (Bilchak, Buenning, & al., 2017). Therefore, LVE measurements suggest that in addition to faster diffusion, grafted nanoparticle constructs may be useful to extend the lifetime of highly permeable polymers which are as of yet unsuitable for membrane separation applications as a result of aging issues.

4.3 Non-linear Response

The viability of matrix-free GNP membranes in commercial settings depends not only on their transport properties but also whether these materials are mechanically robust enough to withstand harsh operating environments. To that end, we study the mechanical properties of these GNP systems using non-linear start up shear and compare their performance to that of linear melts of comparable M_n. We test matrix free GNP samples at three M_n (~41kDa, 80kDa, and 130kDa) and two σ values (0.47 and 0.66 chains/nm^2) as well as the neat analogs for each M_n. However, we determined that the GNP samples with M_n~41kDa fractured during the first strain rate test, at the lowest achievable rate on the instrument . These samples then, were too brittle to measure start-up steady shear even at very small strain rates, and thus our analysis is limited to the M_n~ 80 and 130kDa materials.

We show in Figure 4.9 the steady-state viscosity (normalized to the zero shear viscosity from SAOS/creep measurements) as a function of Weissenberg number, $W_{i,e}$, where $W_{i,e}$ is

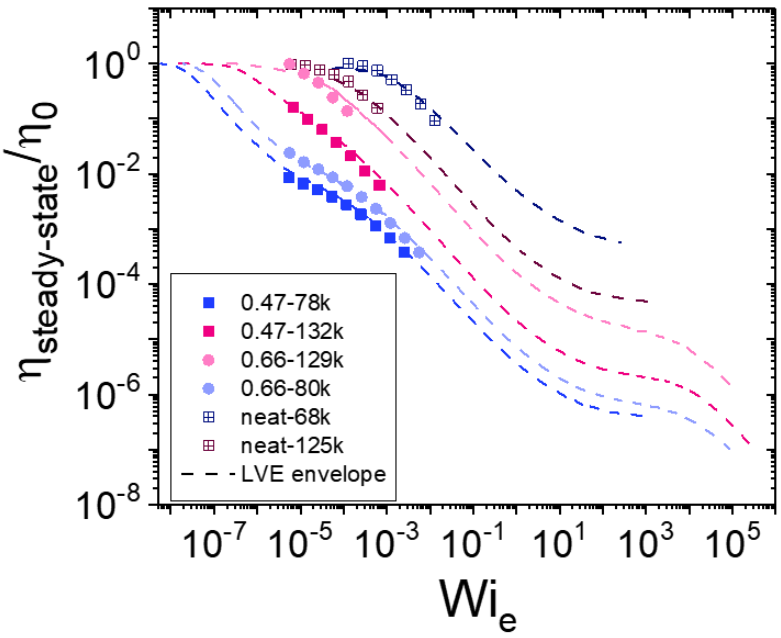

Figure 4.9: Normalized steady-state viscosity as a function of Weissenberg number

defined as $\dot{\gamma}\tau_e$ where τ_e is the entanglement relaxation time as found in section 4.2. The steady-state viscosity from start-up shear measurements superimposes well with the linear viscoelastic envelope from SAOS/creep measurements, which show that the matrix-free grafted nanoparticles follow the Cox-Merz rule.[109]

On average, the GNP systems are more brittle than their neat counterparts (Figure 4.10), though the difference in failure strain rate decreases with increasing M_n. The effect of σ on failure strain rate is less obvious. Figure 4.11 compares stress versus strain at various strain amplitude, γ_0, as a function of both M_n and graft density (raw stress vs. strain, viscosity vs. time, and relaxation stress vs. time at cessation of flow data can be found in Appendix A.10). The stress is

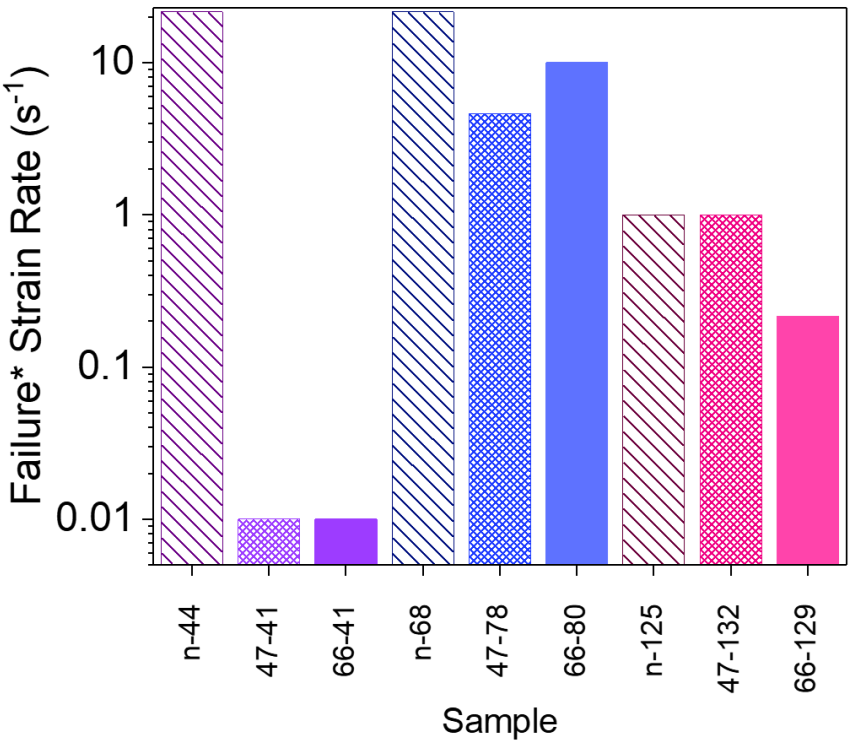

Figure 4.10: Failure strain rate of various GNP and neat PMA samples. Failure strain rate is defined as the experimentally tested strain rate where sample fractured and did not reach steady state. For the GNPs with M_n~41kDa, samples fractured during the lowest strain rate achievable on the instrument

normalized by the stress measured in the linear viscoelastic regime as a product of the entanglement plateau modulus, G_{N0}, and the strain amplitude, γ_0. Figure 4.11A and B compare neat and GNP samples at fixed M_n for ~80kDa and 130kDa, respectively. For the ~80kDa system, both GNP samples show significant increases in yield stress with the appearance of a stronger stress overshoot at higher strain rates compared to neat PMA. There is little effect of graft density for M_n ~80kDa but there is a slight enhancement in the stress overshoot for σ=0.66chains/nm^2 for

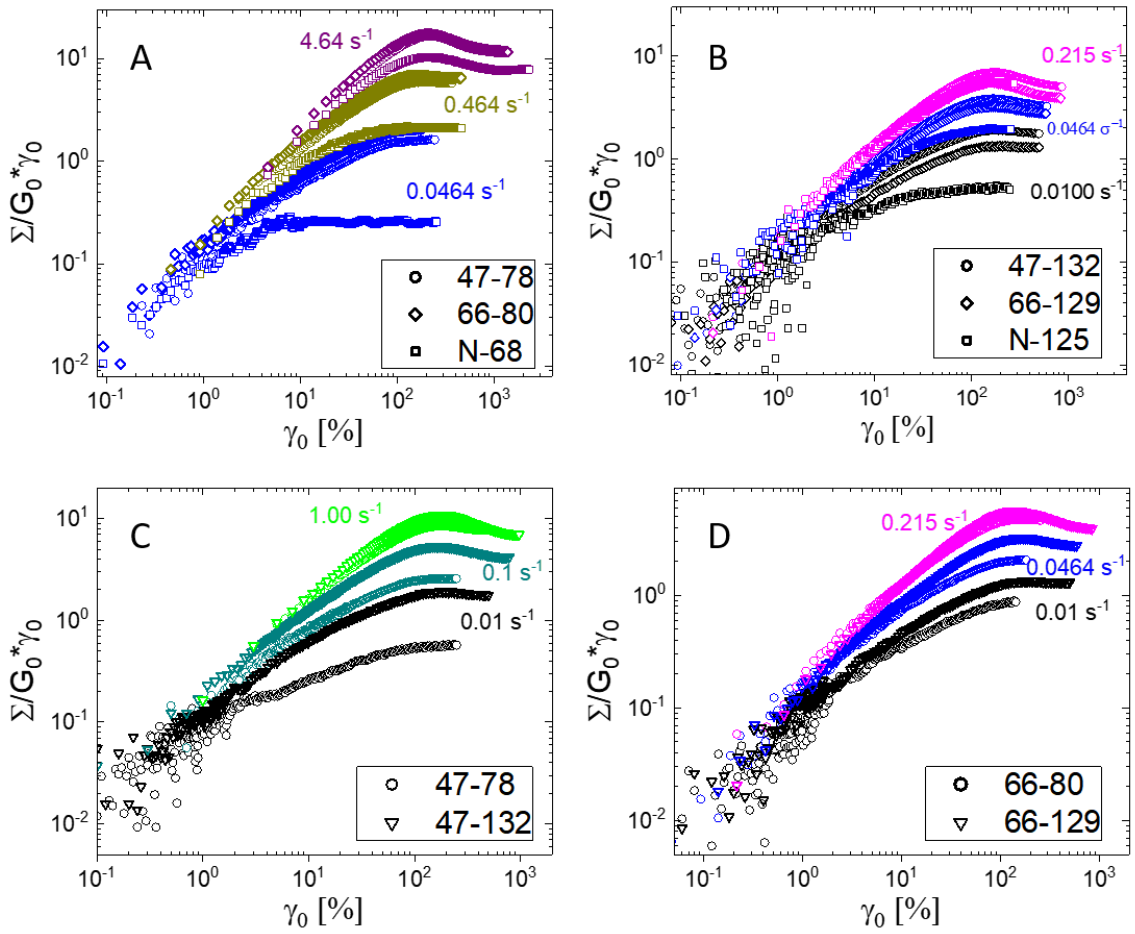

Figure 4.11: Non-linear start up shear of PMA-g-SiO_2 composites at various strain rates. Normalized stress versus strain curves comparing effects of graft density (including neat linear melts) at fixed M_n for (A) ~80kDa, and (B) 130kDa and comparing the effects of M_n at fixed σ for (C) 0.47chains/nm^2 and (D) 0.66chains/nm^2. Representative strain rates are chosen to be roughly evenly spaced and where data are available for all samples, depending on facture strain rate.

the case of long chains (M_n ≅130kDa). For fixed graft density (Figure 4.11C and D), the strain-hardening effect increases as M_n increases, however this effect is diminished as strain rate increases.

Previous studies have shown that mechanical reinforcement of grafted nanoparticles dispersed in linear polymer chains (i.e. **not** matrix-free) is strongest when grafted particles form networks *and* there is significant interaction between the grafted brushes of adjacent particles.[110] In our case, due to the materials being matrix-free, the samples can all be considered as a "percolated network", so here we focus on the contribution from the polymer chains. Figure 4.12A shows the yield stress, Σ_y (defined as the maximum of the stress overshoot peak) normalized by the steady-state plateau stress, Σ_y as a function of strain rate, $\dot{\gamma}$ (note, while stress is generally represented by a lower-case sigma, σ, we use the upper-case to distinguish from graft density). For M_n~ 130kg/mol, the GNP samples show a stress overshoot at very low strain rates compared to the neat polymer. On the other hand, the intermediate chain lengths of M_n ~ 80kg/mol do not show this solid-like overshoot until higher strains, but the degree of reinforcement increases with

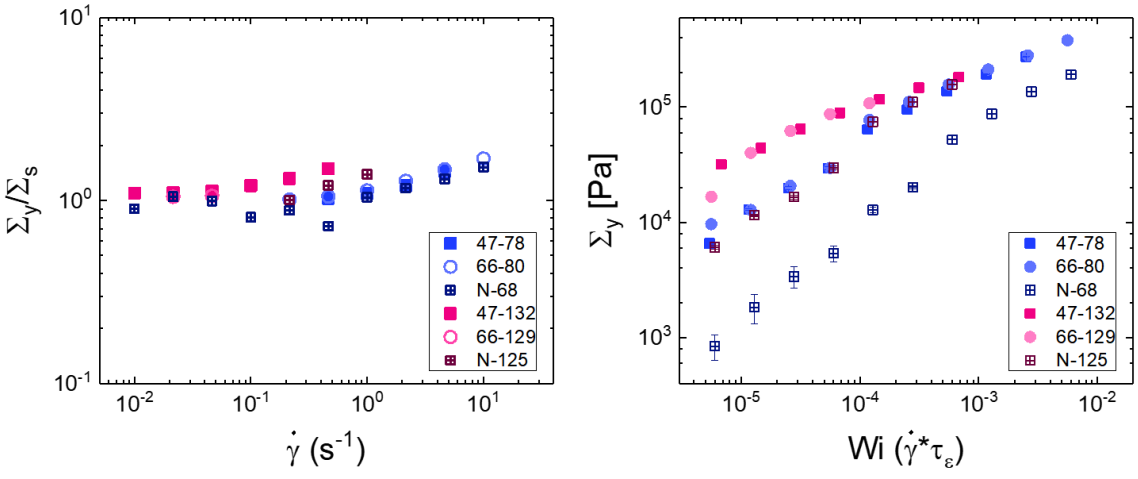

Figure 4.12: Mechanical reinforcement of matrix-free grafted nanoparticles. (A) Yield stress normalized by plateau steady-state stress vs. strain rate; (B) Yield stress vs. Weissenberg number.

increases strain rate. Figure 4.12B plots the yield stress as a function of $W_{i,e}$. For low strain rates, the yield stress in the GNPs with large M_n is significantly higher than the neat polymer and also the GNPs with intermediate M_n. However, at high strains, the yield stress is similar for all GNP samples, although the composites are still reinforced compared to the neat polymer.

We recall that for small M_n, the brush conformation results in these samples behaving effectively as rigid spheres. In these cases, the Gaussian portion of the chain which can interact with neighboring grafted particles is very small, and thus cannot transfer stress efficiently. Indeed, the non-linear start-up shear shows for GNP systems with $M_n < 40$kDa showed brittle fracture even at the smallest experimentally accessible strain rates. For M_n larger than the limit where the particles behave as packed, rigid spheres, the fraction of the Gaussian regime increases and the polymeric behavior of these materials dominates. Therefore, the chains are able to interact with neighboring particles and transfer stress throughout the network, resulting in mechanical reinforcement. Although samples at intermediate and large M_n fracture at lower strain rates compared to their neat counterparts, the GNP materials can tolerate a significantly higher stress before failure than the neat melts. Additionally, for low W_i, GNP materials are significantly more tough than the neat melts. For use in membrane application, these increases in mechanical strength are a potentially valuable benefit to matrix-free GNP constructs in addition to their remarkable transport properties.

Chapter 5

Segmental and Secondary Relaxations Of Matrix-Free Grafted Nanoparticles

In this chapter, we study the segmental and secondary relaxations of matrix-free GNPs and compare their behavior to that of neat PMA melts using broadband dielectric spectroscopy (BDS). Previous BDS studies of polymer nanocomposites, and grafted nanoparticles specifically have focused on systems where the core particle is either much smaller or much larger than the polymer radius of gyration. Here we investigate the effects of grafting chains to the surface of particles where the particle radius $r \sim R_g$.

For a dielectric material exposed to an electromagnetic field of sufficiently low strength, a temporary separation of the positively charged nucleus and negatively charged electrons is induced, called the dielectric displacement. This displacement, D, as described by Maxwell is expressed as: $D = \varepsilon^* \varepsilon_0 E$ where ε^* is the frequency (or time) dependent complex dielectric permittivity, ε_0 is the dielectric permittivity of a vacuum ($\varepsilon_0 = 8.854 \text{ x } 10^{-12}$ F/m) and E describes the electric field.[46] The complex permittivity as a function of frequency, ω, is further described as: $\varepsilon^*(\omega) = \varepsilon'(\omega) - i\varepsilon''(\omega)$ where $\varepsilon'(\omega)$ is the real part, also known as the dielectric permittivity, and $\varepsilon''(\omega)$ is the imaginary part, also known as the dielectric loss. The complex permittivity is related to the relaxation time distribution through a one-sided Fourier transformation $\varepsilon^*(\omega) = \varepsilon_\infty - \int_0^\infty \frac{d\varepsilon(t)}{dt} e^{-i\omega t} dt$. Experimentally, the complex permittivity is calculated from directly measuring the complex impedance, Z^* , in the presence of a sinusoidal electric field,

$E^*(\omega), \varepsilon^*(\omega) = \frac{J^*(\omega)}{i\omega\varepsilon_0 E^*(\omega)} = \frac{1}{i\omega Z^*(\omega) C_0}$ where $J^*(\omega)$ is the complex current density and C_0 is the vacuum capacitance of the sample holder arrangement. Additionally, the real and imaginary parts of ε^* are related by the Kramers/Kronig relations, therefore the real and imaginary spectra measured experimentally contain the same information.

For the GNO systems, the dielectric loss shows the segmental relaxation is significantly broadened and shifted to lower frequencies. The difference between the GNP segmental relaxation and the neat systems is most pronounced for low M_n; however, between GNP systems, the effects of M_n on the characteristic time for the segmental relaxation is small, which corroborate SAOS and DSC measurements which show minimal effects of M_n on T_g. We fit the alpha relaxation in the frequency spectra with the Inter-Layer Method (ILM)[58,111,112] which more accurately describes the dielectric response of heterogeneous polymeric systems which exhibit an interfacial layer of reduced polymer mobility as a result of the presence of inorganic fillers.

The faster secondary relaxations are accessible at low temperatures, and for PMA these relaxations are generally attributed to the rotations of the ester side groups. We show that in the grafted system, the secondary dynamics show non-monotonic behavior with M_n. For low and high M_n, the grafted system essentially follows the neat secondary dynamics. But for intermediate M_n, we see the grafted system has *faster* secondary dynamics than the corresponding neat. The faster secondary dynamics may further confirm there is more local free volume in the intermediate M_n grafted samples, and hence faster diffusion, that was explored in Chapter 2.

5.1 Materials and Methods

PMA grafted SiO_2 nanoparticles (15nm ± 4 nm diameter, σ = 0.43chains/nm^2) as well as neat PMA samples were synthesized and solvent cast using procedures detailed in Section 4.1.

Weight fractions were checked using TGA by burning in O_2 to 800°C at 10°C/min. Afterwards, all samples were stored in a dry box until use. Details of samples used for this study can be found in Table 5.1 below.

Samples were molded for BDS studies by sandwiching directly between two gold electrodes to a thickness of 0.1mm and 14mm diameter at 80°C. A Teflon spacer ring was used to maintain sample thickness and diameter at elevated temperature. After pressing, samples were annealed for at least 24 hours at 80°C under vacuum to remove any traces of water vapor. BDS measurements were taken using a Novocontrol Concept-80 system with Alpha-A impendence analyzer over a frequency range of 10^7-10^{-2} Hz. Temperature sweeps from 353K-133K were conducted using a Quatro Cryosystem temperature controller under N_2 atmosphere. A thermal stabilization of 20min was performed for each temperature step to ensure thermal equilibrium in the sample and cell before measuring.

Table 5.1: BDS Sample Specifications

Sample Class	Sample Name	Graft Density σ chains/nm²	Molecular Weight M_n g/mol	Polydispersity Đ	Weight Fraction Silica (wt%)
GNP	43-27	0.43	29,900	1.14	30.2 ± 0.001
	43-77		77,100	1.15	11.8 ± 0.2
	47-132		132,100	1.18	5.9 ± 0.01
neat	N-23	N/A	23,100	1.09	N/A
	N-62		62,800	1.17	
	N-125		125,000	1.23	

5.2 Segmental (α) Relaxation Dynamics of PMA Nanocomposites

For most neat polymers in the bulk state, the peak in $\varepsilon''(\omega)$ corresponding to the dynamic glass transition is termed the α-relaxation process. This peak describes the relaxation time

distribution for chain segment relaxation. For polymers with permanent dipole moments along the backbone, so-called "type A" polymers, an additional α'prime peak can be detected, corresponding to the whole-chain relaxation. The scope of this work, however, covers only polymers without a dipole along the backbone, so although whole chain relaxation still occurs, it is not detectable with BDS.[46] Additionally, using a generalized regularization method (similar to the CONTIN algorithm), we can obtain the relaxation distribution as a function of time, $g[\ln \tau]$, as opposed to frequency. This can help to decouple multiple convoluted relaxation processes which are too subtle to see in the dielectric loss spectra. We compare ε" and $g[\ln \tau]$ for GNP and neat PMA samples of similar M_n in Figure 5.1. For the composite systems, there is a shift in the peak location to lower ω /longer relaxation times, in addition to a systematic broadening of the α-relaxation towards low ω. This broadening is especially apparent in the $g[\ln \tau]$ where the distribution of relaxation times show a significant shoulder. These effects are more prominent in low M_n systems. The Maxwell-Wagner-Sillars (MWS) process is convoluted with the conductivity in the neat PMA and GNP systems. Qualitatively, these results are consistent with poly(2-vinylpyridine) systems with roughly similar graft density studied by Holt et al.[58] although the shifts to lower frequencies in our systems appear to be stronger. For a more quantitative analysis of the BDS data, we fit the loss spectra with the inter-layer model (ILM) which we detail in the next section.

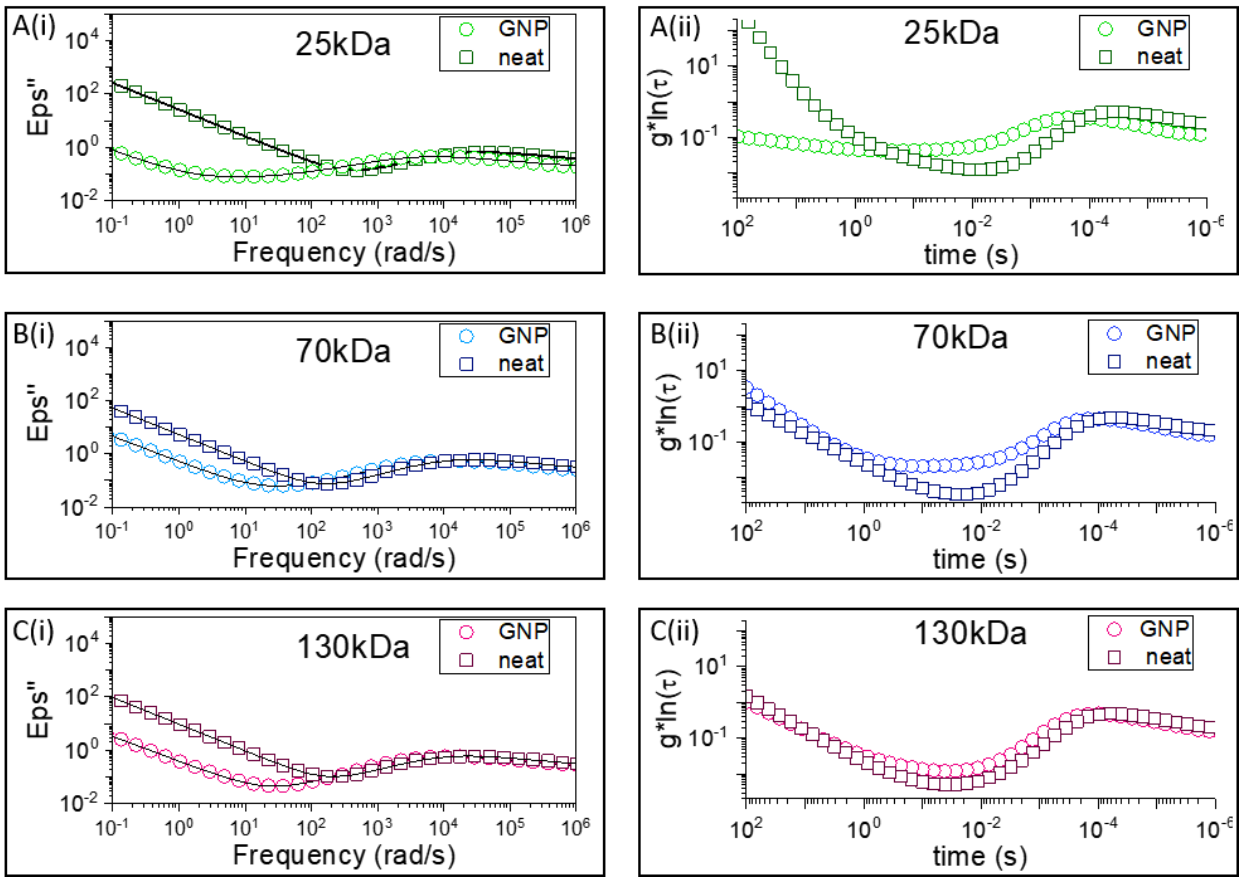

Figure 5.1: Segmental relaxation in BDS. Dielectric loss ε'' (i) and relaxation distribution $g[\ln\tau]$ (ii) for GNP and neat PMA samples with $M_n \approx$ 25kDa (A); 75kDa (B); and 130kDa (C). T = 40°C. Lines on ε'' spectra correspond to interlayer method fits (see section 5.2.1)

5.2.1 Inter-Layer Model for α-Relaxation in Composite Systems

Until recently, interfacial contributions to the BDS spectra in polymer nanocomposites were traditionally fit by treating the shoulder which appears at low ω as a completely separate relaxation process. Therefore, the spectra were fit with two Havriliak-Negami (HN) functions[46], which assumes contributions from the bulk-like polymer and the interfacial polymer are additive.[111] However, this assumption is fundamentally inaccurate, and the interference terms

from dielectric boundaries should be taken into account for heterogeneous systems. Therefore, we use the so-called "inter-layer" model (ILM) which includes all interference terms and attributes the low ω shoulder to a layer near the particle surface where the polymer segments are significantly less mobile, but whose relaxations are still coupled to those of the bulk-like polymer segments far from the particle surface.[59,111] Note, for GNP systems, the interfacial layer is *not* the same as the grafted corona size, or even the stretched CBR layer as described previously in Section 4.2.1. For the neat polymer samples, the data are well fit using a single HN curve. Extracting the average relaxation time at each temperature and plotting as a function of reduced temperature (Figure 5.2A) from fits of the loss spectra, it is clear the GNP systems relax slower than the neat PMA. The difference in relaxation time is significantly more pronounced in the low M_n samples. Fitting the temperature dependent relaxation times with the Vogel-Fulcher-Tamman (VFT) equation we can extract the fragility, m, and glass transition temperature (Table 5.2). Here, we define $T_{g,BDS}$ where $\log(\tau)$ =100. The BDS results show that although there is a broader distribution of relaxation times in the GNP systems, the effect of M_n on T_g is small in grafted composites, which corroborates findings from SAOS and DSC measurements (we note that the difference in T_g as measured by DSC and BDS arises from the difference in cooling rates, which will affect the absolute value of T_g[111]).

Figure 5.2B shows the interfacial layer thickness for the two composite systems at different M_n as a function of temperature. The temperature dependence of the interfacial layer thickness monotonically increases with decreasing M_n. A steeper temperature dependence of the dynamic heterogeneity length scale is expected for systems with higher fragility[113], and it has been argued that there is a direct relationship between the interfacial layer and the dynamic heterogeneity length scale[114,115] for polymer composite systems.[116] However, the fragility indices calculated for GNPs

of different M_n do not differ by an appreciable amount. Additionally, the thickness of the interfacial layer is relatively small for PMA systems compared to other polymer-NP composites[59,111], so for this reason, it is difficult to draw any conclusions about the M_n dependence of free volume from segmental dynamics alone. Therefore, in the next section we study the secondary relaxations using BDS at temperatures well below the glass transition.

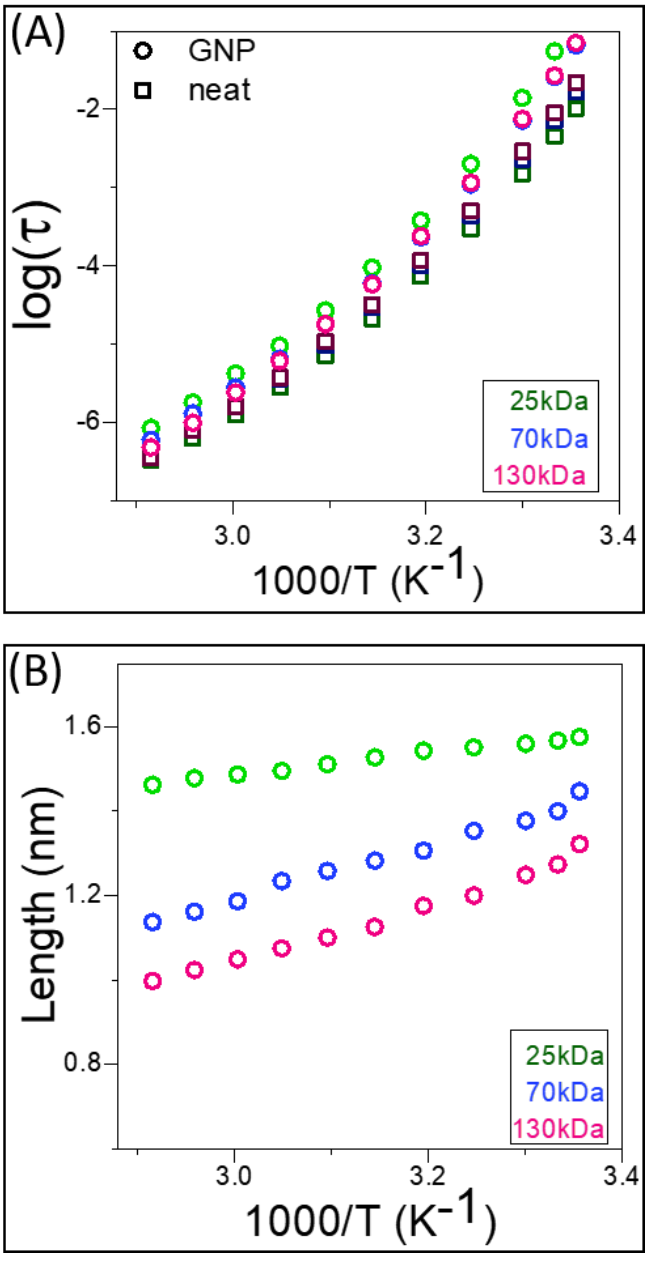

Figure 5.2: Temperature dependence of α-relaxation and interfacial layer. (A) α-relaxation time from ILM fit (or single HN fit for neat PMA) as a function of reduced temperature. (B) Interfacial layer thickness as a function of reduced temperature for GNP systems

Table 5.2: VFT fit parameters of α-relaxation from BDS

Sample		T_0 (K)	$T_{g,BDS}$ (K)	m
GNP	G-27	251.8	288.3	106.3
	G-77	249.4	286.7	104.7
	G-132	243.7	286.2	98.0
neat	N-23	243.4	282.4	101.0
	N-68	244.7	283.5	101.7
	N-125	244.4	284.03	100.4

5.3 Secondary (β and β') Relaxation Dynamics from BDS

Far below the glass transition temperature, PMA exhibits a faster relaxation process, most likely due to rotations of side groups or other small relaxations on the order of ~a couple monomers. Typically, the dielectric loss of these secondary relaxations as a function of frequency can be described as a Cole-Cole process and exhibit an Arrhenius temperature dependence.[46] In PMA specifically, the secondary process is a convolution of a larger, main relaxation (termed the β-relaxation), and a smaller β'-relaxation which more emergent in the $g[\ln(\tau)]$ spectra (Figure 5.3).

Figure 5.4 shows ε' as a function of frequency at -100°C ($T - T_g$ = -120°C) for GNPs and neat PMA of various average molecular weights. Additionally, the relaxation time of the β-process

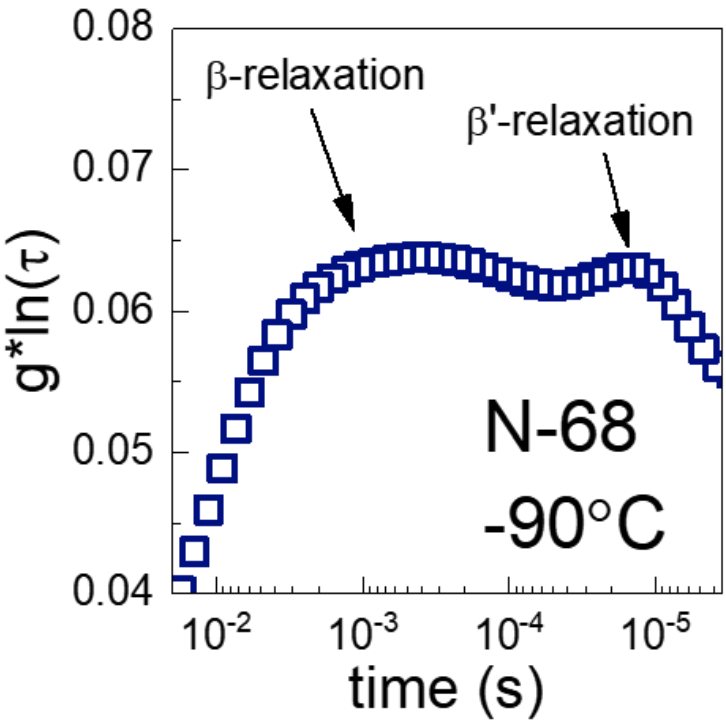

Figure 5.3: Secondary relaxation time distribution as a function of time for neat PMA

extracted from a Cole-Cole fit is plotted as a function of reduced temperature. For low M_n samples, the shape and relaxation times of the GNP and neat samples are similar until very low temperatures, where the dynamics of the GNP sample slows considerably compared to the neat PMA sample. Additionally, at high M_n, the relaxation times of the grafted material are identical to the neat polymer relaxation time for all temperatures studied. However, for the moderate M_n, the main secondary relaxation process of the GNP system is *faster* at all temperatures compared to the neat PMA. For the smaller β'-process, the composite system is consistently slower than the neat polymer (not shown). Activation energies determined by fitting the temperature dependence of the relaxation times are shown in Table 5.3.

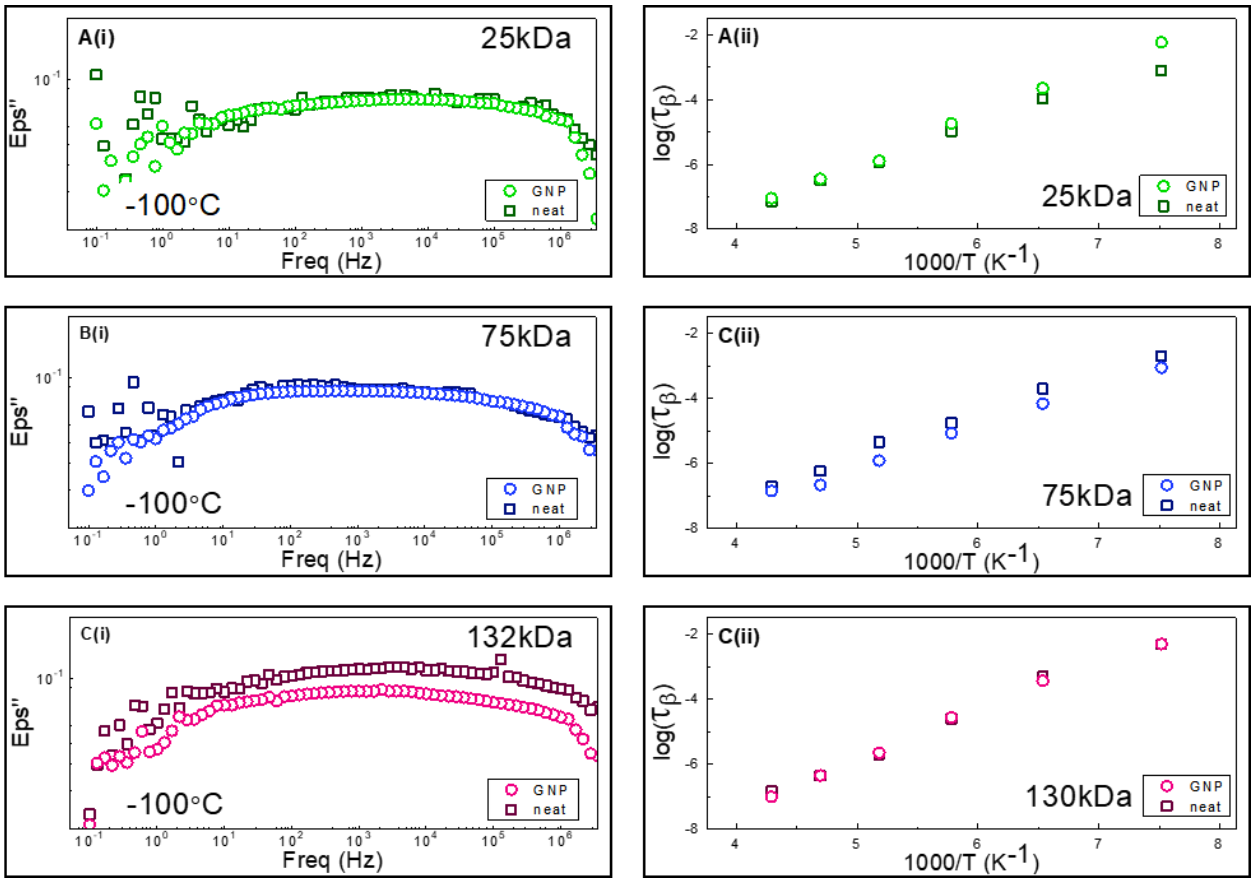

Figure 5.4: Secondary relaxation from BDS in PMA composites. Dielectric loss, ε'', (i) as a function of frequency at -100°C and relaxation time as a function of reduced temperature (ii) for GNP and neat PMA samples with $M_n \approx$ 25kDa (A); 75kDa (B); and 130kDa (C).

To more clearly show the difference in relaxation time between the GNP and neat systems, the relative relaxation times $\log(\tau_{\beta,\phi}/\tau_{\beta,neat})$ are plotted against reduced temperature in Figure 5.5A. It is clear the main β-relaxation process shows non-monotonic behavior as a function of M_n in matrix-free polymer grafted nanoparticle materials. At moderate values of M_n, the secondary relaxations are approximately 30% faster than neat PMA with a similar molecular weight. We note that this minimum in relaxation time occurs in the range where the density of the polymer phase was found to be less than that of neat PMA as previously reported in Figure 2.5 of Chapter 2 (Figure 5.5B).

Table 5.3: Secondary relaxation processes activation energies

Sample		β-process E_A (eV)	β'-process E_A (eV)
GNP	G-27	0.130	0.191
	G-77	0.106	0.164
	G-132	0.131	0.199
neat	N-23	0.110	0.175
	N-68	0.109	0.153
	N-125	0.126	0.153

We postulate that the reduced density of the polymer phase leads to faster side group rotations and/or other small length scale relaxations detected by BDS. The reduction in relaxation times also coincides with the maximum in relative permeability detailed in Chapter 2. The faster dynamics, as a result of the lower density/higher free volume are potentially correlated to faster diffusion, where faster polymer chain movement accommodates jump diffusion for penetrant species. Said another way, if fluctuations along the polymer backbone on length scales comparable to monomer/penetrant size, connections to free volume pockets may open and close more rapidly and penetrant molecules spend less time trapped in a single pocket. For other molecular weights, the secondary relaxation times are the same as the neat polymer for temperatures above -90°C. Therefore, the enhanced free volume in these systems still allows for faster diffusion compared to the neat melt, but the side group rotations at least do not hinder transport.

The time scales of the beta process and small penetrant diffusion are more comparable than that of the mechanical rheology, but anomalous transitions at these moderate values of M_n appear to affect the dynamics and behavior across wide length and time scales nonetheless. Clearly the complex structure of these materials leads to complex dynamical responses, which further

manifests in surprising macroscopic properties, potentially rendering these systems valuable in a wide range of applications.

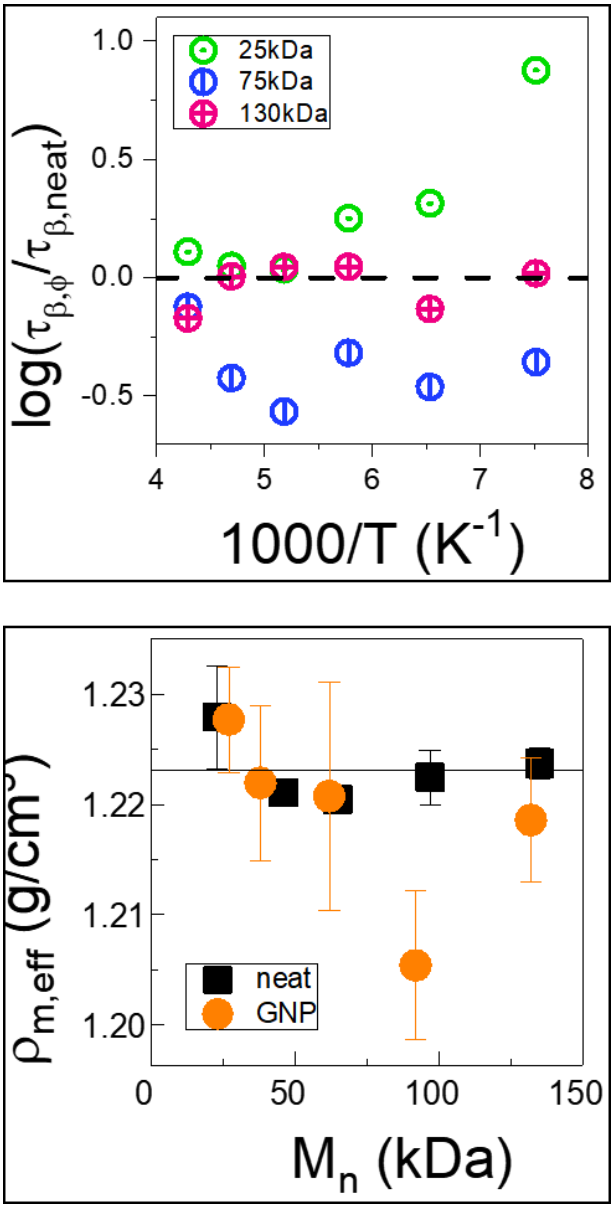

Figure 5.5: Relative secondary relaxation times of GNP systems as a function of reduced temperature (A). Dashed line represents $\tau_{\beta,\phi}/\tau_{\beta,neat}$ =1, *i.e.* where the GNP relaxation time is the same as the neat; effective density of the polymer phase as a function of M_n in neat PMA and GNP systems with σ=0.43chains/nm^2 (B).Solid line is the average density of neat PMA.

Chapter 6

Conclusions and Future Work

In this thesis, we investigate the various properties of matrix-free grafted nanoparticle (GNP) systems, including their applications as selective gas separation membranes, structure, and dynamics. The transport properties of light gases and condensable solvent vapor are systematically studied in matrix-free GNP membranes for various graft density and a wide range of grafted chain molecular weight. Based on these results, we also investigate the free volume of these materials and compare the results to that of neat polymer melts. Second, we investigate the dry-state structure and organization of the nanoparticle cores using small angle X-ray scattering and converted the data to a probability distribution function to analyze the structure in real space. The structure was also studied as a function of solvent content under *in-situ* swelling conditions using contrast variation small angle neutron scattering. Furthermore, we study the dynamics of matrix free GNPs over a broad range of temperatures and time scales. Linear mechanical rheology was used to study relaxation mechanisms ranging from segmental (glassy) relaxation through terminal flow using a combination of small amplitude oscillatory shear and creep flow experiments. We develop a scaling theory to understand how the conformation of a single grafted particle describes the multiple modes of relaxation found for these GNP systems. Next, start-up shear was used to study the non-linear flow behavior of these materials. Finally, faster dynamics such as the segmental and secondary relaxations are studied using broadband dielectric spectroscopy. While nascent, the results presented in this thesis - namely the observed transport enhancement and tunable mechanical behavior- suggest that matrix-free GNPs are an emergent class of materials that have the potential to greatly impact the future design and fabrication of gas separation membranes.

6.1 Polymer-Grafted Nanoparticle Membranes with Controllable Free Volume

The chemical grafting of polymer chains to inorganic NPs is a novel design platform for advanced polymeric membranes. In the matrix-free state, this platform permits precise tuning of gas permeabilities and selectivities through the polymer graft characteristics, both above and below T_g. Surprisingly, the permeability is enhanced non-monotonically relative to the neat polymer melt, with a local maximum in this enhancement at moderate M_n. The absolute value of the permeability increase simply shifts vertically by manipulating the graft density. For small gases, we find up to an order of magnitude enhancement of the permeability, with minor effects on selectivity. The quartz crystal microbalance technique elucidates that the increase in permeability is primarily driven by a significant enhancement in the diffusion coefficient. Multiple experimental probes also show the statistical free volume is directly manipulated by the graft parameters, namely M_n, which leads to the enhancement in small molecule diffusion. This is further supported by molecular dynamics simulations, which suggest that the polymer brush distorts considerably and may lead to lower polymer density in the interstitial spaces. Indeed, experiments also show that at intermediate M_n, the effective polymer density is lower than that of the neat polymer.

While we are as of yet unable to cross the "Robeson Upper Bound", we demonstrate that the enhancement of free volume is not limited to a single polymer chemistry, and works in both rubbery and glassy polymer systems. Importantly, we find no deleterious aging effects in GNP membranes for at least several months, even after aggressive thermal annealing. This work suggests that by combining chemical synthesis of high free volume polymers with physical

constraints of tethering chains to nanoparticle surfaces significantly increases the available handles with which to tune membrane performance.

Furthermore, we have demonstrated that using a quartz crystal microbalance with energy dissipation, we can track in real-time the absorption kinetics to directly calculate the diffusivity and solubility parameters, which are in good agreement with values found by conventional steady-state permeation methods. The use of this method is beneficial in that it is highly accurate and requires significantly fewer constraints on sample preparation. Compared to a conventional permeation cell apparatus, for example, which requires sample masses on the order of grams and completely defect-free membrane preparation, the QCM-D can be used with a few milligrams of sample and is not as sensitive to film preparation. We validate that this method, therefore, may be suitable as a relatively higher throughput technique to quickly screen new polymer membrane candidates, which may further advance the search for high performance gas separation materials. We postulate that using these hybrid structures, the stable manipulation of free volume could lead to rational design of ever better polymer membranes.

6.2 Determining the Structure of Polymer-Grafted Nanoparticle Membranes

We use a combination of microscopy and small angle scattering techniques to study the particle morphology of two graft densities over a range of grafted chain molecular weights. Visually, we confirm from transmission electron microscopy that as in these matrix-free grafted nanoparticle systems, the core particles are well dispersed and no aggregation is occurring for all

graft parameters studied. For fixed graft density, the inter-particle spacing increases with increasing molecular weight. We do not observe any long-range crystal structures, although the micrographs cannot confirm the existence of local ordering. Therefore, we use small angle X-ray scattering combined with a pair distribution function analysis to probe the average structure in the bulk. SAXS experiments confirm the core particles are uniformly well dispersed, and the inter-particle spacing increases with increasing M_n. We find the brush height of a single particle scales as ~$N^{0.7}$, which indicates that the chains are very strongly stretched. Damped sine wave fits to the pair distribution function analysis indicate these samples are completely isotropic and amorphous even at local length scales. Additionally, the morphological changes appear monotonic with respect to molecular weight, thus no obvious explanation for the increased volume found in these materials is found in the dry-state particle organization.

Therefore, using a custom designed sample holder, contrast variation small angle neutron scattering experiments were conducted to study the changes in morphology upon the absorption of a small molecule penetrant. We found no preferential segregation of solvent between the particle cores and instead the solvent uniformly wets the entire brush homogeneously. We conclude the non-monotonic enhancement in permeability and/or free volume most likely does not arise solely from any anisotropy in the core particle morphology of these materials.

6.3 Solid to Liquid Transition of Matrix-Free Polymer Grafted Nanoparticles

The linear viscoelastic response of matrix-free grafted nanoparticle systems for two graft densities and varied M_n was studied over a wide range of temperatures and superimposed to create

a full relaxation master curve. Using creep flow tests, we extend the accessible frequency window to 16 decades and capture relaxations ranging from glassy, segmental motion through terminal flow. For all grafted samples, a significant elongation of the entanglement plateau is observed relative to the neat melt of corresponding molecular weight. The plateau modulus is enhanced relative to the neat polymer; however, the increase is less than that predicted by the Guth-Gold model. At low oscillatory frequency, ω, a second relaxation plateau appears at intermediate M_n, and this plateau becomes more prominent as molecular weight further decreases. Large M_n systems, on the other hand, behave similar to star polymer melts, with no low-ω plateau. Additionally, the terminal flow regime appears at several decades lower frequency than the corresponding neat melts, and this difference increases with decreasing M_n.

We postulate the low-ω plateau relates to a colloidal-type relaxation of the grafted particles as they diffuse via a "cage-hopping" mechanism. This is a result of the brush conformation of an individual grafted particle, which behaves akin to a relatively hard sphere. As a result of grafting long polymer chains to a highly curved surface, the polymer corona is comprised of two distinct conformation regions: a rigid, inner regime where the polymer chains are highly stretched and an outer Gaussian regime. Therefore, we develop a scaling theory to estimate the sizes of these two regimes as a function of molecular weight and graft density. We find good agreement of the estimated brush size with that measured by small angle X-ray scattering. Additionally, the packing fraction of the effective "rigid spheres" increases as molecular weight of the brush decreases and eventually plateaus at ~0.58, commonly otherwise understood as the packing fraction at the glass transition of hard spheres. The transition where the plateau appears occurs at the M_n where the low-ω relaxation processes emerges. Therefore, we conclude the low-ω relaxation is a true colloidal relaxation. We therefore can fit the full master curve using the BoB model for the polymer

arm relaxation and the mode coupling theory to fit the colloidal process. We note that the transition between solid-to-liquid like behavior also occurs in the same M_n window where we observe the largest enhancement of permeability. Although the colloidal relaxation occurs on much longer time scales than small molecule diffusion, we do note that the significantly increased terminal flow relaxation times are possible explanation as to why grafted nanoparticle membranes do not suffer from aging mechanisms compared to neat polymer melts.

Finally, using non-linear start up shear experiments, we show that for systems with intermediate to high M_n, the overall Young's modulus and toughness are increased relative to that of the corresponding neat polymer. However, for small M_n, the grafted nanoparticle systems exhibit brittle fracture at very small strain rates. Therefore, depending on the chain architecture, in addition to enhanced transport properties, grafted nanoparticle constructs may offer additional mechanical reinforcement for polymer membrane systems which must withstand harsh operating environments.

6.4 Segmental and Secondary Relaxations of Matrix-Free Grafted Nanoparticles

Broadband dielectric spectroscopy was used to study the distribution of relaxation times of the segmental and secondary relaxations in grafted polymer nanoparticles, and compared to neat polymer melts of corresponding M_n. For the segmental, or α-relaxation in the composite materials, the dielectric loss is significantly broadened and shifted to lower frequency. These effects become more exaggerated as M_n decreases. We use the inter layer model to fit the segmental relaxation and extract the temperature dependence on the thickness of the interfacial layer where the

segmental mobility close to the surface of the particle is reduced. The thickness of the interfacial layer in the grafted nanoparticle system is smaller compared to that of conventional mixed composites from the literature, yet we only find monotonic changes in behavior with changes in M_n.

However, the secondary relaxations show that for low M_n grafted systems, the β-relaxations of the side group rotations is slower than the neat polymer of a similar molecular weight. At intermediate M_n, the β-relaxation is consistently *faster* over a range of temperatures in the grafted system versus the neat and mixed composites. Finally, for large M_n systems, β-relaxation is relatively unaffected for the composite systems relative to the neat analog. This non-monotonic behavior of the secondary relaxations in matrix-free grafted nanoparticle systems is possibly linked to the lower effective density of the polymer phase detailed in Chapter 2. The apparent increase in free volume of these systems therefore seems accessible only on very small length and time scales. We conclude, therefore, that the rational design of next generation gas separation membranes, or other functional nanocomposite materials require careful characterization on the molecular scale. Clearly the multifaceted structure of these materials leads to complex structure and dynamical responses, which further manifests in surprising macroscopic properties, potentially rendering these systems valuable in a wide range of applications.

6.5 Future Work

Because the work never ends, in this section we detail potential future directions of this project.

6.5.1 Improvements to Grafted Nanoparticle Gas Separation Membranes

The use of grafted nanoparticle constructs significantly increases the parameter space available to improve the performance of polymer membranes for gas separation. Here, we detail a few examples of potential avenues which are as of yet untested in their effect on gas transport properties, although this list is far from exhaustive.

Although we have demonstrated so far that matrix-free grafted nanoparticle constructs show controllable increases to permeability via manipulation of chain architecture for both PMA and PMMA, we still are unable to cross the Robeson upper bound. However, these particular polymers serve merely as a proof of concept, and grafting other, more industrially relevant polymers may allow for membranes which outperform the current state-of-the-art. For example, grafting polymers which are more highly selective or highly permeable may lead to enhancement which breaks the upper bound. A couple classes of polymers which we are currently investigating are those of poly(acetylenes) and poly(acrylonitriles). Other polymers, such as polymers with intrinsic micro-porosity (PIM), have exceptionally high permeability, but due to aging, the permeability is dramatically reduced in a few hours.[117] The concept of grafting may be useful to extend the lifetime of these materials or even current commercially available polymer membranes, as we have demonstrated that these nanocomposites significantly slow the process of aging.

In addition to chemical variations of the grafted brush, other parameters of the filler cores are yet to be investigated. One particular area of interest may be investigating the role of polydispersity of the nanoparticle cores. Recent work by Bachhar and coworkers[118] has shown that polydispersity may significantly hinder crystalline self-assembly. As the silica nanoparticles used in these studies are considerably polydisperse, this may explain why we do not observe any

anisotropy, even on local length scales. It is not obvious, however, if long-range crystalline order would improve or deteriorate diffusion of small molecules. One the one hand, MD simulations predicted that in crystalline systems, areas of local polymer density are located in the interstitial spaces between particles. Perhaps if these "pockets" are aligned to create roughly percolated systems, the diffusion enhancement might increase further. However, local frustration due to inefficient particle packing and organization may explain why the free volume is so significantly increased in these materials in the first place. Therefore, creating more monodisperse and potentially more ordered systems may or may not further improve the permeability.

Additionally, varying the size and/or shape of the nanoparticle core may change the inter-particle morphology or conformation of the grafted corona. On-going theoretical work within the Kumar group show, for example, that grafting from cubic particle cores leads to anisotropic corona shapes, which in turn changes the crystalline unit cell lattice type. These variations in structure both between multiple particles and within the brush of a single particle may lead to changes in the fractional free volume, leading to different effects on the permeability of small molecules. Additionally, changing the chemical composition of the cores from an inert material to one that may play an active role in gas separation, such as a zeolite material, could help to improve the selectivity in these materials. Furthermore, changes to the core geometry and chemical composition may improve the mechanical reinforcement. In order to design next generation membrane materials, then, the effects of multiple parameters must be better understood, which is an ongoing focus of this project.

6.5.2 Free-Volume Distribution in the Presence of High Molecular Weight Solvents of Grafted Nanoparticle Materials

Preliminary results show that the addition of small amounts of free matrix chains to a membrane of polymer grafted nanoparticles of similar M_n results in a non-monotonic effect on the selectivity between CO_2 and CH_4. Although the permeability drops systematically as the weight fraction of added matrix chains, ω_{free}, it appears as though the degree to which permeability is affected is dependent on the size of a given penetrant (Figure 6.1A). Because the permeability for the larger CH_4 molecules decreases much more rapidly, at low loadings of free polymer, there is a large increase in selectivity of CO_2 (Figure 7.1B). Eventually at high loadings, the permeability and selectivity approaches that of the neat polymer, thus the effects imposed by the grafted particles is completely erased. We postulate that because the size of the free chains is comparable to that of the tethered chains, the free polymers cannot wet the brush and are forced to segregate

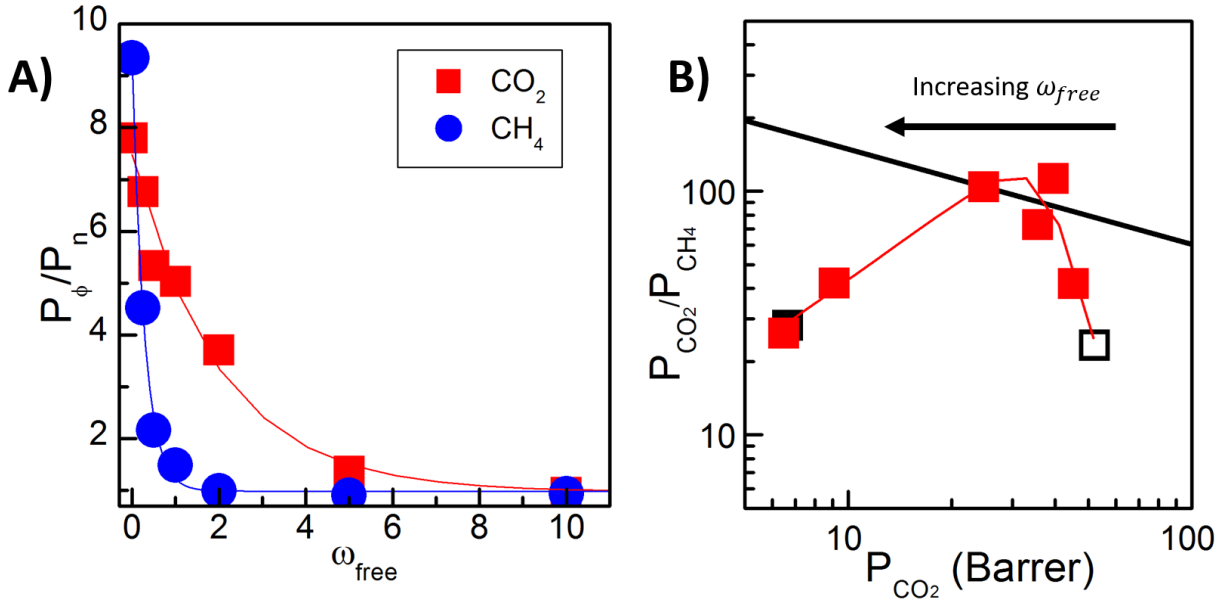

Figure 6.1: Effects of additional free polymer chains on small gas permeability and selectivity

on the outside of the grafted corona. Although we showed in Chapter 3 that small molecule solvents wet the brush homogeneously, the addition of free polymers significantly restricts the available free volume on the outside of the grafted corona. In the limit where the decrease in free volume is only enough to significantly restrict the diffusion of the larger CH_4 molecules, the selectivity of CO_2 rapidly increases. Eventually, the added free chains also reduce the available free volume such that the permeability also decreases sharply for CO_2.

Therefore, if the free chains are restricted to outside the brush, we should be able to detect this using contrast variation small angle neutron scattering. If a "high molecular weight" solvent such as a polymer chain cannot penetrate the grafted brush it should instead preferentially segregate in the interstitial spaces between the particles. This would validate the hypothesis that there is an average reduction in polymer density between particle cores in matrix-free systems. Understanding the origins of the penetrant size dependence in films with added free polymer will aid in the rational design of next generation gas separation membranes. This is therefore an ongoing focus in the study of the structure of these hierarchical grafted nanoparticle materials.

6.5.3 Dynamics of Matrix-Free Grafted Nanoparticles

Broadband dielectric spectroscopy has shown that the secondary β-relaxations show a non-monotonic trend in relaxation time as a function of M_n. For intermediate M_n, where we also observe the highest enhancement in permeability as well as a transition in the long-time flow dynamics, the secondary relaxations are consistently faster than that of the corresponding neat polymer. In order to better determine specific length and time scales at which the dynamics of the grafted system surpass those of the neat polymer, we propose to use quasi-elastic neutron

scattering, specifically neutron backscattering. Preliminary mean squared displacement, $\langle u^2 \rangle$, as a function of temperature from backscattering fixed window scans of matrix-free PMA-g-SiO_2 samples of two molecular weights and fixed graft density compared to neat PMA of corresponding molecular weight are plotted in Figure 6.2.

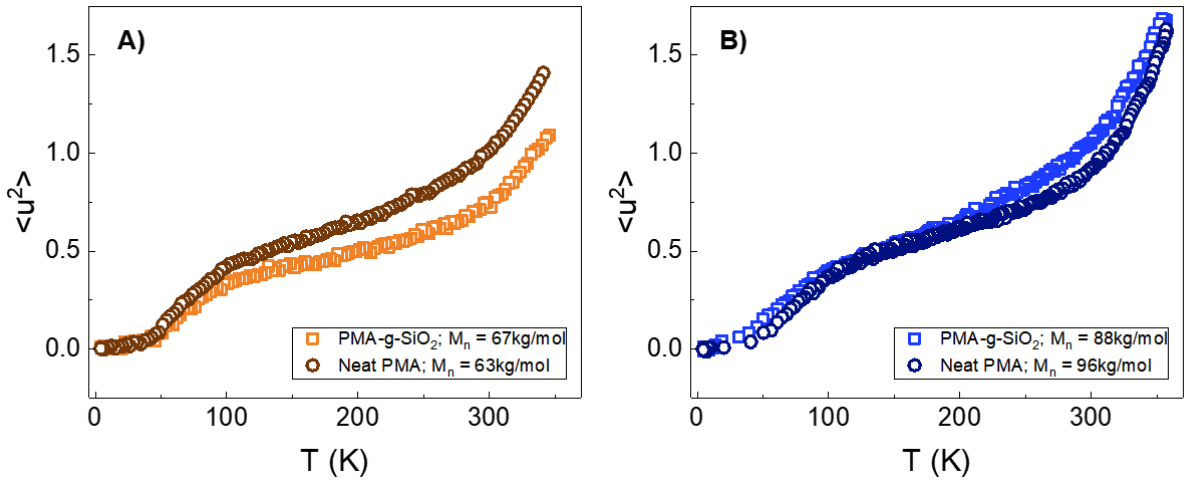

Figure 6.2: Mean-squared displacement as a function of temperature of matrix-free grafted nanoparticle materials at σ=0.47chains/nm^2 (squares) compared to neat PMA (circles) for average molecular weight A) ~65kg/mol and B) ~90kg/mol

For grafted nanoparticle systems below the maxima/transitions found from other studies detailed in this dissertation, the dynamics are systematically slower than that of the neat polymer of comparable molecular weight. However, in the range where we see faster secondary dynamics, the mean squared displacement of the grafted system is higher for the grafted nanoparticle sample, indicating the mobility of these systems is increased. The dependence on sample preparation as well as the accessible temperature range is preferential for neutron backscattering versus dielectric spectroscopy. Therefore, we propose to use backscattering to study the dynamics of a wide range of M_n. It still remains unclear if the remarkable small molecule transport in grafted nanoparticle materials is a result of the polymer chain dynamics, or the dynamics are merely another proxy with which to understand the origins and effects of increased free volume within these systems.

However, because quasi-elastic neutron scattering allows us to obtain explicit information on the time *and* length scales of dynamic processes, this will be a powerful tool in answering this question and ultimately designing new materials with high free volume.

FIN

References

1. Goel, V. *et al.* Structure of Polymer Tethered Highly Grafted Nanoparticles. *Macromolecules* **44,** 8129–8135 (2011).

2. Kumar, S. K., Benicewicz, B. C., Vaia, R. A. & Winey, K. I. 50th Anniversary Perspective: Are Polymer Nanocomposites Practical for Applications? *Macromolecules* **50,** 714–731 (2017).

3. Akcora, P. *et al.* Anisotropic self-assembly of spherical polymer-grafted nanoparticles. *Nat. Mater.* **8,** 354–359 (2009).

4. Bilchak, C. R. *et al.* Polymer-Grafted Nanoparticle Membranes with Controllable Free Volume. *Macromolecules* **50,** 7111–7120 (2017).

5. U.S. Energy Information Administration. *Annual Energy Outlook 2018 with projections to 2050*. (2018). doi:DOE/EIA-0383(2017)

6. Keith, A. & Peter, E. Compositional variety complicates processing plans for US shale gas Reproduced with permission of the copyright owner . Further reproduction prohibited without permission . (2009).

7. National Transportation Safety Board. Pipeline Accident Report: Natural Gas Pipeline Rupture and Fire Near Carlsbad , New Mexico. 1–57 (2003).

8. Energy Information Administration. Natural Gas Processing : The Crucial Link Between Natural Gas Production and Its Transportation to Market. 11 (2006).

9. Robeson, L. M. The upper bound revisited. *J. Memb. Sci.* **320,** 390–400 (2008).

10. Lin, H. & Freeman, B. D. Materials selection guidelines for membranes that remove CO2 from gas mixtures. *J. Mol. Struct.* **739,** 57–74 (2005).

11. Freeman, B. D. Basis of Permeability/Selectivity Tradeoff Relations in Polymeric Gas Separation Membranes. *Macromolecules* **32,** 375–380 (1999).

12. Robeson, L. M. Correlation of separation factor versus permeability for polymeric membranes. *J. Memb. Sci.* **62,** 165–185 (1991).

13. Baker, R. W. & Low, B. T. Gas separation membrane materials: A perspective. *Macromolecules* **47,** 6999–7013 (2014).

14. Robeson, L. M., Liu, Q., Freeman, B. D. & Paul, D. R. Comparison of transport properties of rubbery and glassy polymers and the relevance to the upper bound relationship. *J. Memb. Sci.* **476,** 421–431 (2015).

15. Robeson, L. M., Burgoyne, W. F., Langsam, M., Savoca, a. C. & Tien, C. F. High performance polymers for membrane separation. *Polymer (Guildf).* **35,** 4970–4978 (1994).

16. Powell, C. E. & Qiao, G. G. Polymeric CO2/N2 gas separation membranes for the capture of carbon dioxide from power plant flue gases. *J. Memb. Sci.* **279,** 1–49 (2006).

17. Sridhar, S., Smitha, B. & Aminabhavi, T. M. Separation of Carbon Dioxide from Natural Gas Mixtures through Polymeric Membranes—A Review. *Sep. Purif. Rev.* **36,** 113–174 (2007).

18. Kelman, S., Lin, H., Sanders, E. S. & Freeman, B. D. CO2/C2H6 separation using solubility selective membranes. *J. Memb. Sci.* **305,** 57–68 (2007).

19. Ramesh, N., Davis, P. K., Zielinski, J. M., Danner, R. P. & Duda, J. L. Application of free-volume theory to self diffusion of solvents in polymers below the glass transition temperature: A review. *Journal of Polymer Science, Part B: Polymer Physics* **49,** 1629–1644 (2011).

20. Vrentas, J. S. & Duda, J. L. Diffusion in polymer—solvent systems. I. Reexamination of the free-volume theory. *J. Polym. Sci. Polym. Phys. Ed.* **15,** 403–416 (1977).

21. Cohen, M. H. & Turnbull, D. Molecular Transport in Liquids and Glasses. *J. Chem. Phys.* **31,** 1164–1169 (1959).

22. Fujita, H. Diffusion in polymer-diluent systems. *Fortschritte der Hochpolym.* **3,** 1–47 (1961).

23. Park, J. & Paul, D. R. Correlation and Prediction of gas permeability in glassy polymer membrane materials via a modified free volume based group contribution method. *J. Memb. Sci.* **125,** 23–39 (1997).

24. Baker, R. W. & Lokhandwala, K. Natural gas processing with membranes: An overview. *Industrial and Engineering Chemistry Research* **47,** 2109–2121 (2008).

25. Huang, Y. & Paul, D. R. Physical aging of thin glassy polymer films monitored by gas permeability. *Polymer (Guildf).* **45,** 8377–8393 (2004).

26. Huang, Y. & Paul, D. R. Effect of temperature on physical aging of thin glassy polymer films. *Macromolecules* **38,** 10148–10154 (2005).

27. Huang, Y., Wang, X. & Paul, D. R. Physical aging of thin glassy polymer films: Free volume interpretation. *J. Memb. Sci.* **277,** 219–229 (2006).

28. Rowe, B. W., Freeman, B. D. & Paul, D. R. Physical aging of ultrathin glassy polymer films tracked by gas permeability. *Polymer (Guildf).* **50,** 5565–5575 (2009).

29. Consolati, G., Genco, I., Pegoraro, M. & Zanderighi, L. Positron Annihilation lifetime (PAL) in Poly [1-(trimethylsilyl) propine] (PTMSP): Free Volume Determination and Time Dependence of Permeability. *J. Polym. Sci. Part B Polym. Phys.* **34,** 357–367 (1996).

30. Maillard, D. *et al.* Mechanical properties of thin glassy polymer films filled with spherical polymer-grafted nanoparticles. *Nano Lett.* **12,** 3909–3914 (2012).

31. Rittigstein, P. & Torkelson, J. M. Polymer-nanoparticle interfacial interactions in polymer nanocomposites: Confinement effects on glass transition temperature and suppression of physical aging. *J. Polym. Sci. Part B Polym. Phys.* **44,** 2935–2943 (2006).

32. Rittigstein, P., Priestley, R. D., Broadbelt, L. J. & Torkelson, J. M. Model polymer nanocomposites provide an understanding of confinement effects in real nanocomposites.

Nat. Mater. **6,** 278–282 (2007).

33. Merkel, T. C. *et al.* Ultrapermeable, reverse-selective nanocomposite membranes. *Science (80-.).* **296,** 519–522 (2002).

34. Merkel, T. C. *et al.* Effect of nanoparticles on gas sorption and transport in poly(1-trimethylsilyl-1-propyne). *Macromolecules* **36,** 6844–6855 (2003).

35. Merkel, T. C. *et al.* Sorption, transport, and structural evidence for enhanced free volume in poly (4-methyl-2-pentyne)/fumed silica nanocomposite membranes. *Chem. Mater.* **15,** 109–123 (2003).

36. Crank, J. The mathematics of diffusion. *Oxford Univ. Press* 414 (1975). doi:10.1016/0306-4549(77)90072-X

37. Hill, R. J. Reverse-selective diffusion in nanocomposite membranes. *Phys. Rev. Lett.* **96,** (2006).

38. Takahashi, S. & Paul, D. R. Gas permeation in poly(ether imide) nanocomposite membranes based on surface-treated silica. Part 1: Without chemical coupling to matrix. *Polymer (Guildf).* **47,** 7519–7534 (2006).

39. Hoang, D. T. *et al.* In situ multi-modal monitoring of solvent vapor swelling in polymer thin films. *Rev. Sci. Instrum.* **87,** (2016).

40. Janes, D. W., Moll, J. F., Harton, S. E. & Durning, C. J. Dispersion Morphology of Poly (methyl acrylate)/ Silica Nanocomposites. *Small* 4920–4927 (2011). doi:10.1021/ma200205j

41. Goyal, S. & Escobedo, F. a. Structure and transport properties of polymer grafted nanoparticles. *J. Chem. Phys.* **135,** 184902 (2011).

42. Fernandes, N. J., Koerner, H., Giannelis, E. P. & Vaia, R. a. Hairy nanoparticle assemblies as one-component functional polymer nanocomposites: opportunities and challenges. *MRS Commun.* **3,** 13–29 (2013).

43. Koerner, H., Drummy, L. F., Benicewicz, B., Li, Y. & Vaia, R. A. Nonisotropic Self-Organization of Single-Component Hairy Nanoparticle Assemblies. (2013).

44. Srivastava, S., Choudhury, S., Agrawal, A. & Archer, L. A. Self-suspended polymer grafted nanoparticles. *Curr. Opin. Chem. Eng.* **16,** 92–101 (2017).

45. Choudhury, S., Agrawal, A., Kim, S. A. & Archer, L. A. Self-Suspended Suspensions of Covalently Grafted Hairy Nanoparticles. *Langmuir* **31,** 3222–3231 (2015).

46. Kremer, F. & Schönhals, A. *Broadband Dielectric Spectroscopy. Springer: Berlin* (2003). doi:10.1007/978-3-642-56120-7

47. Rubinstein, M. & Colby, R. H. Polymer physics. *Polymer International* 440 (2003). doi:10.1002/pi.1472

48. Williams, M. L., Landel, R. F. & Ferry, J. D. The Temperature Dependence of Relaxation Mechanisms in Amorphous Polymers and Other Glass-forming Liquids. *J. Am. Chem. Soc.*

77, 3701–3707 (1955).

49. Adam, G. & Gibbs, J. H. On the temperature dependence of cooperative relaxation properties in glass-forming liquids. *J. Chem. Phys.* **43,** 139–146 (1965).

50. Edwards, S. & Edwards, S. F. The statistical mechanics of polymerized material Recent citations The statistical mechanics of polymerized material. *Proc. Phys. Soc.* (1928).

51. McLeish, T. C. B. Tube theory of entangled polymer dynamics. *Adv. Phys.* **51,** 1379–1527 (2002).

52. Rouse Jr, P. E. A theory of the linear viscoelastic properties of dilute solutions of coiling polymers. *J. Chem. Phys.* (1953).

53. Putz, M., Kremer, K. & Grest, G. S. What is the entanglement length in a polymer melt? *Europhys. Lett.* **49,** 735–741 (2000).

54. Kaufman, S., Slichter, W. P. & Davis, D. D. Nuclear Magnetic Resonance Study of Rubber-Carbon Black Interactions. *J. Polym. Sci. Part A-2* **9,** 829–839 (1971).

55. Gong, S., Chen, Q., Moll, J. F., Kumar, S. K. & Colby, R. H. Segmental dynamics of polymer melts with spherical nanoparticles. *ACS Macro Lett.* **3,** 773–777 (2014).

56. Alexandris, S., Sakellariou, G., Steinhart, M. & Floudas, G. Dynamics of unentangled cis -1,4-polyisoprene confined to nanoporous alumina. *Macromolecules* **47,** 3895–3900 (2014).

57. Cheng, S. *et al.* Unexpected Molecular Weight Effect in Polymer Nanocomposites. *Phys. Rev. Lett.* **116,** (2016).

58. Holt, A. P. *et al.* Controlling Interfacial Dynamics: Covalent Bonding versus Physical Adsorption in Polymer Nanocomposites. *ACS Nano* **10,** 6843–6852 (2016).

59. Cheng, S. *et al.* Focus: Structure and dynamics of the interfacial layer in polymer nanocomposites with attractive interactions. *J. Chem. Phys.* **146,** 203201 (2017).

60. Agarwal, P., Kim, S. A. & Archer, L. A. Crowded, confined, and frustrated: Dynamics of molecules tethered to nanoparticles. *Phys. Rev. Lett.* **109,** 1–4 (2012).

61. Kim, S. A., Mangal, R. & Archer, L. A. Relaxation Dynamics of Nanoparticle-Tethered Polymer Chains. *Macromolecules* **48,** 6280–6293 (2015).

62. Pakula, T., Vlassopoulos, D., Fytas, G. & Roovers, J. Structure and dynamics of melts of multiarm polymer stars. *Macromolecules* **31,** 8931–8940 (1998).

63. Vlassopoulos, D., Fytas, G., Pakula, T. & Roovers, J. Multiarm star polymers dynamics. *J. Phys. Condens. Matter* **13,** (2001).

64. Kapnistos, M., Semenov, A. N., Vlassopoulos, D. & Roovers, J. Viscoelastic response of hyperstar polymers in the linear regime. *J. Chem. Phys.* **111,** 1753–1759 (1999).

65. Helgeson, M. E., Wagner, N. J. & Vlassopoulos, D. Viscoelasticity and shear melting of colloidal star polymer glasses. *J. Rheol. (N. Y. N. Y).* **51,** 297–316 (2007).

66. Lodge, T. P. Block copolymers: Past successes and future challenges. *Macromolecular*

Chemistry and Physics **204,** 265–273 (2003).

67. Bockstaller, M. R. & Thomas, E. L. Optical Properties of Polymer-Based Photonic Nanocomposite Materials. *J. Phys. Chem. B* **107,** 10017–10024 (2003).

68. Voudouris, P. *et al.* Anisotropic elasticity of quasi-one-component polymer nanocomposites. in *ACS Nano* **5,** 5746–5754 (2011).

69. Barbey, R. *et al.* Polymer brushes via surface-initiated controlled radical polymerization: synthesis, characterization, properties, and applications. *Chem. Rev.* **109,** 5437–5527 (2009).

70. Li, C., Han, J., Ryu, C. Y. & Benicewicz, B. C. A versatile method to prepare RAFT agent anchored substrates and the preparation of PMMA grafted-nanoparticles. *Macromolecules* **39,** 3175–3183 (2006).

71. Minelli, M. *et al.* Oxygen permeability of novel organic-inorganic coatings: I. Effects of organic-inorganic ratio and molecular weight of the organic component. *Eur. Polym. J.* **44,** 2581–2588 (2008).

72. Chiou, J. S., Barlow, J. W. & Paul, D. R. Sorption and transport of gases in miscible poly(methyl acrylate)/poly(epichlorohydrin) blends. *J. Appl. Polym. Sci.* **30,** 1173–1186 (1985).

73. Robeson, L. M. Correlation of separation factor versus permeability for polymeric membranes. *J. Memb. Sci.* **62,** 165–185 (1991).

74. Janes, D. W. & Durning, C. J. Sorption and Di ff usion of n - Alkyl Acetates in Poly (methyl acrylate)/ Silica Nanocomposites. (2013).

75. Janes, D. W., Bilchak, C. & Durning, C. J. Decoupling energetic modifications to diffusion from free volume in polymer/nanoparticle composites. *Soft Matter* **13,** 677–685 (2017).

76. Shelley, S. Capturing CO 2: Membrane systems move forward. *Chem. Eng. Prog.* **105,** 42–47 (2009).

77. Zhao, Y. H., Abraham, M. H. & Zissimos, A. M. Fast Calculation of van der Waals Volume as a Sum of Atomic and Bond Contributions and Its Application to Drug Compounds. *J. Org. Chem.* **68,** 7368–7373 (2003).

78. Hansen, J. & Verlet, L. Phase transition of the Lennard-Jones system. *Physical Review A* **184,** 151–161 (1969).

79. Egami, Takeshi, Billinge, S. *Underneath the Bragg peaks: Structural analysis of complex materials*. (Elsevier Ltd, 2012).

80. Billinge, S. J. L. & Kanatzidis, M. G. Beyond crystallography: the study of disorder, nanocrystallinity and crystallographically challenged materials with pair distribution functions. *Chem. Commun.* 749 (2004). doi:10.1039/b309577k

81. Juhás, P., Davis, T., Farrow, C. L. & Billinge, S. J. L. PDFgetX3: A rapid and highly automatable program for processing powder diffraction data into total scattering pair distribution functions. *J. Appl. Crystallogr.* **46,** 560–566 (2013).

82. Dukes, D. *et al.* Conformational transitions of spherical polymer brushes: Synthesis, characterization, and theory. *Macromolecules* **43,** 1564–1570 (2010).

83. Fujita, H., Kishimoto, A. & Matusmoto, K. Concentration and temperature dependence of diffusion coefficients for systems polymethyl acrylate and n-akyl acetates. *Trans. Faraday Soc.* 424–437 (1959).

84. Fetters, L. J., Lohse, D. J., Richter, D., Witten, T. A. & Zirkel, A. Connection between Polymer Molecular Weight, Density, Chain Dimensions, and Melt Viscoelastic Properties. *Macromolecules* **27,** 4639–4647 (1994).

85. Zaccarelli, E. *et al.* Crystallization of hard-sphere glasses. *Phys. Rev. Lett.* **103,** 1–4 (2009).

86. van Gurp, M. & Palmen, J. Time-temperature superposition for polymeric blends. *J Rheol Bull* **65,** 5–8 (1998).

87. Nielson, L. & Landel, R. F. *Mechanical Properties of Polymers and Composites*. (Marcel Dekker, Inc, 1994).

88. Weese, J. A regularization method for nonlinear ill-posed problems. *Comput. Phys. Commun.* **77,** 429–440 (1993).

89. Meissner, J., Garbella, R. W. & Hostettler, J. Measuring Normal Stress Differences in Polymer Melt Shear Flow. *J. Rheol. (N. Y. N. Y).* **33,** 843 (1989).

90. Schweizer, T. Measurement of the first and second normal stress differences in a polystyrene melt with a cone and partitioned plate tool. *Rheol. Acta* **41,** 337–344 (2002).

91. Schweizer, T. Comparing cone-partitioned plate and cone-standard plate shear rheometry of a polystyrene melt. *J. Rheol. (N. Y. N. Y).* **47,** 1071 (2003).

92. Schweizer, T., van Meerveld, J. & Öttinger, H. C. Nonlinear shear rheology of polystyrene melt with narrow molecular weight distribution—Experiment and theory. *J. Rheol. (N. Y. N. Y).* **48,** 1345 (2004).

93. Li, X. & Wang, S. Q. Elastic yielding after step shear and during LAOS in the absence of meniscus failure. *Rheol. Acta* **49,** 985–991 (2010).

94. Doi, M. Explanation for the 3.4-power law for viscosity of polymeric liquids on the basis of the tube model. *J. Polym. Sci. Polym. Phys. Ed.* **21,** 667–684 (1983).

95. Fox, T. G. & Loshaek, S. Isothermal viscosity-molecular weight dependence for long polymer chains. *J. Appl. Phys.* **26,** 1080–1082 (1955).

96. Zhou, Q. & Larson, R. G. Direct molecular dynamics simulation of branch point motion in asymmetric star polymer melts. *Macromolecules* **40,** 3443–3449 (2007).

97. Kirkwood, K. M., Gary Leal, L., Vlassopoulos, D., Driva, P. & Hadjichristidis, N. Stress relaxation of comb polymers with short branches. *Macromolecules* **42,** 9592–9608 (2009).

98. Guth, E. Theory of filler reinforcement. *J. Appl. Phys.* **16,** 20–25 (1945).

99. Ohno, K., Morinaga, T., Takeno, S., Tsujii, Y. & Fukuda, T. Suspensions of silica particles grafted with concentrated polymer brush: A new family of colloidal crystals.

Macromolecules **39,** 1245–1249 (2006).

100. Morinaga, T., Ohno, K., Tsujii, Y. & Fukuda, T. Structural analysis of 'semisoft' colloidal crystals by confocal laser scanning microscopy. *Macromolecules* **41,** 3620–3626 (2008).

101. Pusey, P. N. & Van Megen, W. Phase behaviour of concentrated suspensions of nearly hard colloidal spheres. *Nature* **320,** 340–342 (1986).

102. Das, C., Inkson, N. J., Read, D. J., Kelmanson, M. A. & McLeish, T. C. B. Computational linear rheology of general branch-on-branch polymers. *J. Rheol. (N. Y. N. Y).* **50,** 207–234 (2006).

103. Mason, T. G. & Weitz, D. A. Optical measurements of frequency-dependent linear viscoelastic moduli of complex fluids. *Phys. Rev. Lett.* **74,** 1250–1253 (1995).

104. Lionberger, R. A. & Russel, W. B. High frequency modulus of hard sphere colloids. *J. Rheol. (N. Y. N. Y).* **38,** 1885–1908 (1994).

105. Crassous, J. J., Régisser, R., Ballauff, M. & Willenbacher, N. Characterization of the viscoelastic behavior of complex fluids using the piezoelastic axial vibrator. *J. Rheol. (N. Y. N. Y).* **49,** 851–863 (2005).

106. Crassous, J. J. *et al.* Shear stresses of colloidal dispersions at the glass transition in equilibrium and in flow. *J. Chem. Phys.* **128,** (2008).

107. Siebenbürger, M., Fuchs, M., Winter, H. & Ballauff, M. Viscoelasticity and shear flow of concentrated, noncrystallizing colloidal suspensions: Comparison with mode-coupling theory. *J. Rheol. (N. Y. N. Y).* **53,** 707–726 (2009).

108. Snijkers, F., Ratkanthwar, K., Vlassopoulos, D. & Hadjichristidis, N. Viscoelasticity, nonlinear shear start-up, and relaxation of entangled star polymers. *Macromolecules* **46,** 5702–5713 (2013).

109. Cox, W. P. & Merz, E. H. Correlation of dynamic and steady-flow viscosities. *J. Polym. Sci.* **28,** 619–622 (1958).

110. Moll, J. F. *et al.* Mechanical reinforcement in polymer melts filled with polymer grafted nanoparticles. *Macromolecules* **44,** 7473–7477 (2011).

111. Carroll, B., Cheng, S. & Sokolov, A. P. Analyzing the Interfacial Layer Properties in Polymer Nanocomposites by Broadband Dielectric Spectroscopy. *Macromolecules* **50,** 6149–6163 (2017).

112. Cheng, S. *et al.* Revealing spatially heterogeneous relaxation in a model nanocomposite. *J. Chem. Phys.* **143,** (2015).

113. Hong, L., Gujrati, P. D., Novikov, V. N. & Sokolov, A. P. Molecular cooperativity in the dynamics of glass-forming systems: A new insight. *J. Chem. Phys.* **131,** (2009).

114. Stevenson, J. D. & Wolynes, P. G. On the surface of glasses. *J. Chem. Phys.* **129,** (2008).

115. Hanakata, P. Z., Douglas, J. F. & Starr, F. W. Interfacial mobility scale determines the scale of collective motion and relaxation rate in polymer films. *Nat. Commun.* **5,** 4163 (2014).

116. Cheng, S. *et al.* Interfacial Properties of Polymer Nanocomposites: Role of Chain Rigidity and Dynamic Heterogeneity Length Scale. *Macromolecules* **50,** 2397–2406 (2017).

117. McKeown, N. B. & Budd, P. M. Polymers of intrinsic microporosity (PIMs): organic materials for membrane separations, heterogeneous catalysis and hydrogen storage. *Chem. Soc. Rev.* **35,** 675 (2006).

118. Bachhar, N. *et al.* Impact of the Distributions of Core Size and Grafting Density on the Self-Assembly of Polymer Grafted Nanoparticles. *Macromolecules* **50,** 7730–7738 (2017).

119. Sauerbrey, G. The use of quartz oscillators for weighing thin layers and for microweighing. *Zeitschrift fuer Phys.* **155,** 206–222 (1959).

120. Reviakine, I., Johannsmann, D. & Richter, R. P. Hearing what you cannot see and visualizing what you hear: Interpreting quartz crystal microbalance data from solvated interfaces. *Anal. Chem.* **83,** 8838–8848 (2011).

121. Gidley, D. W., Peng, H.-G. & Vallery, R. S. POSITRON ANNIHILATION AS A METHOD TO CHARACTERIZE POROUS MATERIALS. *Annu. Rev. Mater. Res.* **36,** 49–79 (2006).

122. Brunauer, S., Emmett, P. H. & Teller, E. Adsorption of Gases in Multimolecular Layers. *J. Am. Chem. Soc.* **60,** 309–319 (1938).

123. Joyner, L. G., Barrett, E. P. & Skold, R. The Determination of Pore Volume and Area Distributions in Porous Substances. II. Comparison between Nitrogen Isotherm and Mercury Porosimeter Methods. *J. Am. Chem. Soc.* **73,** 3155–3158 (1951).

124. Metin, B. & Blum, F. D. Molecular mass and dynamics of poly(methyl acrylate) in the glass-transition region. *J. Chem. Phys.* (2006). doi:10.1063/1.2162879

125. Jones, R., Kumar, S., Ho, D., Briber, R. & Russell, T. Chain conformation in ultrathin polymer films. *Nature* **400,** 146–149 (1999).

126. Shelton, C. K. & Epps, T. H. Block copolymer thin films: Characterizing nanostructure evolution with in situ X-ray and neutron scattering. *Polym. (United Kingdom)* **105,** 545–561 (2016).

127. Shelton, C. K., Jones, R. L., Dura, J. A. & Epps, T. H. Tracking Solvent Distribution in Block Polymer Thin Films during Solvent Vapor Annealing with in Situ Neutron Scattering. *Macromolecules* **49,** 7525–7534 (2016).

128. Janes, D. W., Kim, J. S. & Durning, C. J. Interval sorption of alkyl acetates and benzenes in poly(methyl acrylate). *Ind. Eng. Chem. Res.* **52,** 8765–8773 (2013).

Appendix A – Experimental Methods

A.1 Synthesis of Grafted Nanoparticles

A visualization of the synthetic scheme of the surface initiate reversible addition-fragmentation chain transfer polymerization from the surface of silica nanoparticles is shown in Figure A- 1. DoPAT (1.75g, 5mmol) and 2-mercaptothiazoline (0.596 g, 5 mmol) were dissolved in 20mL dry CH_2Cl_2. (Dimethylamino)pyridine (DMAP) (61 mg, 0.50 mmol) was added slowly to the solution. After stirring for 10min at 0°C, dicyclohexylcarbodiimide (DCC) (1.24 g, 6.00 mmol) in 10mL CH_2Cl_2 was added to the solution and stirred at room temperature for 1 hour. After the reaction, the salt was removed by filtration. The solvent was evaporated by vacuum and followed by silica gel column chromatography (5:1 mixture of hexane and ethyl acetate) to get activated DoPAT as yellow oil (2.10g, 93% yield). ^{13}C NMR (75MHz, $CDCl_3$) δ (ppm): 222.80, 201.22, 173.25, 56.41, 48.73, 37.52, 31.93, 29.64, 29.56, 29.45, 29.36, 29.10, 28.97, 28.92, 27.91, 22.71, 16.44, 14.15 (Figure A- 2). ^1H NMR (300 MHz, $CDCl_3$) δ (ppm): 6.46 (q, 1H, J =7.1 Hz), 4.62-4.70 (m, 1 H), 4.42-4.52 (m, 1H), 3.38-3.48 (m, 1H), 3.21-3.34 (m, 3H), 1.51-1.75 (m, 5 H), 1.25-1.42 (m, 18 H), 0.88 (t, 3H, J =7.0 Hz) (Figure A- 3). Elemental Analysis: calculated for $C_{19}H_{33}NOS_5$: C, 50.51; H, 7.36; N, 3.10; S, 35.48; found C, 51.31; H, 7.36; N, 3.20; S, 34.46.

Silica nanoparticles (50.0g, 30 wt% in MEK solution) were added to a round bottom flask with 150 mL THF and 3.0 mL 3-aminopropyldimethylethoxysilane. After purging with N_2 for 30min, the solution was refluxed at 75 °C for 5 hours. The solution was then cooled to room temperature and precipitated into large amount of hexane. The amine functional silica nanoparticles were recovered by centrifuge at 5000 rpm for 5 minutes. The dispersion-precipitation process was then repeated two more times. The silica nanoparticles were then dispersed in 150mL

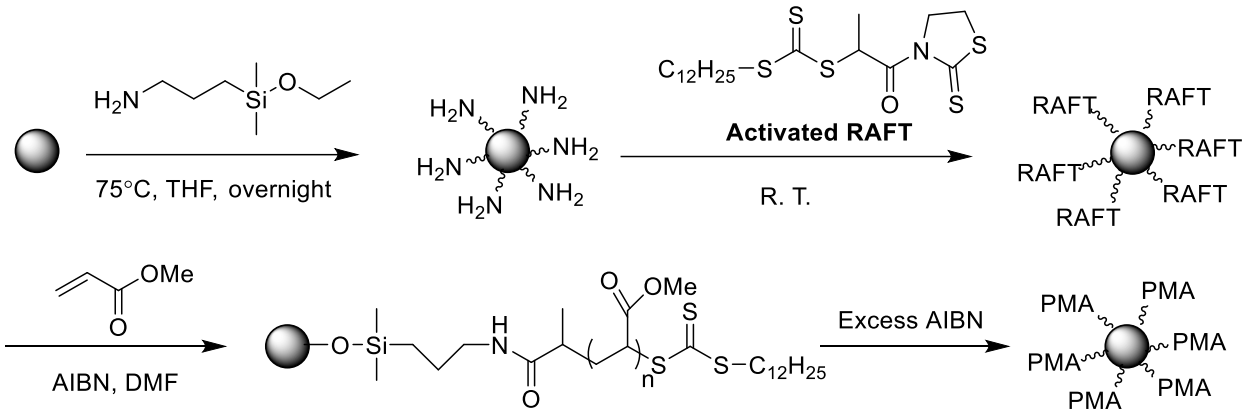

Figure A- 1: Synthetic mechanism of SI-RAFT polymer grafted nanoparticles

dry THF and added to 1.25g activated DoPAT THF (3mL) solution. The solution was stirred overnight and precipitated into a large amount of methanol and re-dispersed in THF. This dispersion-precipitation process was repeated until the supernatant solution was colorless. The nanoparticles were placed in a room temperature vacuum oven to dry. The grafted density of DoPAT-NP was determined with TGA.

A typical example of the polymerization method is described here: DoPAT-NP (0.35g, σ=0.43 chains/nm^2) was dispersed in 14mL DMF and 7.37mL methyl acrylate (0.081 mol). AIBN, dissolved in DMF (0.356mL, 0.01M), was added to the solution, and finally the mixture was transferred into a dried Schlenk flask. (The methymethacrylate polymerization followed the literature.[70]) The mixture was degassed by three freeze- pump- thaw cycles, backfilled with nitrogen, and then placed in an oil bath at 60 °C. The polymerization solution was quenched in ice water after 2.25 hours. THF (20mL) was added to the flask and the solution was poured into hexanes (120mL) to precipitate PMA-grafted nanoparticles. The PMA-grafted silica nanoparticles were recovered by centrifuge at 3000 rpm for 10 min. The nanoparticles were dispersed in 50mL THF and precipitated in 100ml methanol. This dispersion-precipitation process was repeated for another five times.

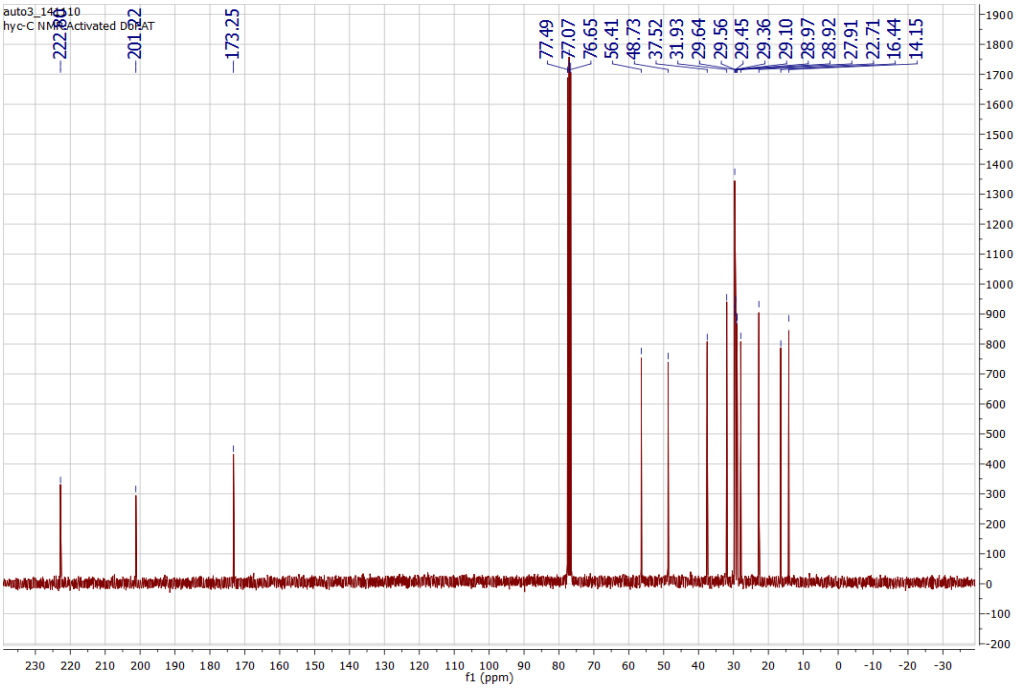

Figure A- 2: ^{13}C NMR of Activated DoPAT

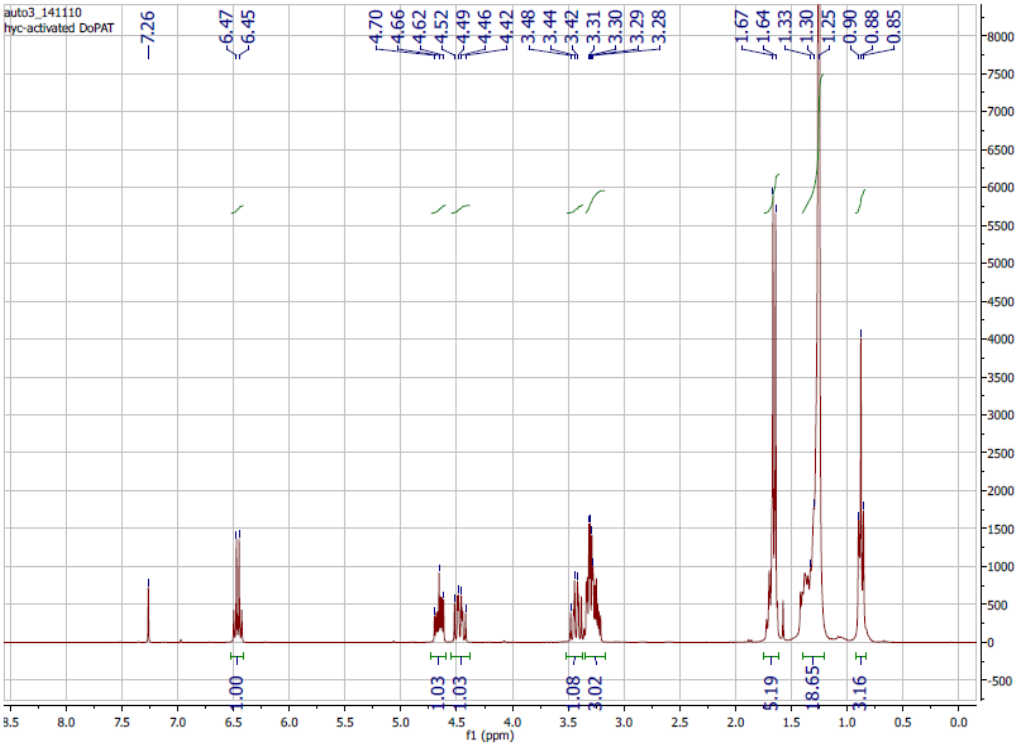

Figure A- 3: ^{1}H NMR of Activated DoPAT

To obtain the graft molecular weights, the polymer chains were cleaved by treating 50mg nanoparticles in 3 mL THF with 0.2mL HF (51% aqueous solution). The molecular weights and dispersity indices (Đ) of the resulting grafts were then analyzed by GPC.

A.2 Gas and Vapor Flow Control Apparatus

Flow rates of gases, including nitrogen used for solvent vapor streams, were controlled using MC-200SCCM-D mass flow controllers (Alicat Scientific). These controllers can be remotely controlled with a computer for nearly instantaneous flow rate changes and are calibrated for use with of multiple gas species. All tubing and fittings are PTFE unless otherwise noted.

A.2.1 Gas Flow Control

For light gas applications, we used two mass flow controllers (MFC) with one dedicated to clean, dry nitrogen off of a compressed cylinder. Other gases (e.g. CO_2 or CH_4) were controlled with the other MFC, connected to a compressed gas cylinder for the respective species. Inlet pressures to MFCs were help constant at 30psi. Lines were routed to a chemical fume hood exhaust and flushed for ~5 minutes after switching gas type. When films were not being tested, a steady supply of pure nitrogen at 100sccm was continuously purging over the crystal. To begin a light gas QCM experiment, the nitrogen MFC was switched off at the same time the test gas was set to 100sccm. So long as the gas retention rate in the headspace above the crystal was very small (<1s), effect of gas flow rate on the diffusion constant was negligible. For concentration effects (see section B.6) on CO_2 diffusion, CO_2 and nitrogen were mixed directly at a known temperature and pressure and partial pressures were determined assuming the ideal gas law.

A.2.2 Vapor Flow Control

A saturated penetrant stream is created by bubbling 50sccm of dried and filtered nitrogen gas through pure liquid ethyl acetate through successive fritted gas washers ("bubblers"). Nitrogen is used as the carrier gas because its solubility in these materials is much lower than ethyl acetate, and at standard conditions (298K, 1atm) we do not observe any discernable sorption of nitrogen above noise using standard QCM (*without* energy dissipation). The bubblers are submerged in an ethylene glycol circulating bath to hold the solvent at a constant temperature, which is held at 0°C for QCM experiments (Chapter 2), and is varied for SANS experiments (Chapter 3). For QCM experiments, prior to entering the solvent bubblers, the nitrogen stream was passed through a copper cooling coil also submerged in the ethylene glycol bath, to ensure the gas temperature was the same as the liquid solvent. This saturated stream can be mixed down with a known mass flow of pure nitrogen (ranging from 100 to 20sccm) from the second MFC, allowing for precise control of penetrant partial pressure. Ethyl acetate partial pressure is calibrated using a gas chromatograph with a flame ionization detector (Agilent).

Differential sorption experiments are conducted by incrementally decreasing the flow rate of dried nitrogen used for mix down, effectively increasing the partial pressure of penetrant in the vapor stream. After mixing, the vapor is flowed into a copper heating coil submerged in a water bath held at 25°C to bring the stream back to room temperature. Temperature of the gas is monitored with thermocouples at various points within the lines. To ensure the vapor stream is in equilibrium after start-up of the bubblers before exposing the films, the stream is routed to a chemical fume hood exhaust via a three-way ball valve. After ~5min, the valve is turned to direct flow to the crystal. For subsequent measurements where the nitrogen bypass is systematically and instantaneously stepped down, we do not perform the mixing equilibration.

A.3 QCM Measurement Technique

Here we present in more detail QCM measurements and data analysis methods. For supplemental material to Chapter 2, refer to Appendix B.

After preparation of films on QCM crystals using methods detailed in Chapter 2, dry film frequencies and resistances, f_f and R_f, respectively, were recorded prior to gas/solvent annealing the films under a saturated gas or penetrant vapor stream for at least 12 hours. Films were then re-dried under 100sccm of nitrogen for 24 hours. Film frequencies and resistances measured after solvent annealing were within 10Hz or 0.05Ω of those measured before solvent annealing. Mass added (per unit area) onto the crystal surface depresses the crystals resonant frequency, and external damping increases the crystal resistance. In the limit that the added polymer film is rigid and the mass uptake Δm is small relative to the mass of the film, the frequency response is linear and related to material properties based on the Sauerbrey Equation [119]:

$$\Delta m = -\frac{\sqrt{\rho_q \mu_q}}{2{f_q}^2}\Delta f, \quad \Delta R = 0 \tag{A.1}$$

where Δf is the frequency change and ρ_q and μ_q are the density and shear modulus of quartz, respectively. Δf and ΔR (the change in the resistance of the crystal) are recorded continuously via data acquisition software to allow for *in situ* measurement of penetrant mass loading. Note that for vapor experiments, where the penetrant has high solubility and relatively high mass, crystal frequency fluctuations become larger with increasing solvent concentrations, limiting the accuracy of experiments for penetrant pressure, relative to its saturated value, above 0.35atm. Since we observe no significant increase in ΔR for film thicknesses below 950nm, the Saurbrey's equation

holds to calculate the total mass uptake as a function of Δf. Fick's Law for transient diffusion can then be applied:

$$\frac{\partial C}{\partial t} = \frac{\partial}{\partial x}\left(D\,\frac{\partial C}{\partial x}\right) \tag{A.2}$$

where D is the diffusion constant, $\frac{\partial C}{\partial x}$ is the concentration gradient across the membrane direction x, and $\frac{\partial C}{\partial t}$ is the concentration change with time. The appropriate boundary conditions are $\frac{\partial}{\partial x}c(0,t) = 0$, $c(l,t) = Kc_1$, and $c(x,0) = Kc_0$, where x = 0 corresponds to the crystal surface and $x = l$ corresponds to the carrier gas/film boundary, where l is the film thickness. The measured mass uptake per unit area M during a sorption experiment is defined as $\int_0^l c(x,t) - Kc_0 dx$. Defining the normalized fractional mass uptake $\widetilde{M}$ for a given sorption experiment as $\frac{M(t)-M(0)}{M(\infty)-M(0)}$, it follows from derivations by Crank that $\widetilde{M}(t) = 2\left(\frac{Dt}{l^2}\right)^{\frac{1}{2}}\left[\pi^{-\frac{1}{2}} + 2\sum_{n=1}^{\infty}(-1)^n i\,erfc\frac{nl}{\sqrt{Dt}}\right]$ (36). In the limit of short and long time scales, this equation reduces to

$$\lim_{t\to 0}\widetilde{M}(t - t_0) \cong \frac{2}{l}\sqrt{\frac{D_{st}t}{\pi}} \tag{A.3}$$

$$\lim_{t\to \infty}\widetilde{M}(t - t_0) \cong 1 - \frac{8}{\pi^2}e^{\left(\frac{-D_{lt}\pi^2 t}{4l^2}\right)} \tag{A.4}$$

Short time diffusion constants, D_{st}, were calculated by fitting Equation A.3 to the data in the range of $0.1<\widetilde{M}<0.45$; long time diffusion constants, D_{lt}, were calculated by fitting Equation A.4 to the range of $0.6<\widetilde{M}<0.95$. For a truly linear sorption experiment, $D_{st} = D_{lt}$. The penetrant weight fraction in the film was calculated using the relation $\omega_1 = \Delta f/(\Delta f + f_q - f_f)$ where the subscripts 1 and 2 refer to the penetrant and polymer, respectively. Partition coefficients were

calculated by relating the penetrant weight fraction in the film with gas partial pressure using the relation $= \frac{RT\omega_1\rho_1\rho_2}{M_{n_1}p_1[\omega_1\rho_2+\rho_1(1-\omega_1)]}$, where p_1 is the experimental partial pressure. Permeability data were fit to 2-parameter exponential models using Microsoft Excel.

A representative example of frequency data and diffusivity extraction from $\widetilde{M}(t)$ employing Fickian diffusion is shown in Figure A- 4A and Figure A- 4B. The fits of Equations A.3 and A.4 to the data accurately capture the diffusion processes exhibited by both the neat and grafted composite materials. The frequency shift after one hour also remains stable for long times up to 5 days, indicating that the penetrant has reached equilibrium within the sample. The calibration of the Saurbrey equation for these materials (Figure A- 4C) show that this equation is valid for film thicknesses as large as $1.2\mu m$. The combination of the well-modeled data and good agreement between D_{st} and D_{lt} (Figure A- 4D) indicate that the diffusion mechanism for both neat PMA and PMA-g-SiO_2 nanocomposites is indeed Fickian.

Unsteady sorption measurements of CO_2 were carried out using a QCM equipped with a flow cell (Biolin Q-Sense, Switzerland). Different partial pressures of each gas in nitrogen were prepared in a manner similar to that described above, but the gas streams were directly mixed at known temperatures and pressures and the partial pressure of the gas was deduced using the ideal gas law. Shifts in Δf and sensor dissipative energy ΔD were modeled using the Voight-Kelvin Model.[120]

Gas diffusion constants are measured in the manner described above. Gas solubility was calculated from QCM by converting the Δm to the volume of gas dissolved in the film volume:

$$S = \frac{\frac{mRT}{PM_{gas}}}{lP_{partial}} \tag{A.5}$$

Where T and $\boldsymbol{P}$ are the experimental temperature and pressure, respectively, R is the gas constant, $P_{partial}$ is the gas phase partial pressure and M_{gas} is the molecular weight of the gas. Gas solubility measurements were conducted at 35°C so as to allow comparison with Robeson plot data, which is historically reported at this temperature.

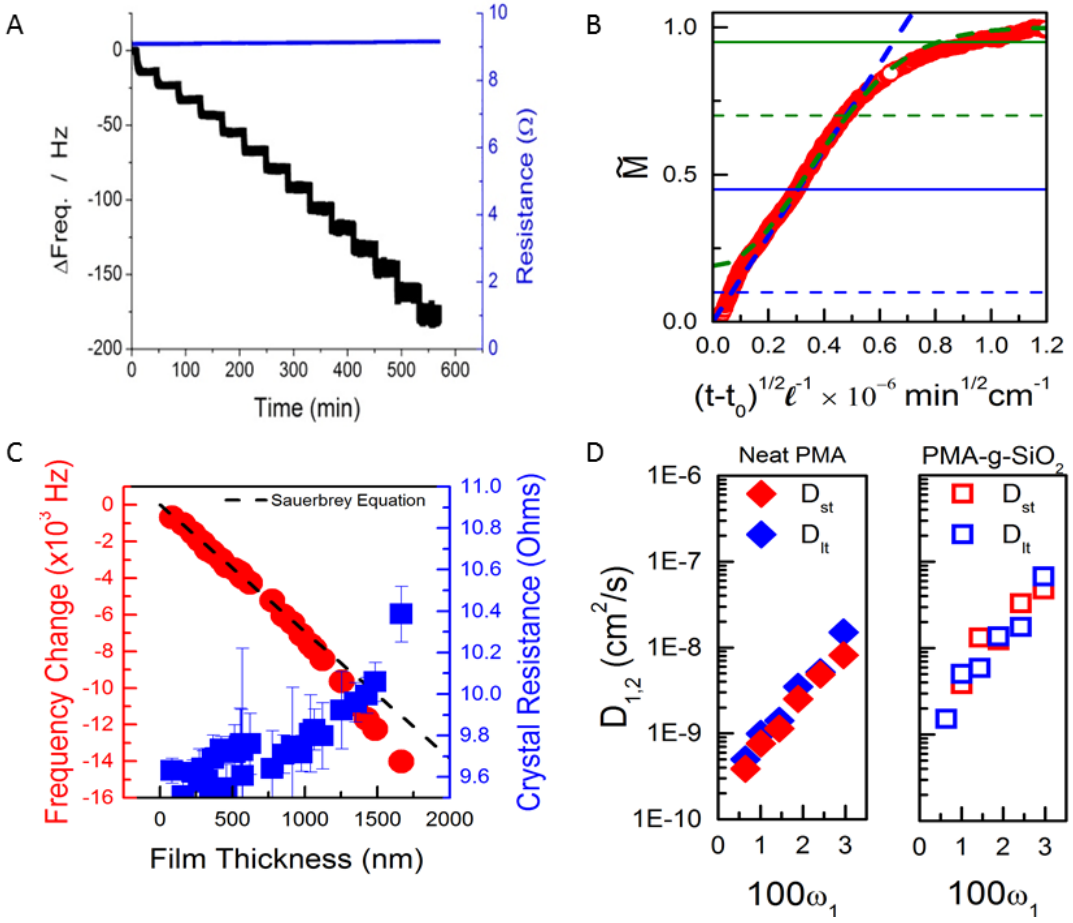

Figure A- 4: Quartz crystal microbalance analysis methods. (A) Representative experimental data from a QCM experiment. Each sharp drop in frequency corresponds to a step change in penetrant activity; (B) Representative fitting of overall fractional mass uptake for a single step change to Fick's equations; t is time, and t_0 is the initial time at which the experiment was begun. (C) Verification of Sauerbrey Equation as a function of film thickness. This equation is used to estimate film thickness from Δf when change in crystal resistance is less than 0.5Ω. All CQM experiments were performed on films less than $1\mu m$ thick; (D) comparison of D_{st} (red) and D_{lt} (blue) for a neat PMA melt and a PMA composite, as a function of penetrant weight fraction, ω_1, in the polymer phase. Within error, D_{st} and D_{lt} are equal to each other, indicating interval step sizes are sufficiently small.

A.4 Free Volume Characterization

A.4.1 Positron Annihilation Lifetime Spectroscopy (PALS)

PALS analysis was performed on bulk, dry samples of PMA composites at the University of Michigan. Intensity spectra were fit to a single positronium (Ps) lifetime τ_3 using the software POSFIT. The Ps lifetime and free volume element size can be correlated using the Tau-Eldrup model, which assumes an infinitely deep spherical well where the Ps annihilate with electrons when it is within a short distance of the element surface: $\frac{1}{\tau_3} = 2\left[1 - \left(\frac{r}{r+r_0}\right) + \frac{1}{2\pi}\sin\left(\frac{2\pi r}{r+r_0}\right)\right]$, where r_0 is the electron layer thickness, estimated at 0.1656Å, and r is the radius of the average free volume element. This model is accurate for nanopores ($r < 1$nm). Fitting with the rectangular Tau-Eldrup Model, which is valid for larger pores, yields similar results.[121]

A.4.2 Surface Area Analysis via N_2 Adsoprtion (BET)

Specific material surface area and average pore sizes were probed using N_2 adsorption/desorption at 77K using a Quantachrome Nova2200E pore size analyzer (Florida). Approximately 200mg of sample was dried under vacuum at 25°C, 75°C and 150°C successively each for one day to ensure each material was free of any solvent. The samples were then degassed under ultra-high vacuum (<.001mmHg) at 100°C for 16 hours, weighed and then transferred to the analysis system. Sorption and desorption were carried out at liquid nitrogen temperature (77K). Apparent surface areas were calculated from N_2 *adsoprtion* data using the multipoint Brunauer-Emmet-Teller (BET) method[122]:

$$\frac{p}{v(p_0-p)} = \frac{1}{v_m c} + \frac{c-1}{v_m c}\frac{p}{p_0} \quad , \quad c \approx e^{\frac{E_{ads}-E_{cond}}{RT}} \tag{A.6}$$

Where p is the partial pressure of N_2, p_0 is the saturation pressure, v is the total volume of gas adsorbed, and v_m is the volume of gas adsorbed when the entire surface is covered by a monolayer of gas. E_{ads} and E_{cond} are related to the energies of adsorption and condensation, respectively, and can provide information on the heat of adsorption. This model is typically valid for experimental data points where the relative N_2 pressure $P/P_0 < 0.3$, which corresponds to a monolayer of N_2 having adsorbed on the sample. Pore size distributions are calculated from the N_2 *desorption* data using the Barrett, Joyner and Halenda (BJH) method[123], which is sensitive to pore sizes in the range of 1-50nm. It should be noted that insufficient amount of the PMA composite with M_n=92kDa; we instead report results from a PMA composite material with M_n=101kDa at a similar grafting density of σ= 0.44chains/nm^2.

Representative N_2 adsorption and desorption isotherms of neat PMA (M_n=135kDa) and PMA composites (M_n=132kDa, σ = 0.43chains/nm^2) is shown in Figure A- 5A. The Y-axis shows the volume of N_2 sorbed per mass of sample. From these raw data it is evident that the composite materials have higher N_2 solubility than neat PMA at similar M_n. The relative increase in adsorbed N_2 for both adsorption and desorption experiments is shown in Figure A- 5B. The composite material contains more adsorbed N_2 for the representative relative pressure in both adsorption and desorption experiments. It is important to note that while there is indeed a hysteresis present in both neat and composite PMA samples, the composite outperforms the neat polymer in both respects. Intermediate PMA composite M_n (for example, 62kDa, see Figure A- 5C) show even greater solubility enhancements.

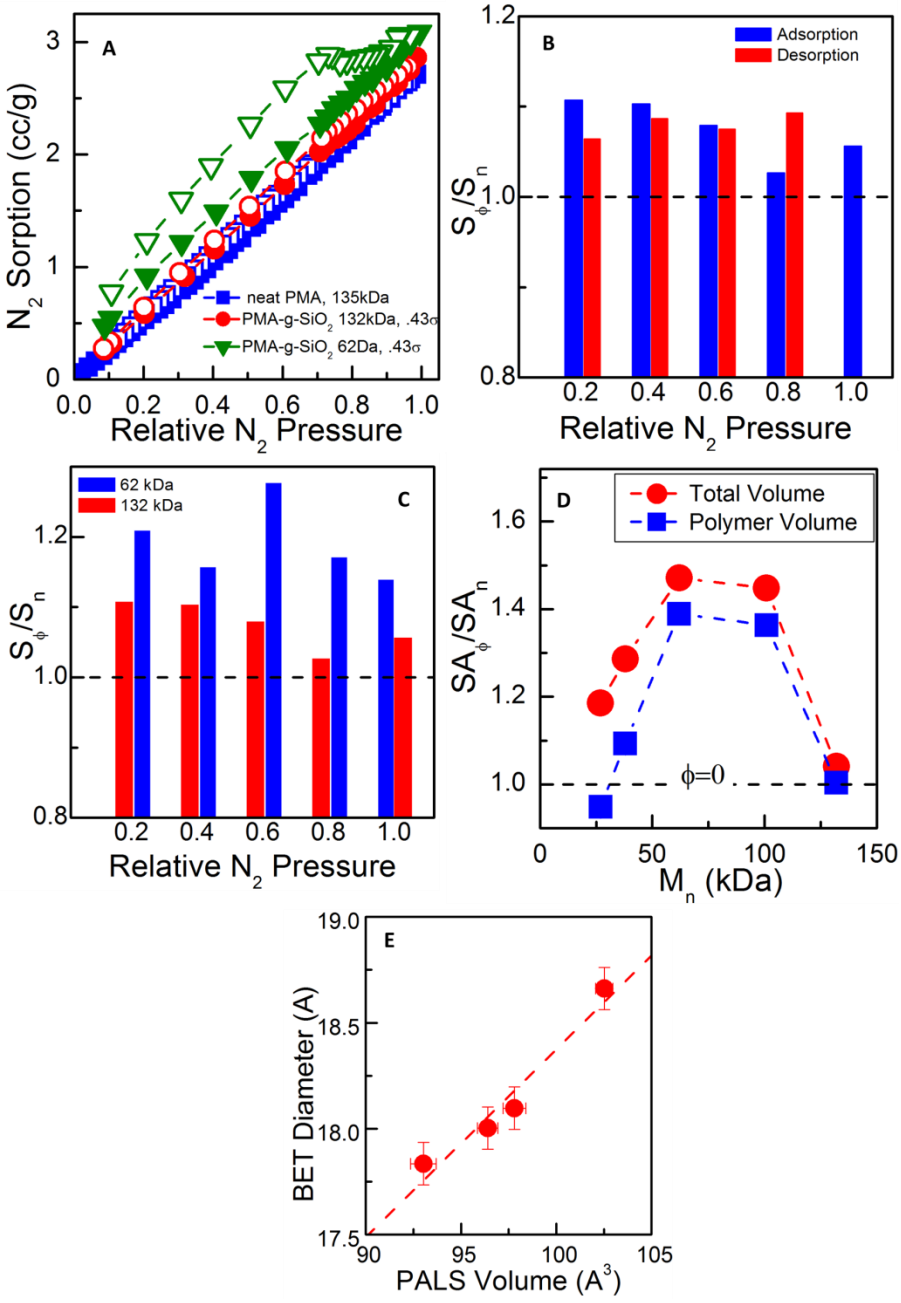

Figure A- 5: N_2 Adsorption/Desorption Isotherm and Solubility (A) Comparison of N_2 sorption isotherms (cc/g) for neat PMA and PMA-grafted nanoparticles at high Σ ($0.43 \text{chains}/\text{nm}^2$) with comparable molecular weights. The composite isotherm distinctly lies above that of neat PMA; (B) Relative N_2 solubility in the composite ($M_n = 132$ kDa) during adsorption and desorption at a variety of N_2 pressures. Neat PMA ($M_n = 135$ kDa) is denoted by the black dashed line; (C) solubility enhancement of two composite materials ($M_n = 62$ kDa and 132 kDa) (D) Relative increase of material surface area (cc/g); (E) Correlation of pore sizes measured from BET and PALS free volume element sizes

The measured BET surface area calculated from Equation A.7 of the composite materials is shown

in Figure A- 5D. We also report the volume-specific surface area obtained by multiplying the surface area on a per-mass basis by the measured density of the material

$$SA_{specific} = \rho_c \times SA_{measured} \quad \text{(A.7)}$$

In the case of neat PMA, ρ_c is replaced with ρ_{poly}. In both cases the surface area is elevated compared to neat PMA. Composites with moderate M_n display the highest relative surface area increase.

The average pore radius extracted from the desorption data is shown in Figure 2.4C. We observe relative pore size increases that are qualitatively consistent with those measured from PALS (note that this does not include the M_n=101kDa composite, for which PALS data was unavailable) as shown in Figure A- 5E. The increase in N_2 solubility, material specific surface area, and average pore size serve as confirmations that the PMA composites indeed possess elevated solubility for a variety of light gases, and that additional surface area and volume is available in the composite materials to allow for increased gas uptake.

A.5 Differential Scanning Calorimetry (DSC)

Glass transition temperatures, T_g, of matrix-free grafted nanoparticle composites with varied M_n and σ as well as neat PMA melts of comparable molecular weights were measured using temperature modulated differential scanning calorimetry (TMDSC) (TA Instruments Discovery250, New Castle, DE, USA). 5-10mg samples were cut from solvent cast, annealed films approximately 0.5-1mm in thickness. Samples in aluminum T-zero pans were compared with

empty reference pans. Thermal history was erased by equilibrating pans at 110°C for 35min. Afterwards, temperature was ramped to -30°C at 2°C/min and modulated at ±1.27°C every 60s. T_g values were extracted from reversible heat capacity versus temperature using the TA TRIOS software.

Figure A- 6 shows T_g as a function of M_n for both grafted PMA composites at 0.43chains/nm^2 and neat melts. As expected, PMA melt T_g data obey the Fox-Flory equation as a function of molecular weight:

$$T_g = T_g^{\infty} - \frac{K}{M_n} \tag{A.8}$$

where T_g^{∞} is the high molecular weight asymptote and K is the Fox-Flory constant. A least-squares fit gives the parameter K to be ~3.6x10^5, which is in reasonable agreement with published results for PMA.[124] Interestingly, T_g does *not* appear to change with molecular weight in the grafted

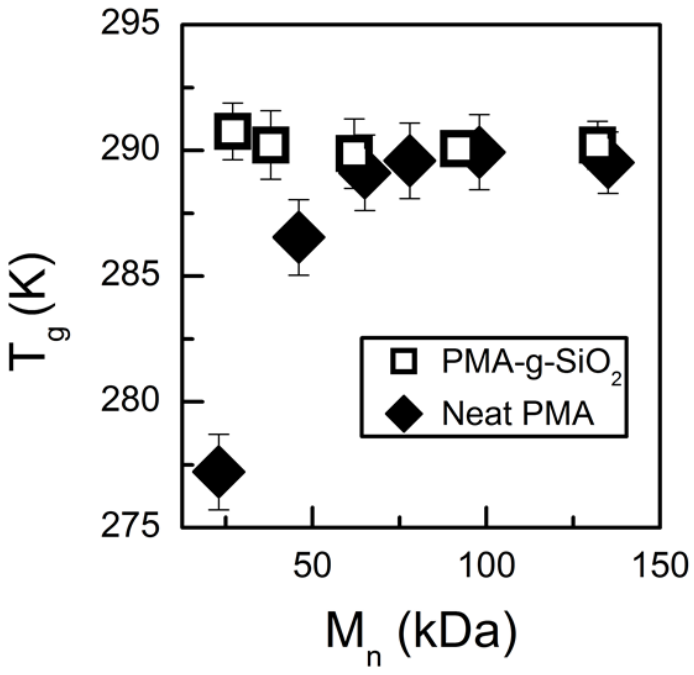

Figure A- 6: Glass Transition Temperature Tg of PMA Grafted Nanoparticles at 0.43ch/nm^3 and various M_n (□) and linear PMA melts of corresponding M_n (◆)

system. The T_g for all the grafted samples are equal within experimental error to the melt T_g^{∞} regardless of graft molecular weight, and therefore silica content.

A.6 Thermogravimetric Analysis (TGA)

Weight fractions of silica core particles were determined using either a TGA-Q500 Discovery TGA (TA Instruments). Approximately 7-14mg of sample was loaded into a tared platinum 100µl TGA pan. Pans were first cleaned by gently rubbing the surface with a cotton-tipped applicator dampened with acetone. Remaining dust and debris were removed by heating the pans with a butane torch for ~15 seconds. Samples were first held at 100°C for 30min to determine if any residual solvent was present. Next, samples were heated in oxygen to 700°C at a rate of 10°C/min. Silica residue was calculated at 690°C using the TA Instruments software (Universal Analysis and/or TRIOS). TGA tests were repeated at least three times for each material.

A.7 Computer Simulations

A.7.1 MD Simulation of Ordered Nanoparticle Lattice

Each nanoparticle of diameter $s_n = 10s$ is grafted with $N_c = 200$ linear polymer chains of length $N_p = 10$. Any pair of particles i and j at a distance r_{ij} apart, where $i, j \in \{n, p\}$ with n and p indicating nanoparticle and polymer respectively, interact with each other via the Lennard-Jones (LJ) potential

$$u(r_{ij}) = 4\varepsilon\left[\left(\frac{s}{r_{ij}-\Delta_{ij}}\right)^{12} - \left(\frac{s}{r_{ij}-\Delta_{ij}}\right)^{6}\right],\ r_{ij} < r_c + \Delta_{ij} \tag{A.9}$$

where ε and s set the energy and length scales. We choose $\Delta_{nn} = s_n - s = 9s$, $\Delta_{np} = (s_n - s)/2 = 4.5s$ and $\Delta_{pp} = 0$. The cutoff distance is set as $r_c = 1.12\sigma$ such that the pair potential is purely repulsive. All the chain monomers are connected via the finite extensible nonlinear elastic (FENE) bond of strength $K = 30\ \varepsilon/s^2$ and length $R_0 = 1.5s$. (37) The first monomer of each chain is anchored on the surface of the nanoparticle with a rigid bond. All particles have the same mass m, and the Boltzmann constant k_B is set to unity.

The LAMMPS simulation package is used with a time step $dt = 0.001\sigma\sqrt{m/\varepsilon}$. (38) The system of $N_n = 32$ polymer grafted nanoparticles are first generated on a dilute face-centered cubic (FCC) lattice. After relaxation of polymer chains at temperature $T = 1.0\ \varepsilon$, the FCC lattice is rapidly compressed to the final pressure $P = 2.0\ \varepsilon/\sigma^3$. The system is then equilibrated for 10^6 time steps at $T = 1.0\ \varepsilon$ and $P = 2.0\ \varepsilon/\sigma^3$.

A.7.2 Single Particle Surface Analysis

We performed MD simulations to clarify the surface structure of isolated polymer-grafted nanoparticles (i.e., a particle in a dilute solution). The simulation method is similar to the calculation for the equilibrium configuration of polymer-grafted nanoparticles on a crystal lattice. Each nanoparticle of diameter $\sigma_n = 7\sigma$ (σ is the diameter of one coarse-grained monomer) is grafted with $N_c = 30$ linear polymer chains of length $N_p = 5, 10, 20$, in a series of simulations. We looked for the farthest polymer beads that lay directly at a certain position on the surface and determined the effective radius of this particle at that position on the surface by time averaging for 10^6 time steps at $T = 1.0$. The effective surface was found by repeating this operation for every point on the surface.

A.8 Small Angle X-Ray Scattering (SAXS)

Bulk SAXS measurements as well as dilute solution particle form factor measurements were performed using SAXSLAB (Xenocs, Sassenage, France) laboratory instrumentation at Columbia University using 4 sample to detector configurations ("ESAXS", "SAXS", "MAXS", and "WAXS"). *In-situ* swelling experiments were conducted at the South Carolina SAXS Collaborative (University of South Carolina, Columbia SC, U.S.A). by connecting the SANS vapor flow control system described below in section A.9.2 to the vapor chamber accessory using the "SAXS" detector configuration.

A.9 Small Angle Neutron Scattering (SANS)

Thin film swelling SANS measurements in transmission were performed at either the NCNR (Gaithersburg, MD, USA) on the NG-7 beamline (λ= 6A) or the Laboratoire Lèon Brillion (LLB) (Saclay, France) on the PA20 beamline (λ= 5A) using two sample to detector distances of 4m and 1m, respectively, to achieve a q range of $0.008A^{-1} – 0.4A^{-1}$. The geometry of the sample holder restricts the high-q limit of the data relative to standard instrument configurations.

A.9.1 Sample Flow Cell Design for SANS Swelling

Due to the relatively low flux of SANS beamlines compared to those of synchrotron or even laboratory X-ray sources, coupled with the limited availability of neutron research facilities worldwide, SANS measurements are ideally performed with thick samples which minimizes counting time while maintaining good statistics. For our swelling experiments, however, sample thicknesses are constrained by the timescales required for the film to reach equilibrium with the vapor. For neat PMA and PMA-grafted composites, the diffusion coefficient for ethyl acetate is on the order of 10^{-8} cm^2/s.[4] A simple analysis following $t \sim \frac{L^2}{D}$ yields for $t \sim 1s$ that L, the film thickness should be ~1μm. To limit the equilibration time scales we therefore limit film thickness

to 1μm. So-called "stacking" of supported films on silicon wafers is a common method to increase sample volume in such cases.[125,126] In order to ensure all films were equally exposed to a controlled vapor stream, we required a custom flow cell which could accommodate the simultaneous swelling of multiple thin supported films. Although Shelton et. al. showed structural evolution during *in-situ* thin film solvent annealing could be tracked using only two films in contact with solvent vapor[127], this multi-film device allows us to deal with films with exceptionally long diffusion times.

Our custom flow cell (Figure A- 7) was produced using direct metal laser sintering from titanium oxide (Stratasys Direct, INC). The faces of the cell were designed to match those of the standard titanium sample cells from the NIST Center for Neutron Research (NCNR) and are compatible with the standard quartz windows and stainless steel retainer plates. The inside of the cell holds ten 1" diameter wafers back-to-back so that when sealed, each film is directly exposed to a small inner chamber where vapor passes through. The top is secured with stainless steel screws, and an indium wire gasket lines the lip of the base prevents leaks.

All interior holes inside the cell are 1/8'' in diameter or smaller, which increases gas velocity and ensures that all six inner chambers receive sufficient gas flow. The inlet and outlet ports can be customized to allow for flexibility in setup at different beam lines/neutron facilities. For these experiments, gas flow was directed in through the top and out through only one port, on the face opposite from the inlet. All inlet and outlet fittings are self-sealing so that the vapor flow can be disconnected after reaching equilibrium to reduce the amount solvent used.

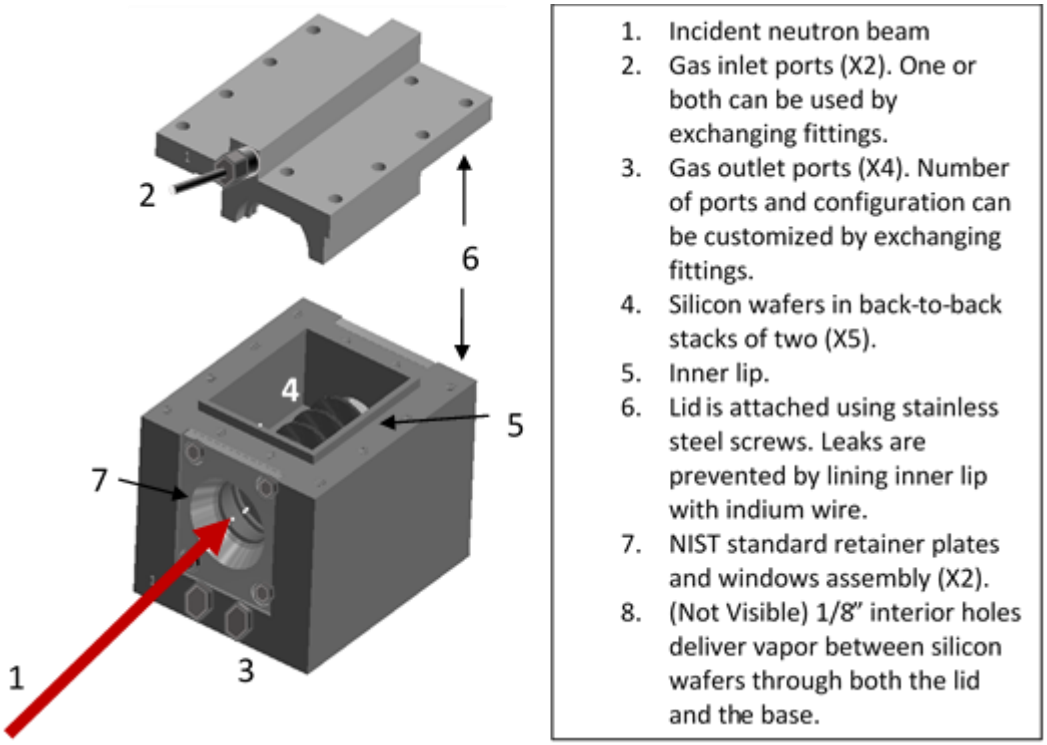

Figure A- 7: Custom sample holder for SANS swelling experiments. Inlet and outlet ports continue through the cell and can be customized by attaching various plugs or tube fittings. Retaining plates, windows, and screws were provided by NIST.

A.9.2 Solvent Vapor Control Apparatus and Procedure for SANS

The concentration of solvent vapor was controlled in a similar manner to previous works.[4,127,128] The general concept involves flowing nitrogen gas at a known mass flow rate through a liquid solvent to create a saturated vapor stream. The concentration of the saturated stream can be controlled by varying the temperature of the liquid solvent. A lower concentration of solvent vapor can be created by "cutting" the saturated stream with additional pure nitrogen. Due to the high price of the specialty deuterated ethyl acetate-d8, the large glass bubblers used in prior work were not well suited to these experiments. Therefore, stainless steel bubblers with a minimum operating capacity of 10ml were purchased from MDC Vacuum Products (Hayward CA,

U.S.A.). The bubblers were filled with approximately 15-18ml of solvent to ensure the bubbler outlet was sufficiently submerged, and the solvent level was topped off after 6 hours of flow at 50-60sccm. The solvent temperature was controlled by submerging the bubblers in a circulating bath chiller filled with ethylene glycol. At least 2 hours was allowed for thermal equilibration prior to beginning any swelling experiments upon a change in bath temperature or refilling of bubblers. All tubing used in the apparatus was 1/8'' outer diameter PTFE.

Before connecting to the SAXS swelling chamber or SANS sample cell, nitrogen flow was started through the bubbler line at either 50 or 60sccm (standard cubic cm per minute). Next, if necessary, the bypass flow rate was set and the streams were allowed to mix for 2-3 minutes to allow for equilibration. Presence of solvent vapor was verified by observing bubble flow rate in water. Once steady state was achieved, the vapor stream was connected to the inlet of the flow cell(s). For SANS measurements, the films were exposed to the vapor for at least 1 hour to ensure equilibrium, although SAXS measurements indicate no changes to the scattering patterns after only 30 minutes (Figure A- 8A). Before changing concentration or solvent contrast, the sample cell was flushed with 150sccm pure nitrogen for 1 hour to remove the solvent from the sample. This was only done for steps with sequentially increasing solvent concentration; to go from a higher concentration to a lower concentration of solvent in the film, the samples were removed from the cell and dried in a vacuum oven at 80°C for 1 hour. Recovery of the exact same spectra for the dry film ensured that drying the sample was effective and that the sorption processes were reversible and repeatable (Figure A- 8B). Additionally, SAXS measurements using both ethyl acetate EtAC-h_8 and perdeuterated ethyl acetate EtAC-d_8 yield the same spectra, which confirms

there is no preference towards either protonated or deuterated solvent by the film (Figure A- 8C).

Fitting parameters for swelling controls based on fitting procedure in section 0 are found in

Table A- 1: Fitting parameters of swollen films in SAXS controls as a function of swelling time

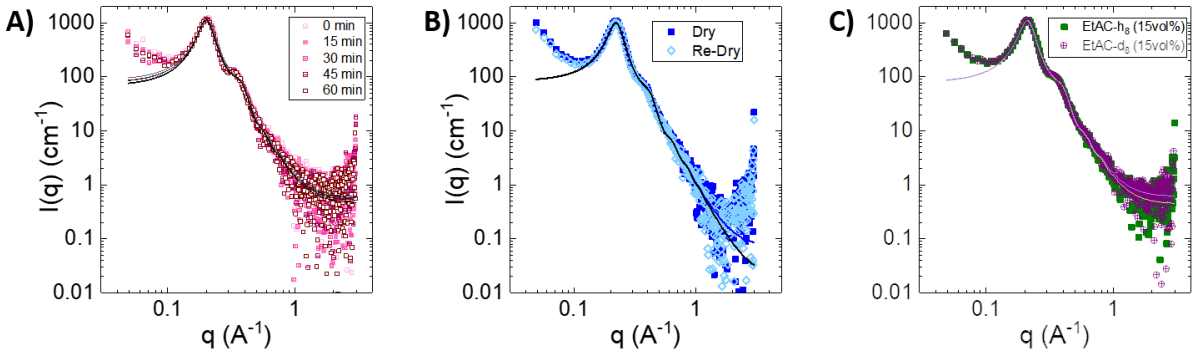

Figure A- 8: In-situ SAXS verification and controls. (A) Time dependence of intensity during solvent uptake. No change in intensity after 30 minutes of soak-time indicate films <1000nm reach equilibrium after 30min of solvent exposure. (B) Comparison of starting film to film after solvent exposure and subsequent drying at 80°C under vacuum. Recovery of identical spectra indicates swelling process is completely reversible and no permanent structural change is induced with solvent exposure. (C) Comparison in SAXS of protonated EtAC-h_8 and deuterated EtAC-d_8 at 15vol% solvent concentration, showing no preference for hydrogen or deuterium by film.

for $\phi_s(V)$=0.28. $\phi_{HS,w}$ refers to the volume fraction of hard sphere interactions from a Percus-Yevick structure factor

$\phi_s(V)$	$\phi_{p,w}$	σ	Core Particle Radius (nm)	η X 10^{-10} (cm^{-1})	$R_{HS,w}$ (nm)	ϕ_{HS}	$\phi_s(\eta)$
0	0.083	0.28	7.01	7.35	15.80	0.39	25.5
15	0.077	0.28	7.01	7.37	16.00	0.39	26.3
30	0.075	0.28	7.01	7.41	16.10	0.39	27.7
45	0.071	0.28	7.01	7.44	16.28	0.40	28.7
60	0.073	0.28	7.01	7.45	16.30	0.40	29.1

A.10 Non-Linear Rheology

In Figure A- 9 we provide raw stress (Σ) versus strain amplitude (γ_0) for various strain rates for two graft densities (0.47 and 0.66chains/nm^2) for two average molecular weight (~80 and ~130kg/mol), as well as neat PMA of corresponding molecular weights. The last strain rate plotted corresponds to the last strain rate sampled before the sample experienced fracture.

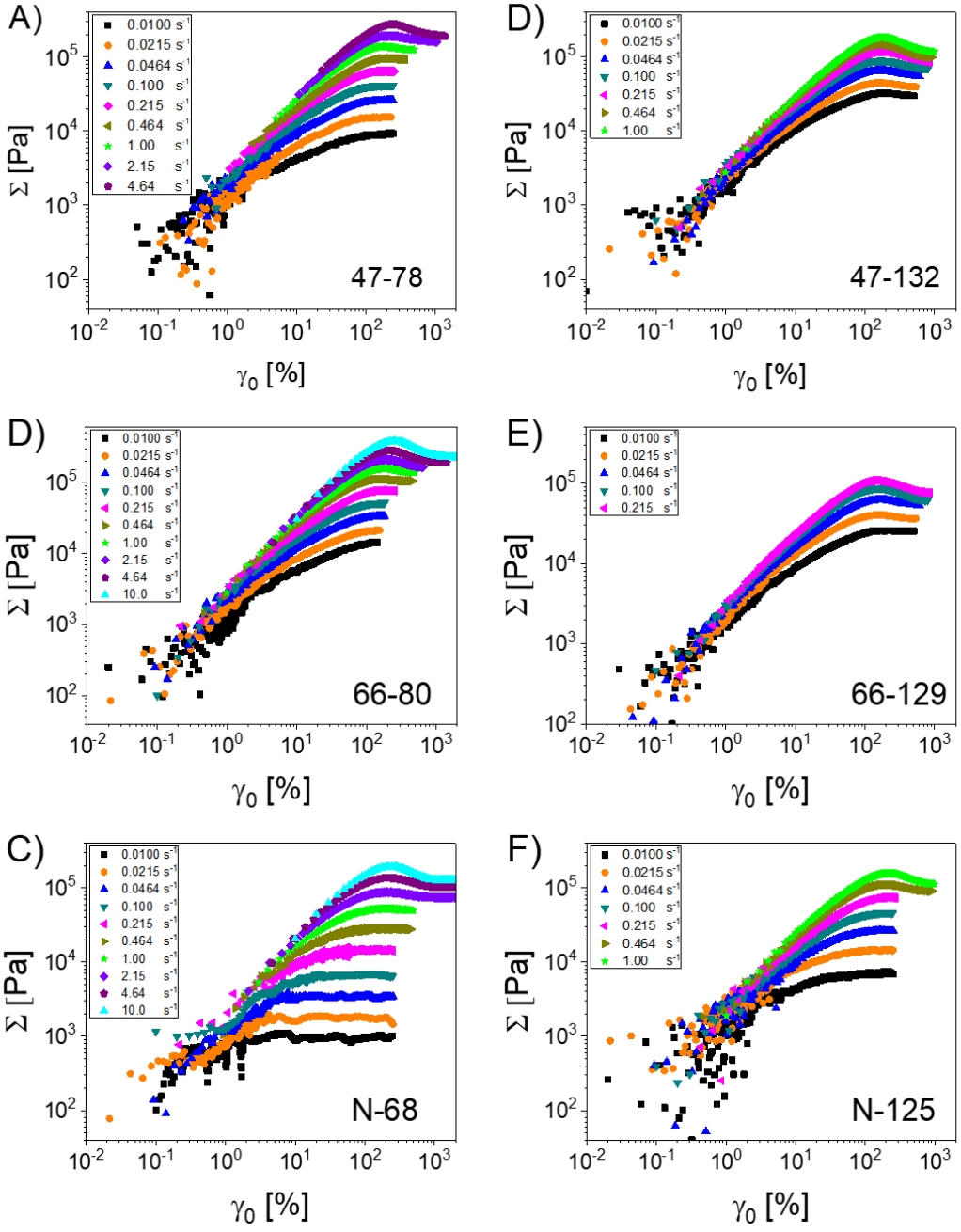

Figure A- 9: Raw stress versus strain response in start-up of steady shear for various GNP and neat systems at various strain rates

Figure A- 10 shows the raw viscosity (η) as a function of time during start-up of steady shear for various strain rates for two graft densities (0.47 and 0.66chains/nm^2) for two average molecular weight (~80 and ~130kg/mol), as well as neat PMA of corresponding molecular weights. The linear viscoelastic envelop from SAOS/creep tests are superimposed on the data.

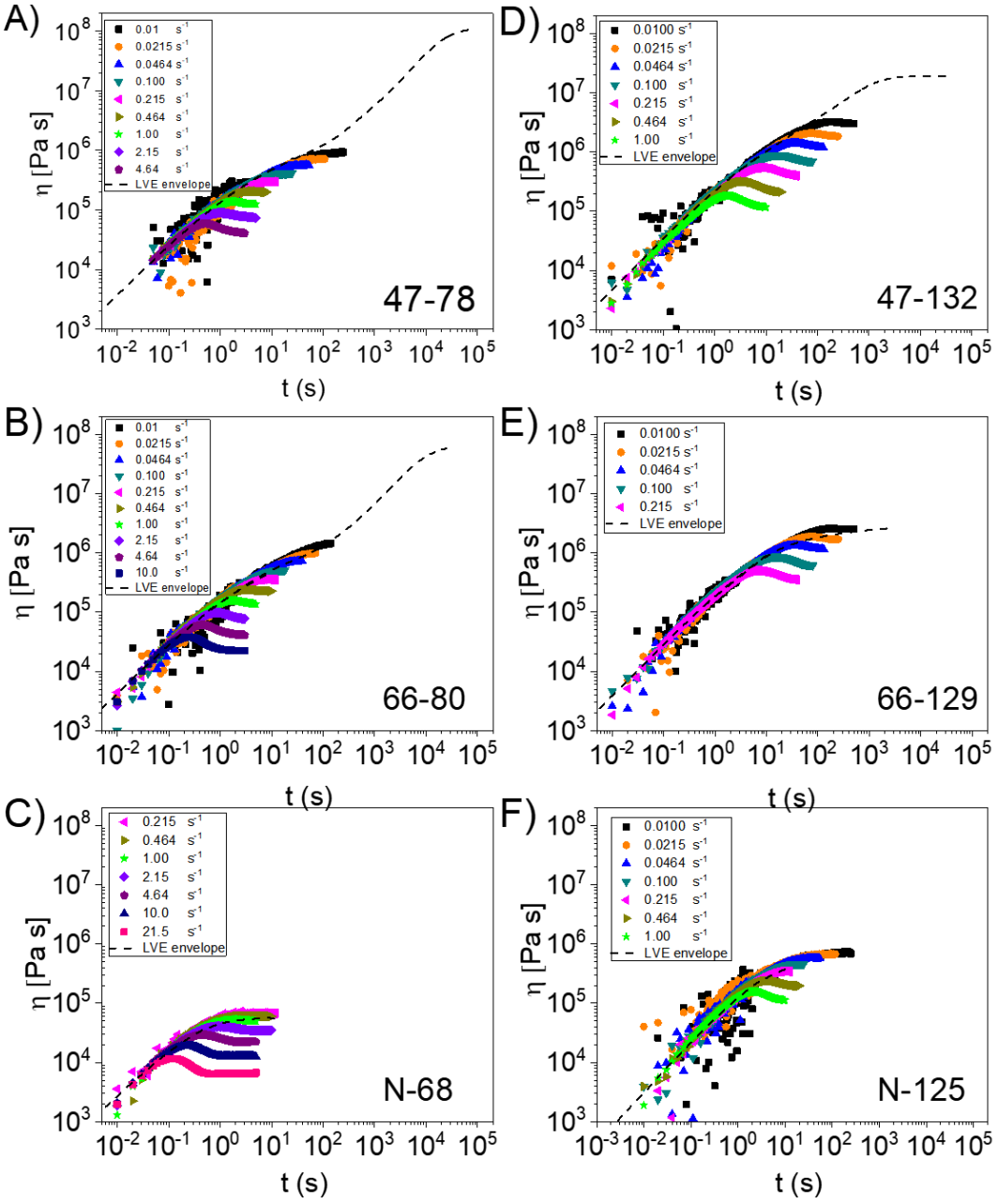

Figure A- 10: Raw viscosity versus time for start-up of steady shear for various GNP and neat systems at various strain rates. For sample N-68 (C), low strain rates are not shown due to high noise. Dashed lines represent linear viscoelastic (LVE) envelope from SAOS/creep measurements

Figure A- 11 shows the relaxation after cessation of steady-state flow for two graft densities (0.47 and 0.66chains/nm^2) for two average molecular weight (~80 and ~130kg/mol), as well as neat PMA of corresponding molecular weights for a variety of strain rates. The stress is normalized

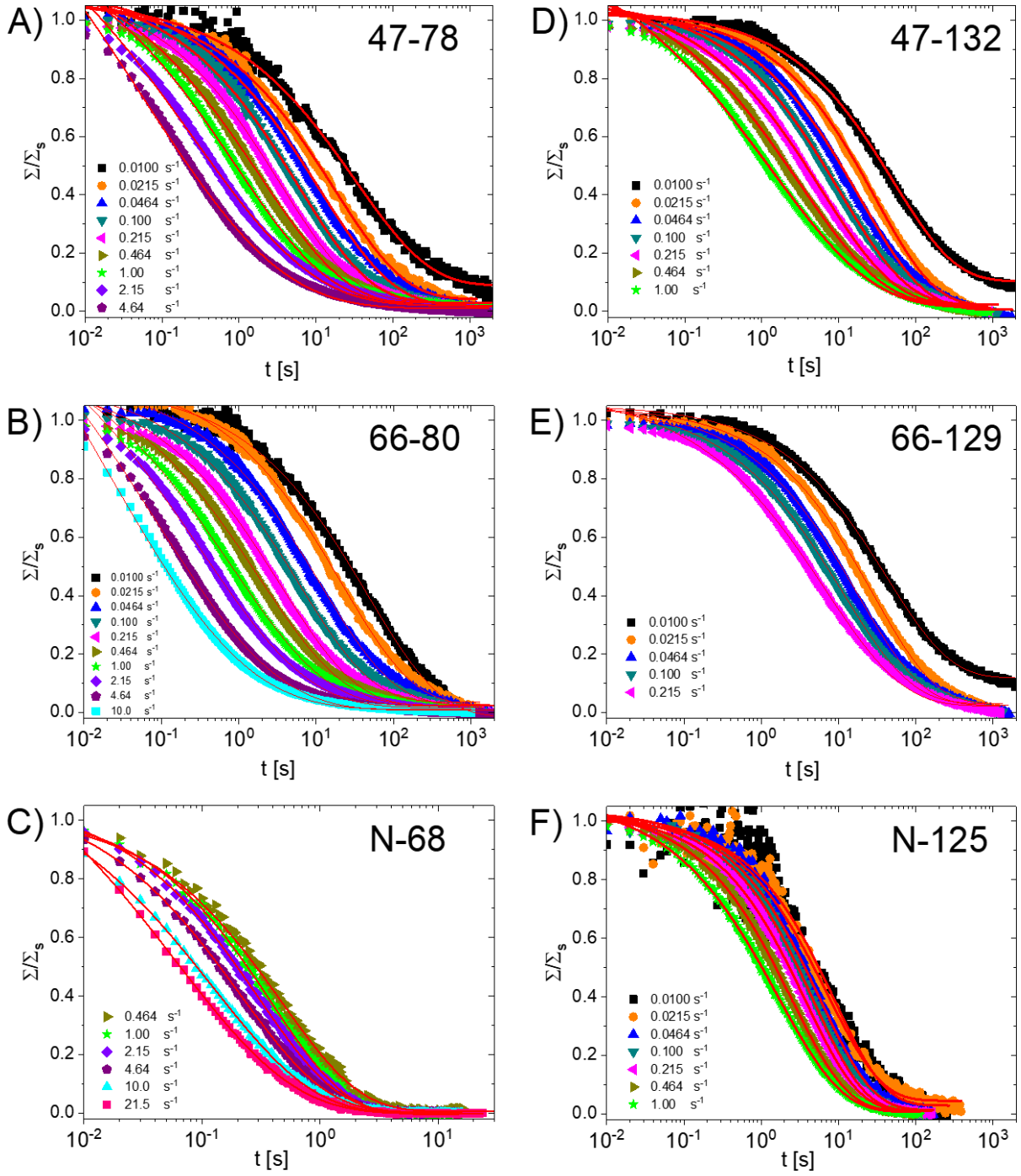

Figure A- 11: Stress relaxation upon cessation of steady-state flow as a function of time for various GNP and neat systems at various strain rates. For sample N-68 (C), low strain rates are not shown due to high noise. Red lines represent stretched exponential fits.

by the steady-state plateau stress. Due to high levels of noise, only relaxations for relatively high strain rates are plotted for sample N-68. Relaxation curves are fit using a stretched exponential function. The fitting parameters τ and β are shown for each sample at various strain rates in Figure A- 12. For low strain rates, the fit parameters of neat PMA are independent of strain rate, although there is a shift with molecular weight. In the GNP system, the relaxation times are strongly dependent on shear rate, with only slight differences in molecular weight at low strain.

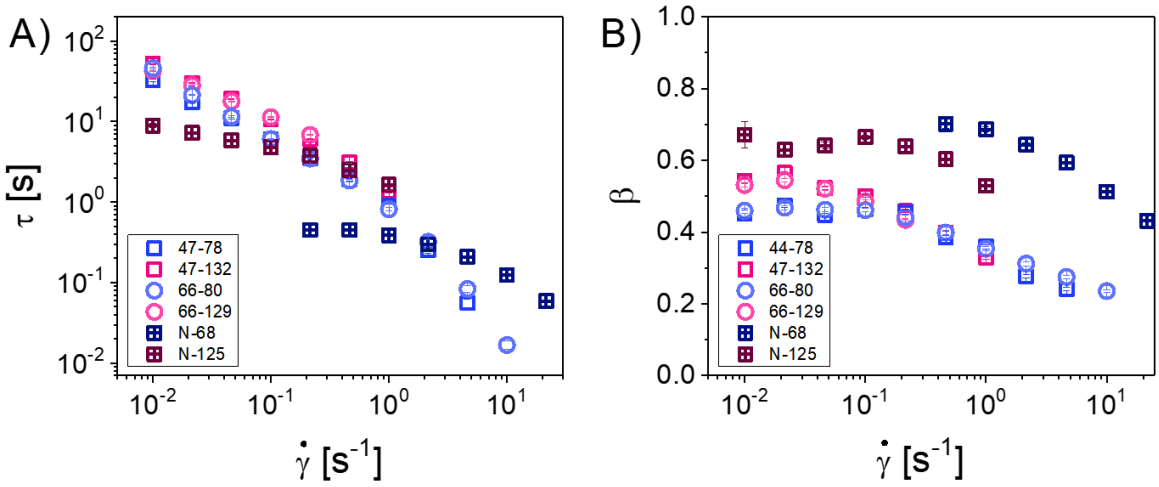

Figure A- 12: Stretched exponential fit parameters (A) τ and (B) β of relaxation curves upon cessation of steady-state shear.

Appendix B - Supplementary Info. (Ch. 2)

Here we present additional controls and data analysis of transport phenomena discussed in Chapter 2.

B.1 Neat Polymer Controls

The measured permeability of neat PMA over a range of molecular weights similar to those used for composite materials are shown in Figure B- 1A. While PMA with chain lengths <25kDa show a slight elevation when compared with higher M_n, this increase is less than 6% in most cases. The increase is even less pronounced for 42kDa chains (<3%), which is within experimental error. This is consistent with DSC experiments (see below) which show that the T_g of short polymer chains is reduced from the presence of additional chain ends, which provide additional free volume. Furthermore, we observe no discernable change in permeability across a wide range of and film thicknesses, from 400nm-1500nm (See Figures Figure B- 1A and Figure B- 1B). Both of these observations are corroborated by previous QCM studies of neat PMA films.[74,128] The permeability of CO_2 in neat PMA is also shown to be constant for film thicknesses between $0.5 < l > 50$

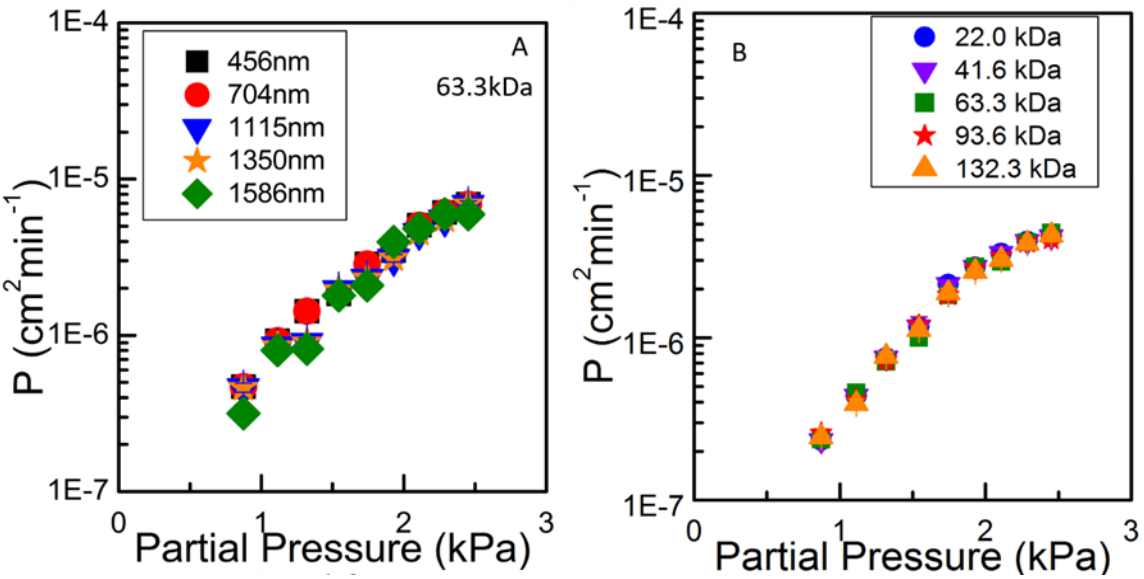

Figure B- 1: Neat PMA Transport Data. (A) Extracted ethyl acetate permeability data for 63kDa neat PMA film at a variety of film thicknesses. (B) Ethyl acetate permeability data for neat PMA with a variety of M_n. The shortest chain length has minor permeability elevations (< 6%) relative to higher M_n.

B.2 Bare Particles in Neat Polymer

Physical mixtures of PMA (M_n =72kDa) and bare silica nanoparticles also show a substantial decrease in material permeability (Figure B- 2), consistent with conventional composite theories regarding molecular diffusion in the presence of inert particles. Similar reductions measured by QCM in the same polymer/nanoparticle system have also been reported previously.[74]

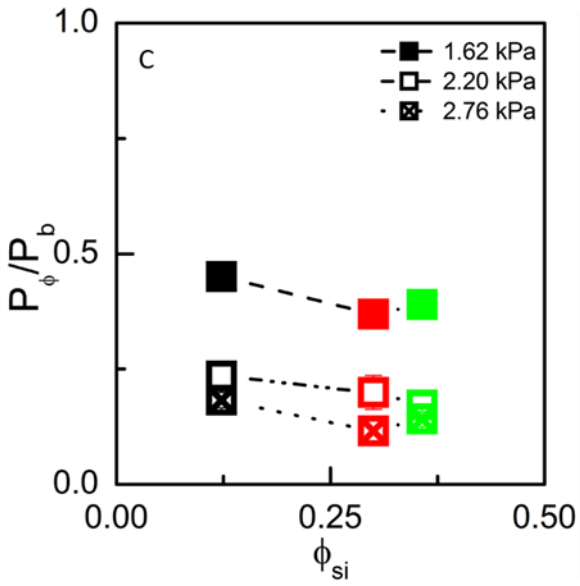

Figure B- 2: Relative permeability of ungrafted silica composites as a function of silica volume fraction. Data are shown for multiple experimental partial pressures, and are normalized by the value in the corresponding neat PMA M_n

B.3 Effects of Graft Density

We first review PMA composites with a low grafting density (σ = 0.07 chains/nm^2). Permeability data extracted from the QCM experiments described above are shown in Figure B-3A. For these plots the neat polymer permeability is taken to be the average of the five molecular weights reported in Figure B- 1B. At low molecular weights (M_n <25kDa), permeability in general is suppressed relative to the neat polymer, as shown in the corresponding volcano plot in Figure B- 3B. Moderate M_n have permeabilities comparable to the neat PMA, with some observable increases at intermediate M_n. The 72kDa composites display permeability increases as large as 1.75 times that of the melt. Large M_n show a suppression in permeability, consistent with Maxwell's reasoning that the silica cores become point defects that hinder molecular transport

when the polymer fraction becomes sufficiently large. Trends in relative ethyl acetate diffusion constant, while slightly less clear, follow a similar trend and clearly show that the permeability

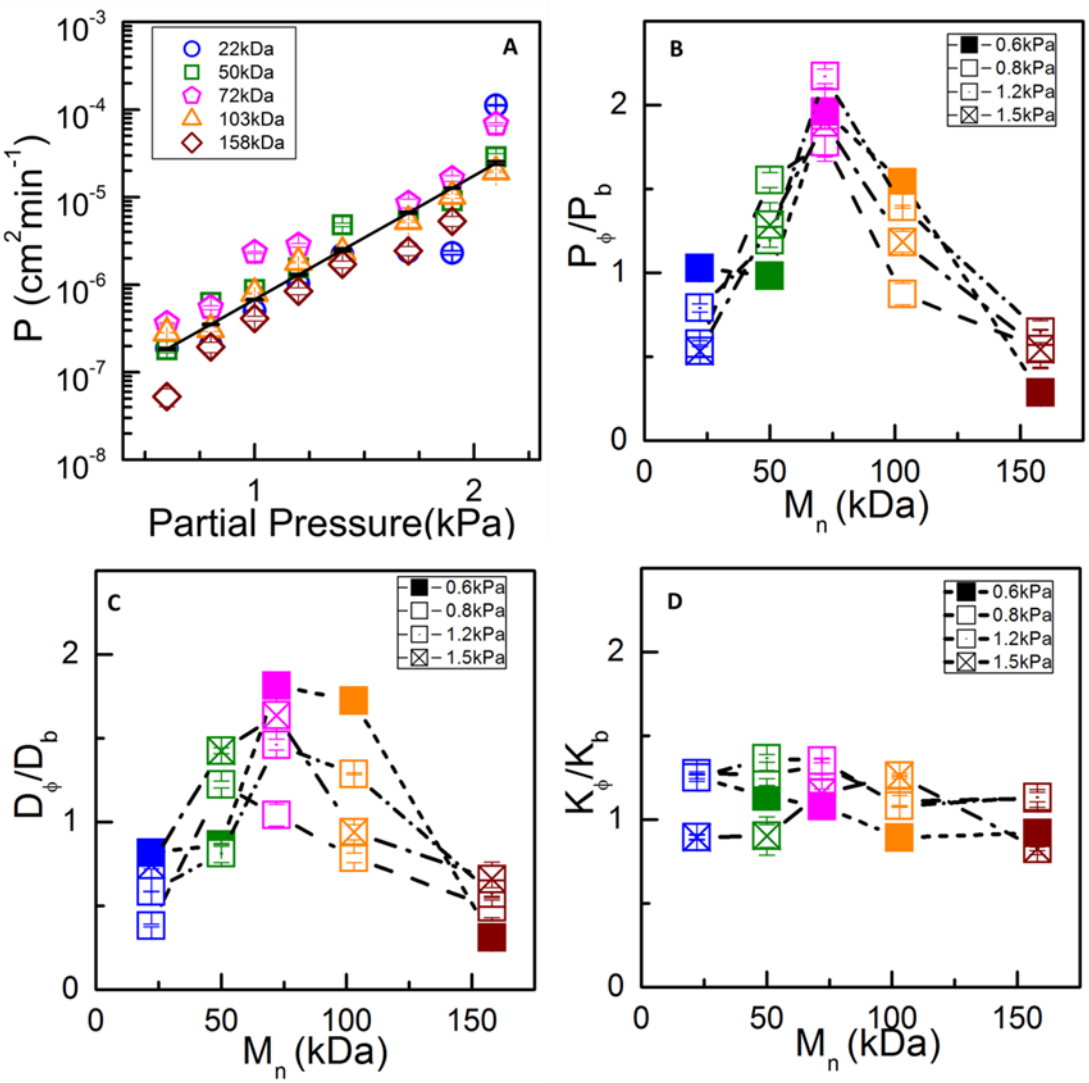

Figure B- 3: Ethyl acetate vapor diffusion in Σ=0.07chains/nm^2 graft density composites. (A) Extracted permeability data for a series of PMA composites with varied M_n with graft density; (B) relative permeability; (C) diffusion constant and (D) partition coefficient as a function of M_n

increase is predominantly a result of increased diffusion (Figure B- 3C). K_i varies slightly as well, but there is no observable trend with M_n and the increases are less than 30% than that of the neat polymer (Figure B- 3D).

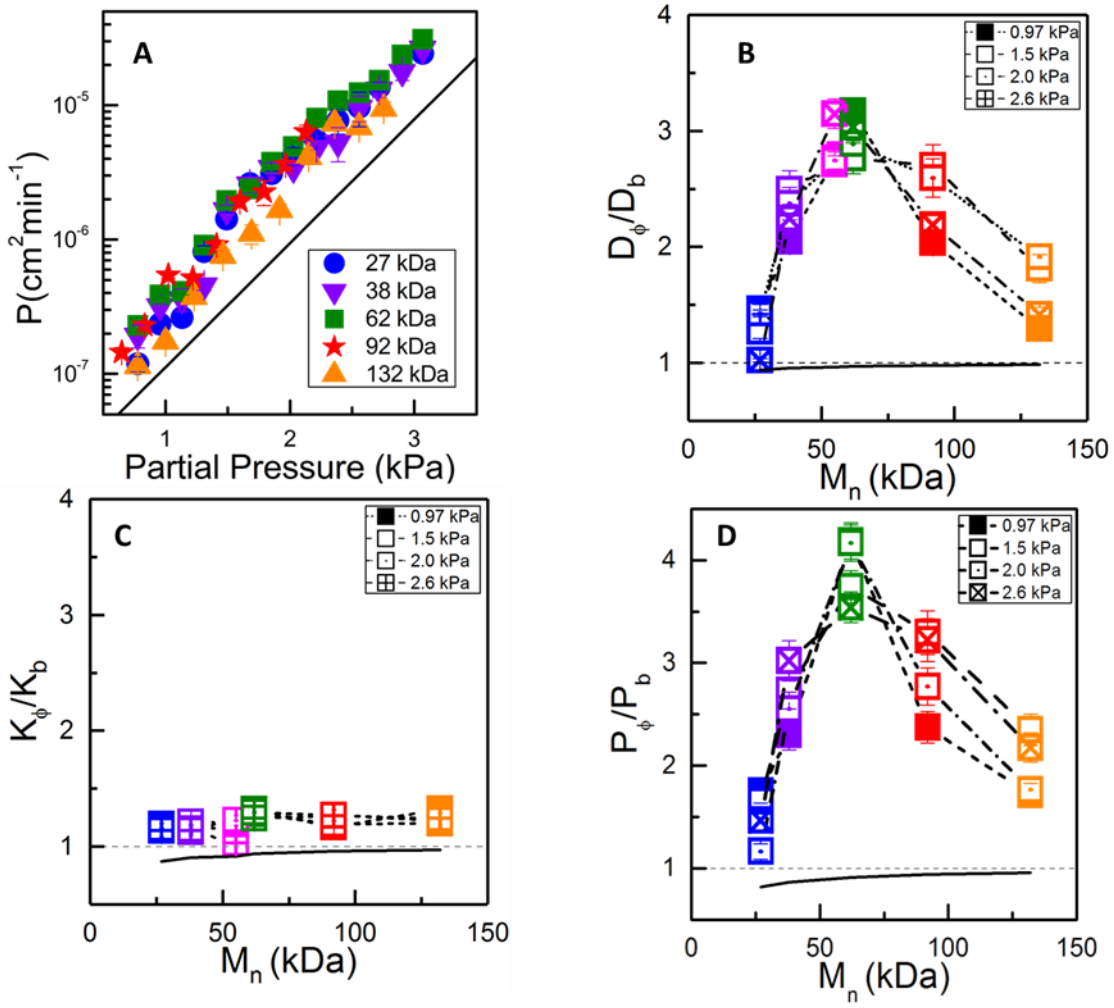

Figure B- 4: Ethyl acetate vapor diffusion in Σ=0.43chains/nm^2 graft density composites. (A) Extracted permeability data for a series of PMA composites with varied M_n with graft density Σ=0.07chains/nm^2; (B) relative permeability; (C) diffusion constant and (D) partition coefficient as a function of M_n

Additionally, raw relative diffusivities and partition coefficients for the σ=0.43chains/nm^2 PMA composites are compared to neat PMA melts as a function of M_n for multiple gas phase loadings in Figure B- 4B and Figure B- 4C (representative extracted data are shown in Figure B- 4A). At all experimental gas loadings, the permeability and the diffusivity show a non-monotonic increase as a function of the graft molecular weight, with a maximum permeability increase of

approximately 3.75 times that of neat PMA at moderate M_n (=62kDa).This relative increase is substantially higher than that observed for low graft density composites (see above). The partition coefficient is slightly increased in all molecular weights, but there is no discernable trend in the increase and the increase is generally within experimental error. The non-monotonic increases in permeability relative to the PMA melt are surprising as Maxwell's prediction would anticipate a suppression in relative permeability as the particle volume fraction ϕ is increased, i.e., the permeability should strictly decrease with decreasing polymer brush length.

Additionally, the effect of aging at low graft density is shown in Figure B- 5**.** No significant decrease in permeability due to aging was found after two years, suggesting that there has been no loss of material free volume with time as is typically observed in glassy polymers and polymer nanocomposites.

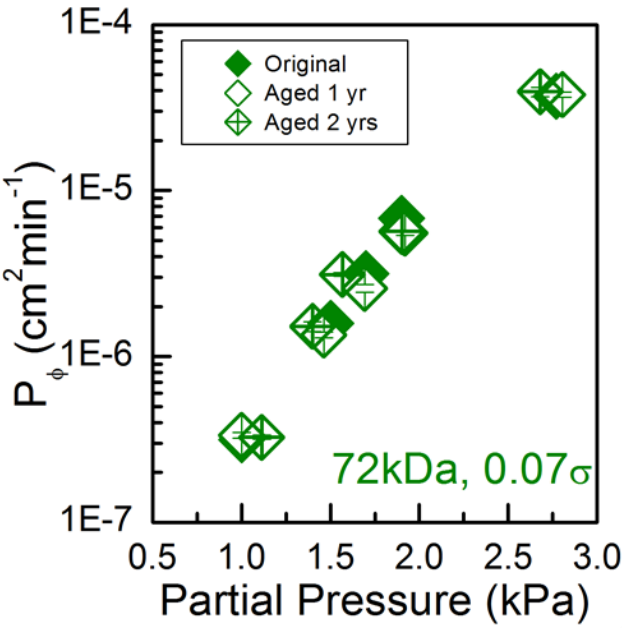

Figure B- 5: Effect of Aging on low graft density grafted particle membranes.

B.4 Permeance

We also report permeance data, calculated by dividing the measured permeability by the film thickness, in Figure B- 6. Figure B- 6A and Figure B- 6B refer to CO_2 permeance taken from conventional light gas permeation experiments, while Figure B- 6C and Figure B- 6D are from QCM experiments using ethyl acetate in a high σ PMA composite. While the permeance of these films are modest (Figure B- 6A), this is directly related to the thickness of the films tested. Given that the films are rubbery and that permeability is constant across a wide range of thicknesses, these materials can clearly allow for high permeance films. Figure B- 6B shows the CO_2 permeance of the PMA composite materials for film thicknesses of 500nm, which can be readily fabricated in the laboratory.

The ethyl acetate permeance data are shown in extracted and reduced form (Figure B- 6C and Figure B- 6D, respectively). In both cases we observe qualitatively similar trends. This is unsurprising as the measured film thicknesses of the composite films are all within the range of 560-595nm and therefore trends in permeance and permeability data are approximately equal. Figure B- 6E shows the relative permeance increase from light gas permeation experiments. For comparative purposes, the film thickness of all films is assumed to be 500nm and that the permeability of each material is identical to its 30-50μm counterpart. This is a very reasonable assumption given the excellent agreement between QCM experiments and conventional gas sorption experiments (see gas transport measurements in films with thickness <1μm via QCM, below). The qualitative shape in this plot is reminiscent of that seen in Figure 2.2B, indicating that both permeability and permeance are enhanced by nearly an order of magnitude in these composite materials.

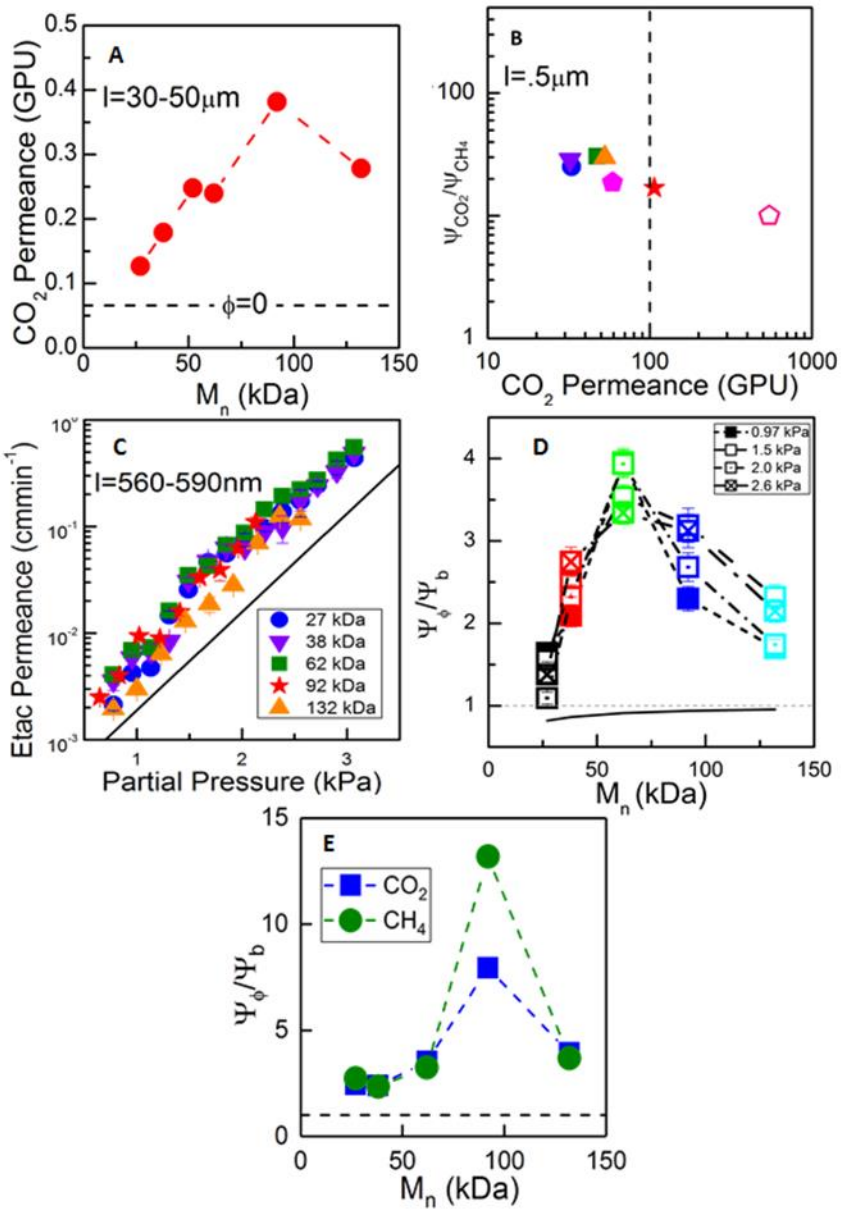

Figure B- 6: Permeance in Σ=0.43chains/nm^2 graft density composites. (A) Calculated permeance, Ψ, of PMA composites as a function of graft PMA molecular weight. Experimental film thicknesses are in the range of 30-50μm; (B) "Robeson" plot of CO_2/CH_4 selectivity against CO_2 permeance for film thicknesses of 500nm. The vertical line represents the permeance of cellulose acetate (100GPU), a common industrial membrane material; (C) Ethyl acetate permeance calculated from QCM; (D) Relative ethyl acetate permeance; (E) Relative permeance increase from light gas permeation experiments. For comparison, the CO_2 and CH_4 permeance in neat PMA are 13.44 and 0.48GPU, respectively.

B.5 Infinite Dilution Model

The permeability trend for each material sample can be fit to a simple exponential model of the form $P_\infty e^{\beta p}$, where p is the penetrant partial pressure and P_∞ and β are fitted parameters. For such a model, the coefficient β can be envisioned as a concentration dependent term, and P_∞ as a materials permeability at zero concentration (a so-called "infinite dilution" permeability). Relative values of β compared with β_{neat} for low and high σ composites are shown in Figure B-7A-B. For low σ composites, β/β_b=1 within experimental error. While there is a general increase in β for moderate molecular weight grafts at high σ, there is no discernable trend and the differences in this elevation again remain within measurement error. Conversely, Figure B- 7C shows that P_∞ exhibits non-monotonic behavior as a function of molecular weight for low σ materials. Consistent with the relative permeability curves in Figure B- 3B we observe that P_∞ suppressed at both low and high chain lengths, but has a strong local maximum at moderate chain lengths (i.e., M_n=72kDa). The same trend in P_∞ is qualitatively observed for high σ composites (Figure B- 7D) however in this case the relative ratio exceeds unity for all molecular weights. The local maximum also occurs at a moderate chain length of M_n=62kDa, consistent with low σ data.

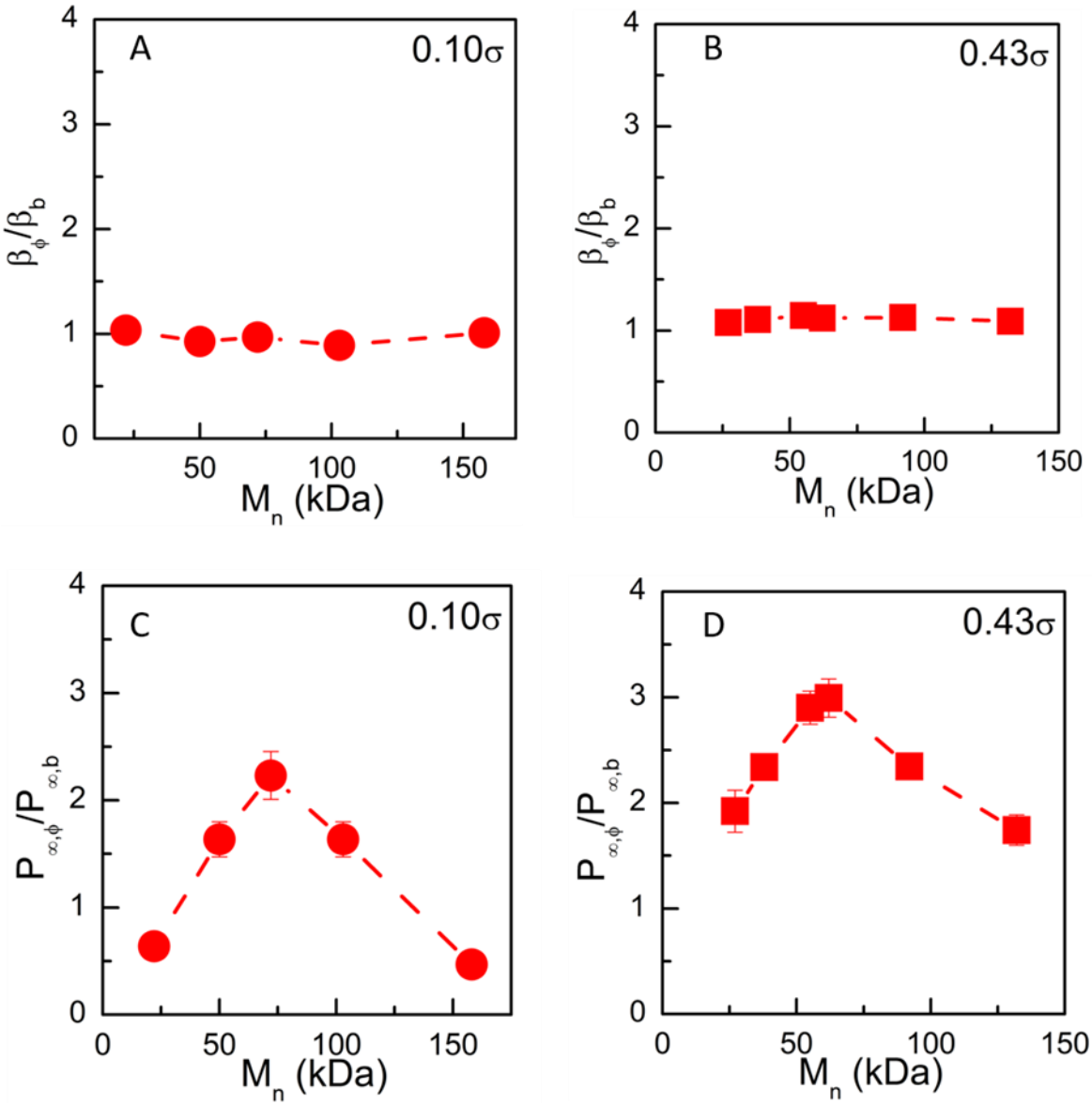

Figure B- 7: Exponential regression of permeability from QCM. Relative increase in (A) β for Σ=0.07chains/nm^2; (B) β for Σ=0.43chains/nm^2; (C) P_∞ for Σ=0.07chains/nm^2 composites; (D) P_∞ for Σ=0.43chains/nm^2 composites

B.6 QCM Measurements of Light Gases

The permeability of CO_2 in neat PMA (M_n=63kDa) measured QCM is 6.72 Barrer, which is in excellent agreement with the 6.67 Barrer measured using conventional permeation cells.[72] Diffusion constant and solubility values are also similar to values collected using conventional

techniques (see Figure B- 8A). Measurements of the CO_2 permeability in neat PMMA yield a value of 0.66 Barrer, also in good agreement with the literature value of 0.65 Barrer.[12] Additionally, we report the permeabilities and selectivities of various light gas pairs for PMA-based composites Figure B- 9.

A

	P_{CO_2} (Barrer)	S_{CO_2} ($^{cc}/_{cc\ atm}$)	D_{CO_2} ($\times 10^8\ ^{cm^2}/_{s}$)
Paul, 1985	6.67	1.981	2.56
QCM-D	6.72±.12	1.980±.006	2.58±.04

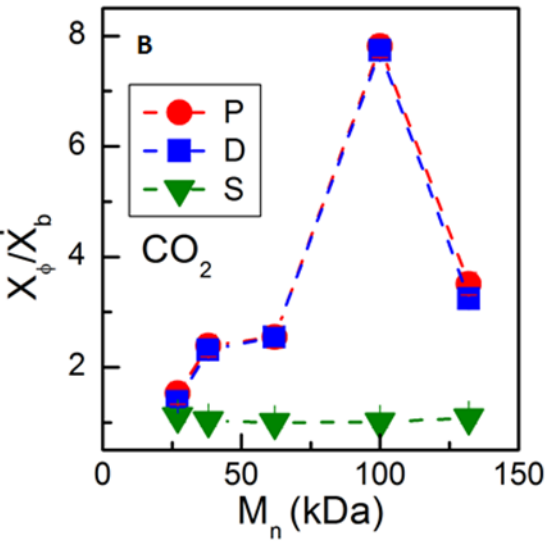

C

Graft M_n (kDa)	P_{CO_2} (Barrer)
27.0	10.05
38.1	15.71
62.1	16.77
100.9	51.40
132.1	23.11

Figure B- 8: Verification of QCM as a method for measuring light gas diffusion. (A) Comparison of P, D, and S of CO_2 in neat PMA (M_n =135kDa) measured with QCM compared to measurements from conventional permeation experiments. Literature values are taken from reference [72]; (B) relative increase of P, D, and S of CO_2 in grafted PMA composite materials. The relative increase in P from these experiments is similar to that found via permeation experiments; (C) Absolute CO_2 permeabilities of PMA composites.

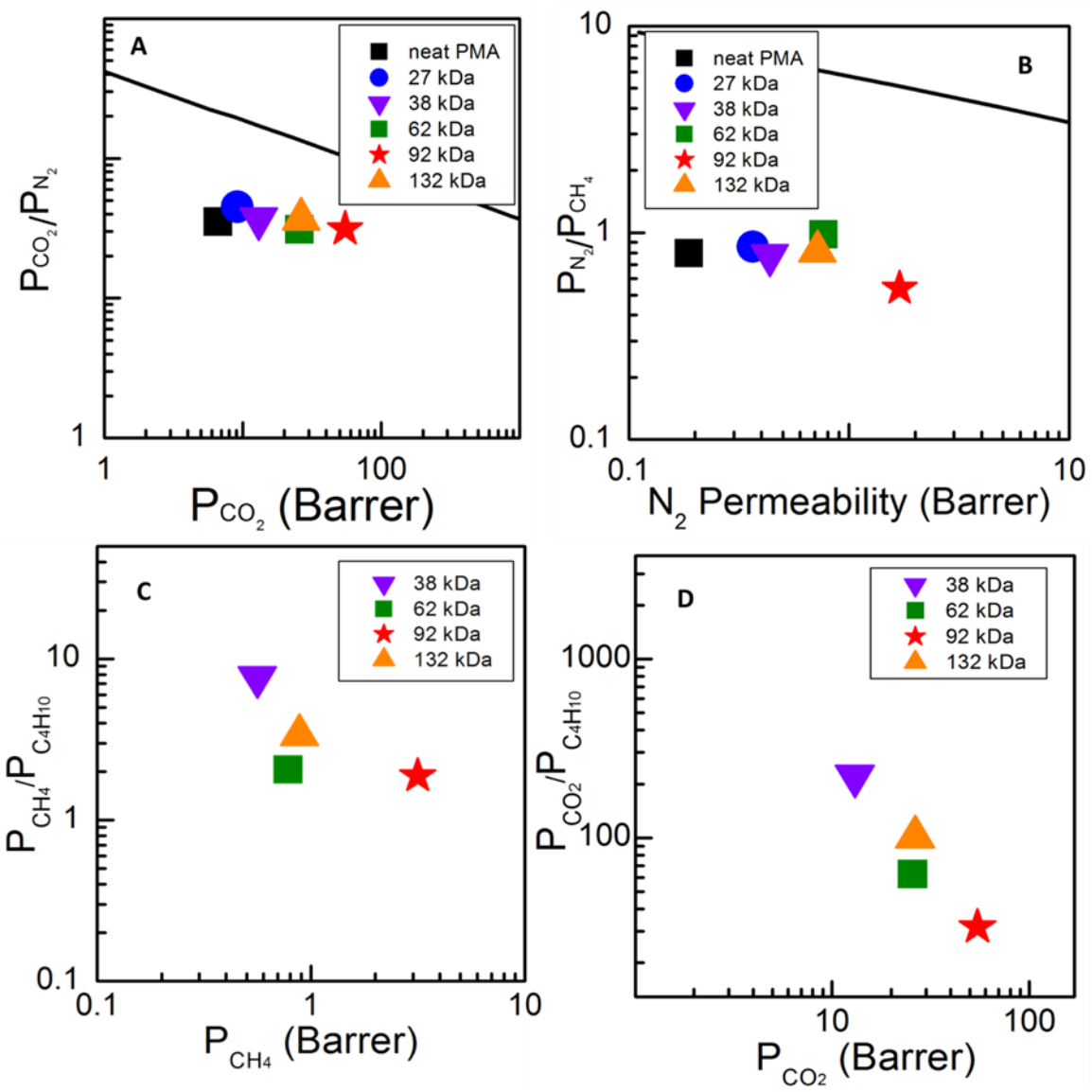

Figure B- 9: Additional light gas permeation for PMA grafted nanoparticle films. Robeson plots of (A) CO_2/N_2; (B) N_2/CH_4; (C) CH_4/C_4H10; (D) CO_2/C_4H_{10} for PMA composites with Σ=0.43chains/nm^2

CO_2 solubility in the composite films is shown in Figure B- 8B. It is evident that there is increased gas sorption in the composite materials relative to the neat PMA, which is further corroborated by measurements of N_2 solubility using the BET method. While the relative solubility of CO_2 is increased in the composite materials, no discernable trend can be seen and most composite solubilities are within 20% that of neat PMA. Conversely, *D* is strongly elevated in the composite materials by up to eight times that of neat PMA, consistent with QCM data on

light gas permeation experiments. The absolute CO_2 permeability values calculated using this technique are shown in Figure B- 8C so they may be directly compared with that of neat PMA.

The CO_2 and CH_4 permeabilities in PMMA-grafted nanoparticle materials were also tested. CO_2 permeability shows no M_n dependence for the PMMA materials tested. The relative permeability increases in a series of PMMA composites are shown in Figure B- 10A. Trends qualitatively similar to those observed for PMA composites are also seen here; that is, permeability is enhanced in all composites, and the degree of increase in permeability is non-monotonically dependent on the graft M_n. The infinite dilution values of P_{CO_2} and D_{CO_2} also show similar enhancements (Figure B- 10B). This indicates that the permeability enhancements are not limited to rubbery polymers, and this grafting procedure can therefore be extended to polymer glasses as well.

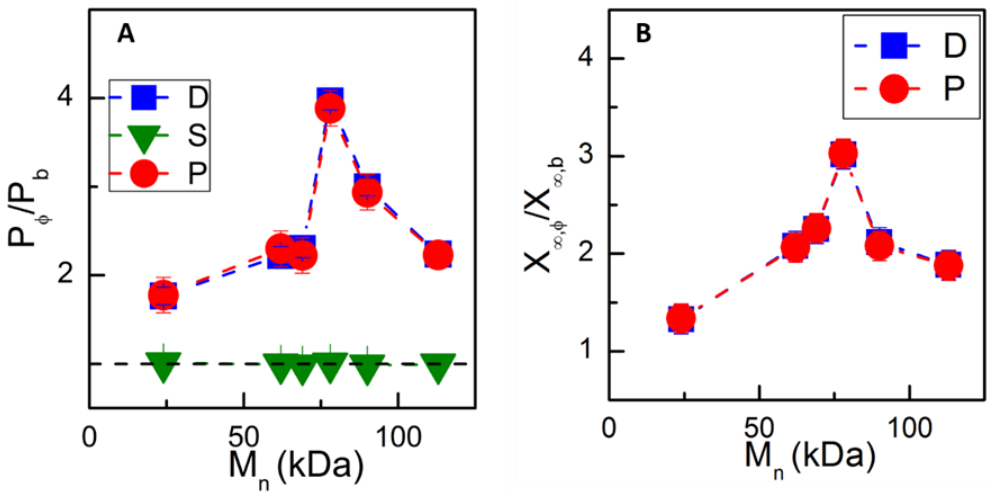

Figure B- 10: Gas transport in PMMA grafted composites via QCM. (A) Comparison of relative P, D, and S of CO_2 in PMMA composites measured using QCM. (B) Infinite dilution properties of P, and D in these materials